

Supplementary Information for:

**Topologies of synthetic gene circuit for optimal fold change activation**

**List of Contents**

1.	Simplified models with linear operations.....	2
2.	Models and simulations.....	5
2.1	Biological models for transcriptional interference and antisense transcription.....	5
2.2	Models for ICF design.....	12
2.2.1	Molecular ICF three-nodes model.....	12
2.2.2	Genetic ICF four-nodes model.....	14
2.3	Models for DNF design.....	16
2.3.1	Molecular DNF three-nodes model.....	16
2.3.2	Genetic DNF four-nodes model.....	18
3.	Experimental results for the 6 promoters.....	20
3.1	The synthetic promoter $P_{BADsyn}$ .....	20
3.2	The synthetic promoter $P_{lacO}$ .....	23
3.3	The native specific promoter $P_{LhrtO}$ .....	25
3.4	The native specific promoter $P_{arsR}$ .....	28
3.5	The native stress promoter $P_{katG}$ .....	30
3.6	The native stress promoter $P_{recA}$ .....	33
4.	Experimental data from Flow cytometry.....	35
5	Plasmid maps used for this work (Table S1).....	81
6	Synthetic parts used for this work (Tables S2, S3 and S4).....	88
	References.....	94

## 1. Simplified models with linear operations:

In this section, we build linear models of three circuit topologies that can control their fold change:

- (1) Open loop (OL) circuit
- (2) Indirect Coherent feedforward (ICF) circuit.
- (3) Mutual inhibition by double negative feedback (DNF) circuit

First, we describe the part under test (PUT) in its prototype topology, as shown in Fig. S1. The circuit performs a non-linear monotonic function with two distinct levels: (1) a minimum normalized level “ $\beta$ ” (e.g., basal level of promoter) and (2) a maximum normalized level “1”. Such a function can be described by:

$$Out = (1 - \beta) \cdot f(In) + \beta \quad (\text{S1.1})$$

And the fold change detection FCA level is given by:

$$FCA = 1 - \beta \quad (\text{S1.2})$$

Where  $f(0)$  is also non-linearly monotonic with a basal level equal to zero, and a maximum level equal to one. The  $f(0)$  satisfies:

$$f_{min}(In = 0) = 0 \quad (\text{S2.1})$$

$$f_{max}(In = In_{max}) = 1 \quad (\text{S2.2})$$

$$FCA = 1 \quad (\text{S2.3})$$

Sensitivity measures the fold change in the output regarding the fold change in the input, and is given by:

$$S = \frac{\Delta Out / Out}{\Delta In / In} \quad (\text{S3})$$

By substituting Eq. S1.1 into Eq. S3, we get the sensitivity of part under test as:

$$\frac{\Delta Out}{Out} = \frac{(1-\beta) \cdot df(0)}{(1-\beta) \cdot f(0) + \beta} \quad (\text{S4.1})$$

$$S = \frac{S_f}{1 + \frac{\beta}{(1-\beta) \cdot f(0)}} \quad (\text{S4.2})$$

Where  $S_f = \frac{df(0)/f(0)}{\Delta In / In}$  is the sensitivity of the function  $f(0)$ . For the open loop circuit (Fig. S1B), the output is reduced by a constitutive value ( $F_S$ ), and is given by:

$$Out = (1 - \beta) \cdot f(0) + \beta - F_S \quad (\text{S5.1})$$

Since the basal and maximum levels are reduced by the same amount, we do not expect for an improvement in the FCA level:

$$Out_{max} = 1 - F_S \quad (\text{S5.2})$$

$$Out_{min} = \beta - F_S \quad (\text{S5.3})$$

$$FCA_f = 1 - \beta \quad (\text{S5.4})$$

$$S = \frac{S_f}{1 + \frac{\beta - F_S}{(1-\beta) \cdot f(In)}} \quad (\text{S5.5})$$

Our analysis over the three circuits is presented with normalizations, with  $0 < \beta < 1$ ,  $0 < F_S < 1$ .

The indirect coherent feedforward (ICF) circuit is shown in Fig. S1C. The signal of the part under test splits to two branches, the sum of which positively regulate the final output. While in the first branch the signal directly controls the final output, the second branch involves two inhibition nodes to regulate the final output. The ICF circuit output is given by:

$$Out = (1 - \beta) \cdot f(In) + \beta - F_S \cdot [1 - (1 - \beta) \cdot f(In) - \beta] \quad (\text{S6.1})$$

$$Out_{max} = 1 \quad (\text{S6.2})$$

$$Out_{min} = \beta - F_S \cdot (1 - \beta) \quad (\text{S6.3})$$

$$FCA = 1 - \beta + F_S \cdot (1 - \beta) \quad (\text{S6.4})$$

$$S = \frac{S_f}{1 + \frac{\beta - F_S + F_S \cdot \beta}{(1-\beta) \cdot (1+F_S) \cdot f(In)}} \quad (\text{S6.5})$$

From Eq. S6.4 and Eq. S6.5, we obtain the maximum value of *FCA* and maximum value of sensitivity when:

$$F_S = \frac{\beta}{1-\beta} \quad \rightarrow \quad FCA_{max} = 1, \quad S = S_f \quad (\text{S7})$$

By selecting a specific level of  $F_S$  (Eq. S7), we can enhance the FCA level using the ICF design.

The double negative feedback loop (DNF) circuit is shown in Fig. S1D. The signal of the part under test is regulated by a cascade of an indirect positive feedback and an inhibition with a negative signal. The circuit output is given:

$$Out = (1 - \beta) \cdot f(In) + \beta - F_S \cdot (1 - out) \quad (\text{S8.1})$$

$$\Rightarrow Out = \frac{(1-\beta) \cdot f(In) + \beta - F_S}{1 - F_S}$$

$$Out_{max} = 1 \quad (\text{S8.2})$$

$$Out_{min} = \frac{\beta - F_S}{1 - F_S} \quad (\text{S8.3})$$

$$FCA = \frac{1 - \beta}{1 - F_S} \quad (\text{S8.4})$$

$$S = \frac{S_f}{1 + \frac{\beta - F_S}{(1-\beta) \cdot f(In)}} \quad (\text{S8.5})$$

From Eq. S8.3 and Eq. S8.5, we obtain maximum value of *FCA* and maximum value of sensitivity when:

$$F_S = \beta \quad \rightarrow \quad FCA_{max} = 1, \quad S = S_f \quad (\text{S9})$$

By selecting a specific level of  $F_S$  (Eq. S9), we can enhance the FCA level using the DNF design.

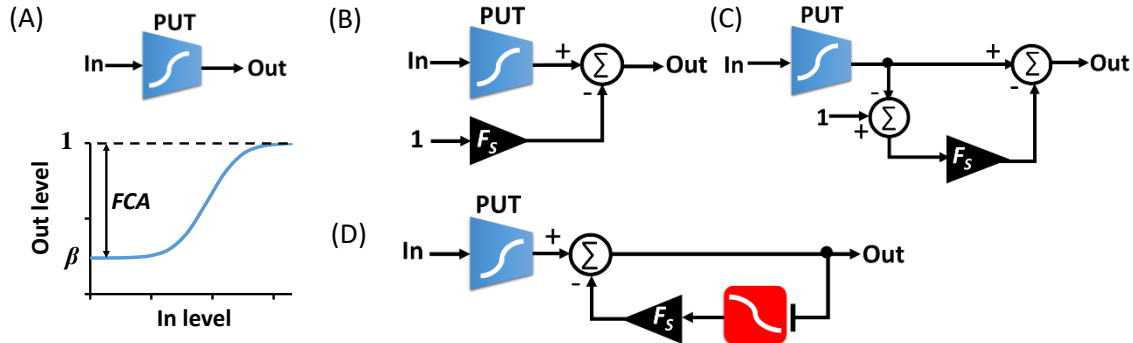


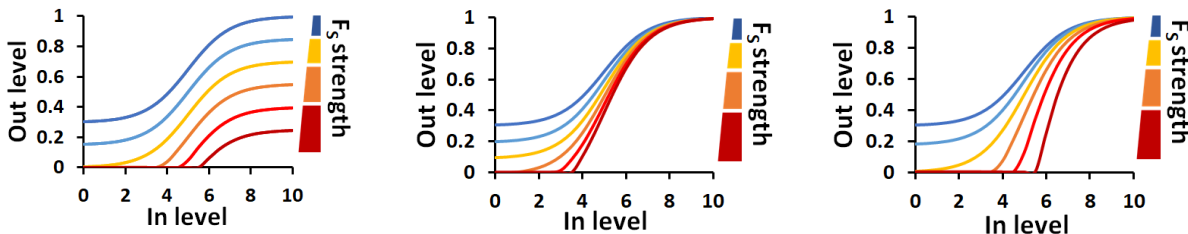
Fig. S1. (A) Transfer function of part under test (PUT) in its prototype design. (B) Open loop (OL) design for basal level reduction. (C) Indirect coherent feedforward (ICF) design for basal level reduction. (D) Double negative feedback (DNF) design for basal level reduction

Our simulation results including the input-output transfer function and sensitivity for the three circuits are shown in Fig. S2. In these simulations, we assumed that  $f(I_n)$  is a sigmoid function that is shifted in  $x$ -axis:

$$f(I_n) = \frac{e^{(x-x_0)}}{1+e^{(x-x_0)}} \quad (\text{S10})$$

Since biological signals cannot be negative, only non-negative outputs are allowed for the three designs. All the negative values were set to zero. The sensitivity was calculated using Eq. S3. As shown in our simulation results (Fig. S3A), the open loop design cannot increase the FCA, while the DNF loop can reach maximum of FCA=1 and reduce the basal level to zero when  $F_S=\beta$ . Similar behavior can be obtained for the ICF design, when  $F_s=\beta/(1-\beta)$ . We define minimum detection level (MDL) as the input value when the sensitivity is maximum (Fig. S3C). Interestingly, the three circuits show the same characteristics of minimum detection level (MDL) as a function of  $F_S$  (Fig. S3B). Our result show that MDL has optimum at different  $F_S$  value for each circuit. For ICF circuit, minimal MDL is obtained at  $F_S=\beta/(1-\beta)$ . For DNF circuit, minimal MDL is at  $F_S=\beta$ . In both cases, the minimum MDL values are the same. The MDL is proportional to the limit of detection corresponding to the lowest concentration of a target input that is detectable.

As shown in simulation results, there is a strong dependency between the basal level and the  $F_S$  strength. This dependency can guide us to search for the  $\beta$  and  $F_S$  values to reach an optimal performance (Maximum FCA and Minimum MDL). Therefore, we graphed  $\beta$ - $F_S$  diagrams to show qualitatively how relations between  $\beta$  and  $F_S$  affect FCA and MDL in ICF and DNF circuits (Fig. S4A-4B). For comparison, we also combined the graphs for both circuits (Fig. S4C).



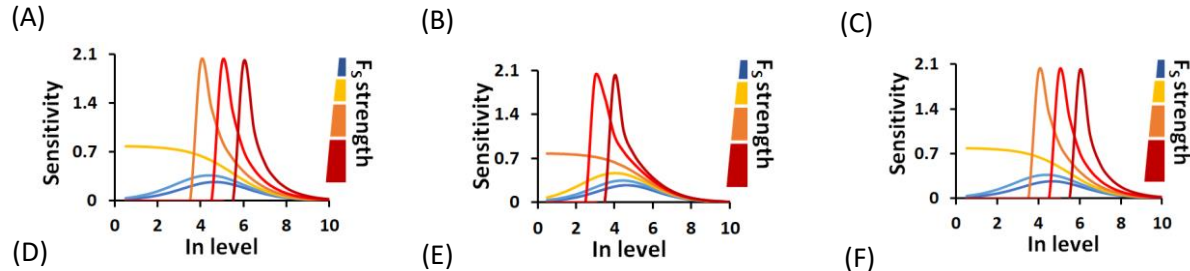


Fig. S2. (A)-(C) simulation results for input-output transfer functions for the open loop (OL), indirect coherent feedforward (ICF) and double negative feedback (DNF) designs. (D)-(F) Sensitivity results for OL, ICF and DNF models based on Eq. S3.

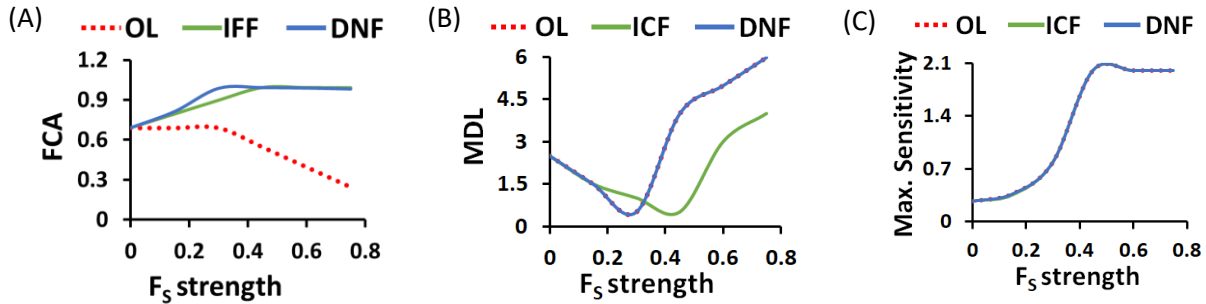


Fig. S3. Simulation results of (A) Fold change activation (FCA) versus F<sub>s</sub> strength, (B) Minimum detection level versus F<sub>s</sub> strength. Minimum detection level or MDL is defined as the input value when the sensitivity is maximum, and (C) Maximum sensitivity versus F<sub>s</sub> strength. These results were estimated based on the simulation results of Fig. S2.

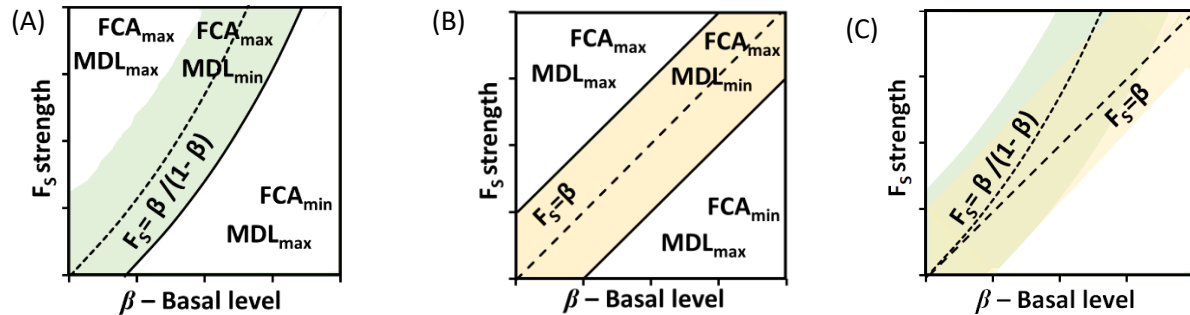


Fig. S4. Qualitative  $\beta$ -F<sub>s</sub> diagrams for (A) indirect coherent feedforward circuit (ICF), (B) double negative feedback loop (DNF) and (C) Both circuits.

## 2. Models and simulations

### 2.1. Biological models for transcriptional interference and antisense transcription:

Here, we implement the subtraction operation in Fig. S5 using two biological models:

- (1) Transcriptional interference (Fig. S5A). We utilize two competitive promoters ( $P_{Forw}$  vs  $P_{Rev}$ ) that located in opposite orientation to each other, where  $P_{Rev}$  impede the transcriptional activity of  $P_{Forw}$ . The  $P_{Rev}$  promoter is located upstream to the target gene. This special organization allows interference between the forward and reverse promoters to arise due to RNA polymerase (RNAP) collisions. The promoter under test (PUT) is used as  $P_{Forw}$ .

(2) Antisense transcription (Fig. S5B). We utilize two competitive promoters ( $P_{Forw}$  vs  $P_{Rev}$ ) that located in opposite orientation to each other, where  $P_{Rev}$  produces antisense mRNAs to block the translation of mRNA transcribed from  $P_{Forw}$ . The  $P_{Rev}$  promoter is located downstream to the target gene. This special organization allows hybridization of complementary mRNAs from the forward and reverse promoters and thus down-regulation of promoter translational activities. The promoter under test (PUT) is used as  $P_{Forw}$ .

Although a detailed biophysical model was developed (Brophy & Voigt, 2016) for modeling such complex structure of promoters, here we took a simpler approach. The purpose of our models is to capture the general behavior of systems and examine how they can be incorporated into the ICF and DNF circuits. Regarding the transcriptional interference in Fig. 5SA, because the two opposite promoters are located close to each other, we treat them as one system modeled using statistical thermodynamics (Fig. S6). The binding of RNA polymerases recruited by TFs to promoters is modeled according to the Shea-Ackers formalism (Ackers et al., 1982; Bintu et al., 2005). The model describes five different states: (1) Both promoters are unbound; (2) RNA polymerases (RNAP) without transcription factors are bound on both promoters and cause a basal level activity. (3) The complex activator (X)-RNAP is bound to the forward promoter, activating the output signal. (4) The complex activator (Y)-RNAP is bound to the reverse promoter, repressing the output signal. (5) The complex activator (X)-RNAP is bound to the forward promoter, and the complex activator (Y)-RNAP is bound to the reverse promoter. In our model we also assume that the collision interference is large and thus the probability that the forward and the reverse RNA polymerases can simultaneously bind to the DNA is very low ( $\theta \ll 1$ ). The level of gene expression is proportional to the probability ( $P$ ) that RNA polymerase is bound to the forward promoter at the equilibrium, and is given by:

$$P = \frac{\left(\frac{X}{K_{df}}\right)^{n_f} + \beta}{1 + \left(\frac{X}{K_{df}}\right)^{n_f} + \left(\frac{Y}{K_{dr}}\right)^{n_r} + \beta} \quad (S11)$$

Where  $X$  and  $Y$  are the concentrations of transcription factors which bind to forward and reverse promoters, respectively.  $n_f$  and  $n_r$  are Hill-coefficients,  $K_{df}$  and  $K_{dr}$  are dissociation constants of transcription factors binding to forward and reverse promoters, respectively. Based on Eq. S11, the maximum activity of promoter is 1, however, the collision interference can also reduce the maximum expression level, and as a result, we can modify Eq. S11:

$$P = \frac{\left(\frac{X}{K_{df}}\right)^{n_f} + \beta}{1 + \left(\frac{X}{K_{df}}\right)^{n_f} + \rho_1 \cdot \left(\frac{Y}{K_{dr}}\right)^{n_r} + \beta} \cdot \left( \frac{1}{1 + \rho_2 \cdot \left(\frac{Y}{K_{dr}}\right)^{n_r}} \right) \quad (S12)$$

where  $\rho_1$  and  $\rho_2$  are parameters representing the strength of two processes as Y level increases: (1) shift of switching threshold with coefficient  $\rho_1$  and (2) repression in the expression level with coefficient  $\rho_2$ . The kinetics of gene expression based on the promoter activity in Eq. S12 is:

$$\frac{dz}{zt} = \alpha \cdot \frac{\left(\frac{X}{K_{df}}\right)^{n_f} + \beta}{1 + \left(\frac{X}{K_{df}}\right)^{n_f} + \rho_1 \cdot \left(\frac{Y}{K_{dr}}\right)^{n_r} + \beta} \cdot \left( \frac{1}{1 + \rho_2 \cdot \left(\frac{Y}{K_{dr}}\right)^{n_r}} \right) - \frac{z}{\tau_z} + P_{min} \quad (S13)$$

At the steady state we get:

$$Z = Z_{max} \cdot \frac{\left(\frac{X}{K_{df}}\right)^{n_f} + \beta}{1 + \left(\frac{X}{K_{df}}\right)^{n_f} + \rho_1 \left(\frac{Y}{K_{dr}}\right)^{n_r} + \beta} \cdot \left( \frac{1}{1 + \rho_2 \cdot \left(\frac{Y}{K_{dr}}\right)^{n_r}} \right) + Z_{min} \quad (S14)$$

where  $Z_{max}$  is the maximum protein level, and  $Z_{min}$  is the minimum protein level. The  $Z_{min}$  level is different than the basal level. From Eq. S14, we can see that the basal level of the forward promoter is achieved when  $X=0$  and is equal to  $\frac{\beta}{1+\rho_1 \cdot \left(\frac{Y}{K_{dr}}\right)^{n_r}}$  which is affected by  $\beta$  and  $Y$ , while the  $Z_{min}$  is not regulated. For example,  $Z_{min}$  can be a result of autofluorescence.

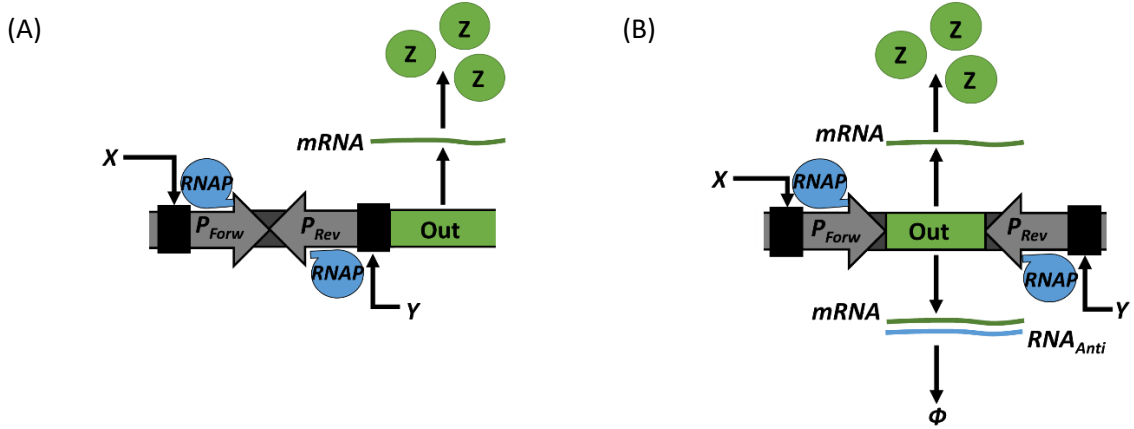


Fig. S5. Implementation of subtraction: (A) A schematic of a genetic circuit based on transcriptional interference. (B) A schematic of a genetic circuit based on antisense transcription.

Simulation results of the transcriptional interference model in Eq. S14 are shown in Fig. S7. The  $\rho_1$  and  $\rho_2$  parameters have a significant impact on the results. As explained previously,  $\rho_1$  shifts the transfer function of  $Z$  relative to  $X$  rightward, increasing the effective dissociation constant ( $K_{df}$  is equal to the effective dissociation constant when  $Y/K_{dr} \ll 1$ ).  $\rho_2$  decreases the effective maximum  $Z$  level through the coefficient  $\left(\frac{1}{1+\rho_2 \cdot \left(\frac{Y}{K_{dr}}\right)^{n_r}}\right)$ . Interestingly, our simulation results show that when  $\rho_1=0$ ,  $\rho_2=1$ , the transcriptional interference behaves as a pure subtraction with respect to  $Y$  level (Fig. S7A and Fig. S7E have similar behaviors as in Fig. S2A). In this case, the FCA is either a constant without dependency on  $Y$  level for  $Z_{min}=0$  (Fig. S8A) or decreases as  $Y$  increases for  $Z_{min}=20$  (Fig. S8B). Here  $Z_{min}$  affects the FCA in the same way as in the linear model where all the negative values were set to zero, because biological signal cannot be negative. Another interesting case is when  $\rho_1=1$ ,  $\rho_2=0$  (Fig. S7F), specifically, FCA level increases even when the  $Z_{min}$  is high (Fig. S8B). This is because when  $\rho_2=0$ , there is no reduction to  $Z$  expression level even when the input is very high. An increase in  $Y$  can result in threshold shift and thereby enhance circuit FCA, but when it represses the gene expression level, a reduction of FCA can be observed. Consequently, an optimal level of FCA can be obtained at specific  $Y$  level (Fig. S8B). The main conclusions from our simulation results are as follows:

1. Transcriptional interference model can behave as a pure subtraction when there is only a repression component due to the enhanced activity of the reverse promoter ( $Y$  level), without any effect on the threshold of the complex promoter, that is,  $\rho_1=0$ ,  $\rho_2=1$  (Top curves in Fig. S8A and S8B).

2. The FCA of promoters based on transcriptional interference can be improved by enhancing the activity of reverse promoter ( $Y$  level), when the reverse promoter affects the threshold of the complex promoter, that is,  $\rho_1 \neq 0$ ,  $\rho_2 = 1$ .

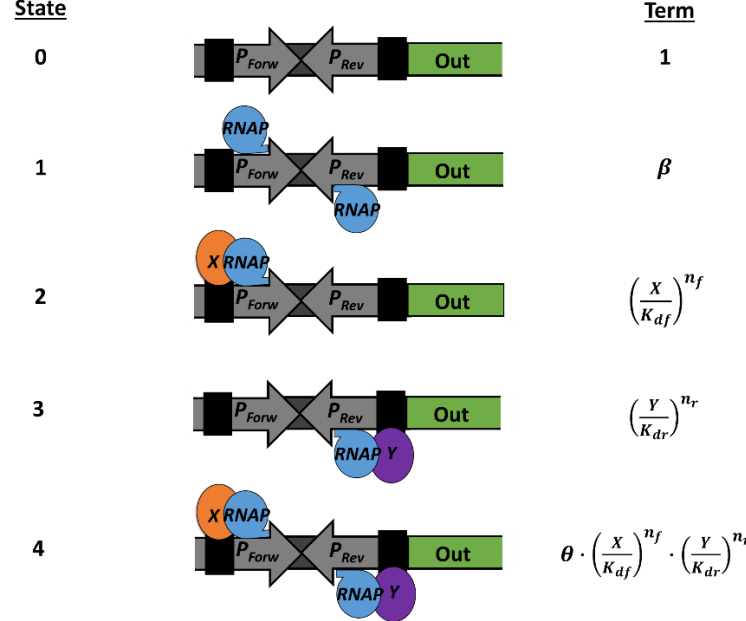


Fig. S6. The binding states of the forward promoter and the transcriptional interference by the reverse promoter.

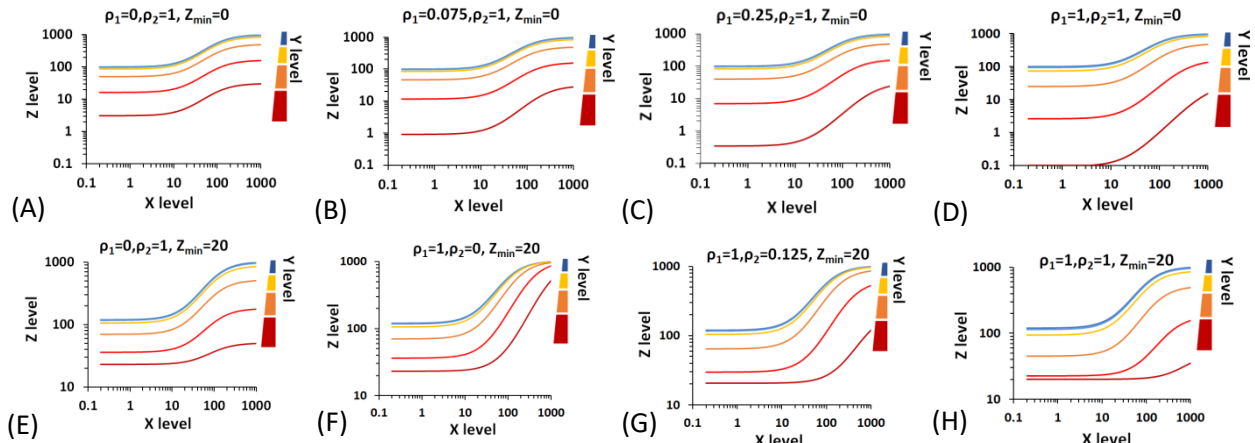


Fig. S7. Simulation results of transcriptional interference model (Eq. S14) as function of  $X$  levels (activity of forward promoter) and  $Y$  levels (activity of reverse promoter). Simulation parameters:  $n_f=1.5$ ,  $n_r=1.5$ ,  $K_{df}=100$ ,  $K_{dr}=100$ ,  $\beta=0.1$ ,  $Z_{max}=1000$ .

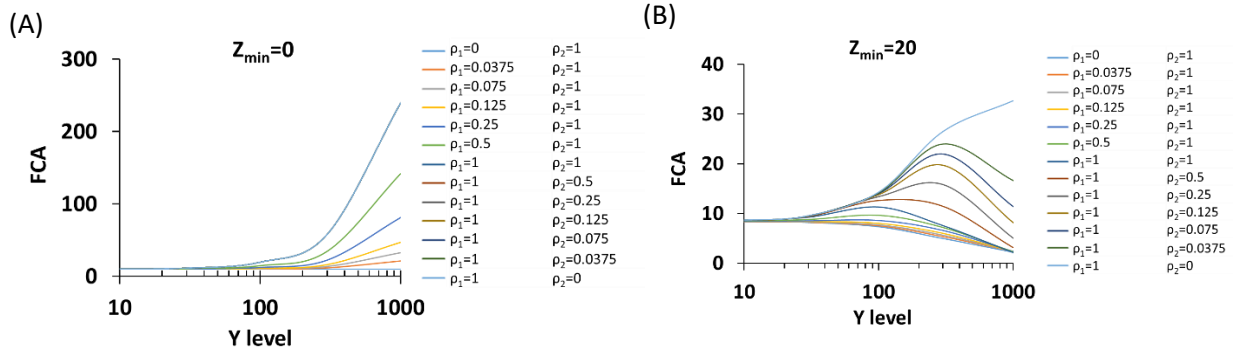


Fig. S8. Fold change activation (FCA) level of transcriptional interference model versus the activity of reverse promoter (Y level), based on results Fig. S7, (A) when  $Z_{min}=0$ , (B) when  $Z_{min}=20$ .

In this work, the biophysical model of antisense transcription is based on the biochemical binding reaction occurring between mRNA and antisense RNA (Fig. S5B), without considering the RNA polymerase (RNAP) collisions:



where mRNA is the level of mRNA produced from the forward promoter, and  $RNA_{Anti}$  is the level of antisense RNA produced from the reverse promoter, and  $K_m$  is the dissociation constant of the reaction. At steady state, we obtain:

$$Complex = \frac{mRNA \cdot RNA_{Anti}}{K_m} \quad (S16.1)$$

$$\frac{dmRNA}{dt} = -\frac{dComplex}{dt} \rightarrow mRNA = mRNA_T - Complex \quad (S16.2)$$

$$\frac{dRNA_{Anti}}{dt} = -\frac{dComplex}{dt} \rightarrow RNA_{Anti} = RNA_{Anti\_T} - Complex \quad (S16.3)$$

Where  $mRNA_T$  and  $RNA_{Anti\_T}$  are the total level of mRNA and antisense RNA. Substituting Eq. S16.2, Eq. S16.3 into Eq. S16.1:

$$Complex = \frac{(mRNA_T - Complex) \cdot (RNA_{Anti\_T} - Complex)}{K_m} \quad (S17)$$

With the solution of:

$$Complex = \frac{(mRNA_T + RNA_{Anti\_T} + K_m) - \sqrt{(mRNA_T + RNA_{Anti\_T} + K_m)^2 - 4 \cdot mRNA_T \cdot RNA_{Anti\_T}}}{2} \quad (S18)$$

The expression level of the output  $Z$  is proportional to the free mRNA:

$$Z = \alpha_Z \cdot \tau_Z \cdot (mRNA_T - Complex) + Z_{min} \quad (S19)$$

$\alpha_Z$  is the translation rate and  $\tau_Z$  is the protein half-life.  $Z_{min}$  is a minimum protein level, analogous to  $Z_{min}$  in Eq. S14. The concentrations of  $mRNA_T$  and  $RNA_{Anti\_T}$  are

$$mRNA_T = M_f \frac{\left(\frac{x}{K_{df}}\right)^{n_f} + \beta_f}{1 + \left(\frac{x}{K_{df}}\right)^{n_f}} \quad (S20.1)$$

$$RNA_{Anti\_T} = M_r \frac{\left(\frac{Y}{K_{dr}}\right)^{n_r} + \beta_r}{1 + \left(\frac{Y}{K_{dr}}\right)^{n_r}} \quad (S20.2)$$

Where  $M_f$  and  $M_r$  are the maximum mRNA and RNA<sub>Anti</sub> levels and are produced by the forward and reverse promoters, respectively. Simulation results of the antisense transcription model based on Eqs. S18 to S20.2 are shown in Fig. S9. Interestingly, the results show that when  $K_m$  is slightly equal to  $M_r$ , the antisense transcription model behaves as a pure subtraction with respect to  $Y$  level (Fig. S9A has a similar behavior to Fig. S2A). In this case, the FCA based on mRNA level is constant without dependency on  $Y$  levels (Fig. S10A), and FCA based on protein levels decreases when  $Y$  is increased (Fig. S10B,  $Z_{min}>0$ ). In case that the affinity of the binding reaction between mRNA and antisense RNA is strong, i.e.,  $K_m$  is small, increasing the  $Y$  level can improve the FCA (Figs. S9B, S9C, S10A, 10B). This interesting dependency on  $K_m$  can be explained by Eq. S17, when mRNA- RNA<sub>Anti</sub> complex level is small:

$$Complex \ll mRNA_T + RNA_{Anti\_T} + K_m$$

$$\Rightarrow Complex = mRNA_T \cdot \frac{RNA_{Anti\_T}}{K_m + RNA_{Anti\_T} + mRNA_T} \quad (S21)$$

Case 1:  $K_m \gg mRNA_T + RNA_{Anti\_T}$ , when  $K_m$  is larger than  $M_f$  and  $M_r$ : We can assume that the concentration of the complex is smaller than the concentrations of  $mRNA_T$  and  $RNA_{Anti\_T}$  and therefore, the complex concentration can be written as:

$$Complex = \frac{mRNA_T \cdot RNA_{Anti\_T}}{K_m} \quad (S22.1)$$

$$mRNA = \frac{mRNA_T}{K_m} \cdot (K_m - RNA_{Anti\_T}) \quad (S22.2)$$

$$mRNA = \frac{M_f}{K_m} \cdot \frac{\left(\frac{X}{K_{df}}\right)^{n_f} + \beta_f}{1 + \left(\frac{X}{K_{df}}\right)^{n_f}} \cdot \left( K_m - M_r \cdot \frac{\left(\frac{Y}{K_{dr}}\right)^{n_r} + \beta_r}{1 + \left(\frac{Y}{K_{dr}}\right)^{n_r}} \right) \quad (S22.3)$$

$$mRNA = \frac{M_f}{K_m} \cdot \frac{\left(\frac{X}{K_{df}}\right)^{n_f} + \beta_f}{1 + \left(\frac{X}{K_{df}}\right)^{n_f}} \cdot \frac{1}{1 + \left(\frac{Y}{K_{dr}}\right)^{n_r}} \left( K_m - M_r \cdot \beta_r + (K_m - M_r) \cdot \left(\frac{Y}{K_{dr}}\right)^{n_r} \right) \quad (S22.4)$$

We are interested in the case when  $K_m \approx M_r$ : Increasing the  $Y$  level causes to decrease the mRNA level only, without shifting the threshold (As shown in Eq. S22.4). Thus, in such conditions,  $Y$  acts as a pure subtraction.

Case 2:  $K_m + RNA_{Anti\_T} \gg mRNA_T$

For the case that  $M_r > K_m$ , and  $M_f$  is equal to  $K_m$ , the Eq. S22.1 is not valid and instead, we developed a new equation based on Eq. S21.:

$$\Rightarrow Complex = mRNA_T \cdot \frac{RNA_{Anti\_T}}{K_m + RNA_{Anti\_T}} \quad (S23.1)$$

$$\Rightarrow mRNA = mRNA_T - mRNA_T \cdot \frac{RNA_{Anti\_T}}{K_m + RNA_{Anti\_T}} \quad (S23.2)$$

$$\Rightarrow mRNA = mRNA_T \cdot \frac{K_m}{K_m + RNA_{Anti\_T}} \quad (S23.2)$$

$$\Rightarrow mRNA = M_f \cdot \frac{\left(\frac{X}{K_{df}}\right)^{n_f} + \beta_f}{1 + \left(\frac{X}{K_{df}}\right)^{n_f}} \cdot \frac{1}{1 + \frac{M_r}{K_m} \frac{\left(\frac{Y}{K_{dr}}\right)^{n_r} + \beta_r}{1 + \left(\frac{Y}{K_{dr}}\right)^{n_r}}} \quad (S23.3)$$

Here (Eq. S23.3), we can see that when  $M_r/K_m \gg 1$ : Increasing the Y level causes to decrease in the mRNA level, without shifting the threshold. Thus, in such conditions Y acts as a pure subtraction.

### Case 3: $K_m < mRNA_T + RNA_{Anti\_T}$

In this case,  $K_m$  is small but is not negligible compared to the mRNA levels. In this case, we directly used Eq. S21, and substituted it in Eq. S16.1

$$\Rightarrow mRNA = mRNA_T \cdot \frac{\frac{K_m + mRNA_T}{K_m + RNA_{Anti\_T} + mRNA_T}}{1 + \frac{mRNA_T}{K_m + RNA_{Anti\_T} + mRNA_T}} \quad (S24.1)$$

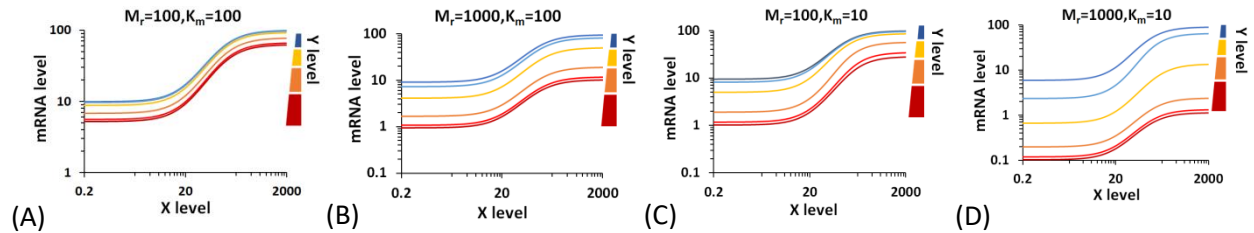
$$\Rightarrow mRNA = mRNA_T \cdot \frac{1 + \frac{mRNA_T}{K_m}}{1 + \frac{RNA_{Anti\_T}}{K_m} + \frac{mRNA_T}{K_m}} \quad (S24.2)$$

$$\Rightarrow mRNA = M_f \cdot \frac{\left(\frac{X}{K_{df}}\right)^{n_f} + \beta_f}{1 + \left(\frac{X}{K_{df}}\right)^{n_f}} \cdot \frac{\frac{1 + \frac{M_f}{K_m} \left(\frac{X}{K_{df}}\right)^{n_f} + \beta_f}{1 + \left(\frac{X}{K_{df}}\right)^{n_f}}}{1 + \frac{M_r}{K_m} \frac{\left(\frac{Y}{K_{dr}}\right)^{n_r} + \beta_r}{1 + \left(\frac{Y}{K_{dr}}\right)^{n_r}} + \frac{M_f}{K_m} \frac{\left(\frac{X}{K_{df}}\right)^{n_f} + \beta_f}{1 + \left(\frac{X}{K_{df}}\right)^{n_f}}} \quad (S24.3)$$

For  $M_f/K_m \gg 1$ , and  $M_r/K_m \gg 1$ :

$$mRNA = M_f \cdot \frac{\left(\frac{X}{K_{df}}\right)^{n_f} + \beta_f}{1 + \left(\frac{X}{K_{df}}\right)^{n_f}} \cdot \frac{\frac{1 + \frac{M_r}{K_m} \frac{\left(\frac{Y}{K_{dr}}\right)^{n_r} + \beta_r}{1 + \left(\frac{Y}{K_{dr}}\right)^{n_r}} + \frac{M_f}{K_m} \frac{\left(\frac{X}{K_{df}}\right)^{n_f} + \beta_f}{1 + \left(\frac{X}{K_{df}}\right)^{n_f}}}{1 + \frac{M_r}{K_m} \frac{\left(\frac{Y}{K_{dr}}\right)^{n_r} + \beta_r}{1 + \left(\frac{Y}{K_{dr}}\right)^{n_r}} + \frac{M_f}{K_m} \frac{\left(\frac{X}{K_{df}}\right)^{n_f} + \beta_f}{1 + \left(\frac{X}{K_{df}}\right)^{n_f}}}}{1 + \frac{M_r}{K_m} \frac{\left(\frac{Y}{K_{dr}}\right)^{n_r} + \beta_r}{1 + \left(\frac{Y}{K_{dr}}\right)^{n_r}} + \frac{M_f}{K_m} \frac{\left(\frac{X}{K_{df}}\right)^{n_f} + \beta_f}{1 + \left(\frac{X}{K_{df}}\right)^{n_f}}} \quad (S25)$$

According to Eq. S25, Y level only shifts the threshold and decreases the basal level, and thus, the FCA level increases when X increases.



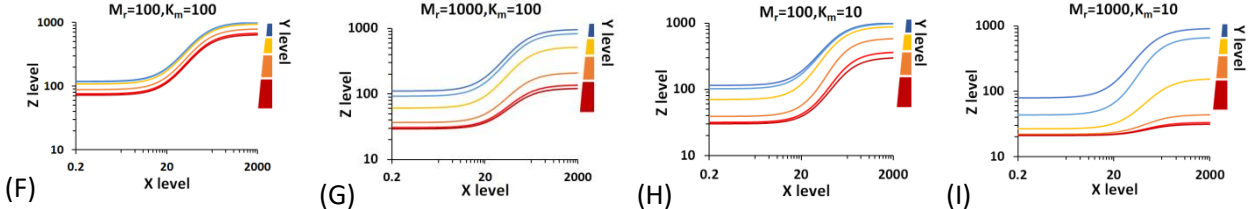


Fig. S9. Simulation results of antisense transcription model (Eqs. S18 to S20.2) as function of X levels (activity of forward promoter) and Y levels (activity of reverse promoter). Simulation parameters:  $n_f=1.5$ ,  $n_r=1.5$ ,  $K_{df}=100$ ,  $K_{dr}=100$ ,  $M_f=100$ ,  $\beta_f=0.1$ ,  $\beta_r=0.01$ ,  $Z_{max}=1000$ ,  $Z_{min}=20$ ,  $\alpha_Z \times \tau_Z=10$ .

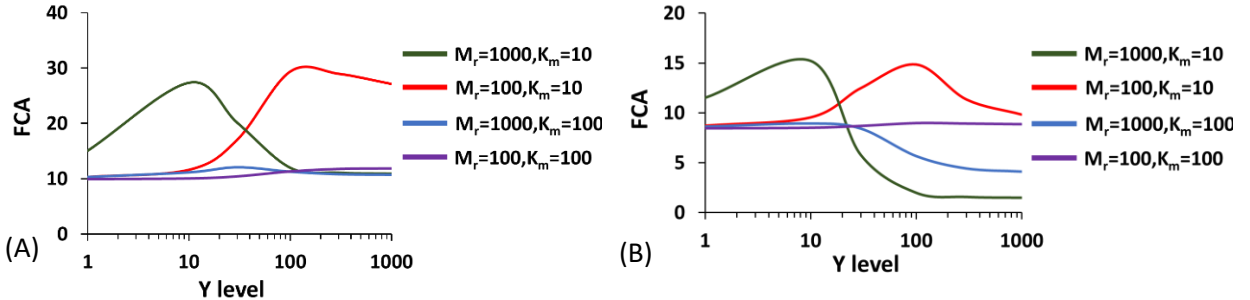


Fig. S10. Fold change activation (FCA) of the antisense transcription model as a function of the activity of reverse promoter (Y level), based on results Fig. S9, for (A) mRNA level, and (B) protein levels.

**2.2. Models for ICF design:** We developed two bio-models for the ICF design: (1) Molecular ICF using three nodes, which is based on biochemical reactions only, (2) Genetic ICF using four nodes, which is based on gene regulatory elements.

**2.2.1. Molecular ICF three-nodes model:** The next step was to develop a biomolecular model of the ICF circuit (Fig. S11) and test if this model is consistent with the models of the open loop circuits developed earlier in this work. The molecular ICF circuit comprise two branches (Fig. S11A): (1) the input molecule  $X$  activates the output molecule  $Z$ , and (2) the input molecule  $X$  inhibits the activity of molecule  $Y$ , which in turn inhibits the activity of  $Z$ . While both branches positively regulate the output  $Z$ , the first branch is a direct regulation of  $Z$ , and the second branch is an indirect regulation through cascading two inhibitors. The ICF circuit is also known as coherent feedforward type 4 (Mangan & Alon, 2003). The output signal of ICF is given by:

$$Z = Z_{max} \cdot \frac{\left(\frac{X}{K_{df}}\right)^{n_f} + \beta_f}{1 + \left(\frac{X}{K_{df}}\right)^{n_f}} \cdot \frac{1}{1 + \left(\frac{Y}{K_{dr}}\right)^{n_r}} \quad (\text{S26.1})$$

$$Y = Y_{max} \cdot \frac{1}{1 + \left(\frac{X}{K_{df}}\right)^{n_f}} \quad (\text{S26.2})$$

Here the  $Y_{max}$  is the maximum molecular level achieved in the regulation of molecule  $Y$  by  $X$ ,  $K_{dr}$  is the dissociation constant of binding  $Y$  and  $Z$ . The ratio  $Y_{max}/K_{dr}$  is the regulation strength of the second branch on the output  $Z$ . For simplicity, we assume that  $n_r=1$ , and by substituting the Eq. S26.2 into Eq. S26.1, we obtain:

$$Z = Z_{max} \cdot \frac{\left(\frac{X}{K_{df}}\right)^{n_f} + \beta_f}{1 + \left(\frac{X}{K_{df}}\right)^{n_f}} \cdot \frac{1 + \left(\frac{X}{K_{df}}\right)^{n_f}}{1 + \left(\frac{X}{K_{df}}\right)^{n_f} + \frac{Y_{max}}{K_{dr}}} + Z_{min} \quad (\text{S27.1})$$

$$Z = Z_{max} \cdot \frac{\left(\frac{X}{K_{df}}\right)^{n_f} + \beta_f}{1 + \left(\frac{X}{K_{df}}\right)^{n_f} + \frac{Y_{max}}{K_{dr}}} + Z_{min} \quad (\text{S27.2})$$

$$\Rightarrow FCA = \frac{Z|_{X>K_{df}}}{Z|_{X=0}} = \frac{1}{\beta_f} \cdot \left(1 + \frac{Y_{max}}{K_{dr}}\right) \quad (\text{S27.3})$$

The FCA given in Eq. S27.3 was calculated for  $Z_{min}=0$ , and it shows that increasing the  $Y_{max}/K_{dr}$  leads to increase in the FCA level. Eq. S27.1 is equivalent to Eq. S25 and Eq. S27.2 is equivalent to Eq. S14 when  $\rho_1=1$  and  $\rho_2=0$ , which means that our models of antisense transcription and transcriptional interference under specific conditions has similar equations as ICF circuit. The simulation results of molecular ICF circuit (Eq. S27) are shown in Fig. S11B for  $Z_{min}=0$  and Fig. S11C for  $Z_{min}\neq 0$ . Both indicate that FCA can be improved by increasing  $Y_{max}/K_{dr}$  level (Fig. S11D). We also presented the sensitivity in Fig. S11E for  $Z_{min}=0$  and Fig. S11F for  $Z_{min}\neq 0$  in order to evaluate the MDL. As we expected, improving the FCA by increasing the  $Y_{max}/K_{dr}$  level resulted in an increased MDL (Fig. S11G).

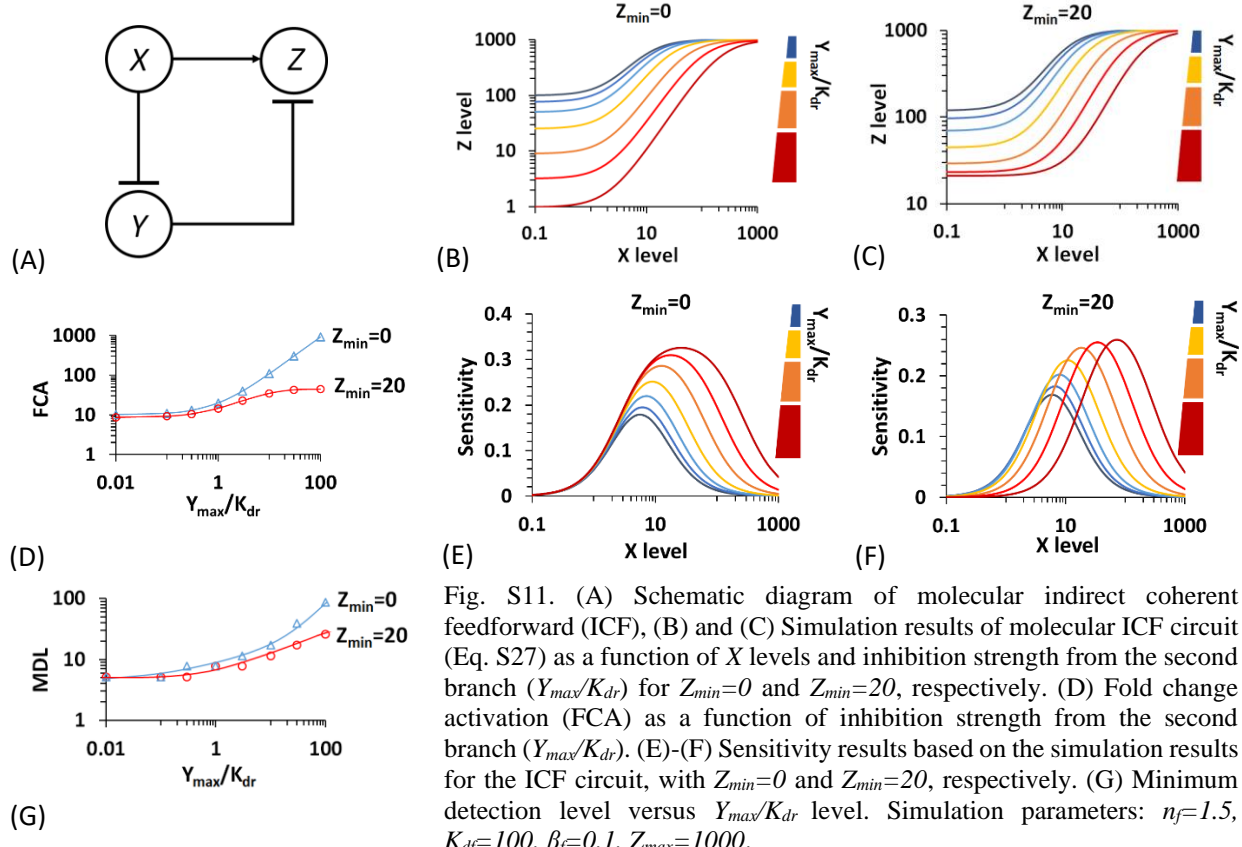


Fig. S11. (A) Schematic diagram of molecular indirect coherent feedforward (ICF). (B) and (C) Simulation results of molecular ICF circuit (Eq. S27) as a function of X levels and inhibition strength from the second branch ( $Y_{max}/K_{dr}$ ) for  $Z_{min}=0$  and  $Z_{min}=20$ , respectively. (D) Fold change activation (FCA) as a function of inhibition strength from the second branch ( $Y_{max}/K_{dr}$ ). (E)-(F) Sensitivity results based on the simulation results for the ICF circuit, with  $Z_{min}=0$  and  $Z_{min}=20$ , respectively. (G) Minimum detection level versus  $Y_{max}/K_{dr}$  level. Simulation parameters:  $n_f=1.5$ ,  $K_{df}=100$ ,  $\beta_f=0.1$ ,  $Z_{max}=1000$ .

**2.2.2. Genetic ICF four-nodes model:** The implementation of ICF in living cells using gene regulation requires another node, because transcription factors often can either repress or activate promoters (some synthetic parts can have dual operations, however the efficiency of these parts is low). Therefore, a node  $R$  is added to receive the positive regulation from  $X$  that directly represses  $Y$  (Fig. S12A). Fig. S12B shows the implementation of ICF using gene regulation based on antisense transcription model, where the output  $Z$  is given by:

$$Z = \alpha_Z \cdot \tau_Z \cdot (mRNA_T - Complex) + Z_{min} \quad (S19)$$

$$Complex = \frac{(mRNA_T + mRNA_{Anti\_T} + K_m) - \sqrt{(mRNA_T + mRNA_{Anti\_T} + K_m)^2 - 4 \cdot mRNA_T \cdot mRNA_{Anti\_T}}}{2} \quad (S18)$$

$$mRNA_T = M_f \frac{\left(\frac{X}{K_{df}}\right)^{n_f} + \beta_f}{1 + \left(\frac{X}{K_{df}}\right)^{n_f}} \quad (S20.1)$$

$$mRNA_{Anti\_T} = M_r \frac{\left(\frac{Y}{K_{dr}}\right)^{n_r} + \beta_r}{1 + \left(\frac{Y}{K_{dr}}\right)^{n_r}} \quad (S20.2)$$

$$R = R_{max} \frac{\left(\frac{X}{K_{df}}\right)^{n_f} + \beta_f}{1 + \left(\frac{X}{K_{df}}\right)^{n_f}} \quad (S28)$$

$$Y = Y_{max} \frac{1}{1 + \left(\frac{R}{K_R}\right)^{n_R}} \quad (S29)$$

As we showed earlier, the binding affinity ( $K_m$ ) between mRNA and antisense RNA can determine the functionality of antisense transcription genetic unit (Eq. S25, Fig. S9 and Fig. S10). For a strong binding affinity, the reverse promoter shifts the threshold and increases the FCA, similar to a comparator. For a weak binding affinity, the reverse promoter acts as subtraction, without increasing the FCA. Therefore, the implementation of ICF design using antisense transcription genetic unit can yield different FCA levels, based on the  $K_m$  value. In the circuit design, the forward promoter regulates the output signal and the transcription factor  $R$  (Fig. S12B). The repressor  $R$  regulates the activity of  $Y$ , which activates the antisense transcription unit from the reverse promoter  $P_{Rev}$ . The simulation results of ICF circuit using antisense transcription with a strong binding affinity ( $K_m$  is small), acting as a comparator, are shown in Fig. S12C for  $Z_{min}=0$  and in Fig. S12D for  $Z_{min} \neq 0$ . With a weak binding affinity ( $K_m$  is large), the ICF circuit acts as a subtractor. The results are shown in Fig. S12E for  $Z_{min}=0$  and in Fig. S12F for  $Z_{min} \neq 0$ . We also evaluated the FCA of this system, and in both cases for weak and strong binding affinities an improvement of the FCA was observed for a specific range  $K_R$  (Fig. S12G and H), where the  $K_R$  is the dissociation constant between repressor  $R$  and promoter  $P_R$ . Fig. S12I shows the simulation results for various molecules in the circuit as a function of  $X$  levels.

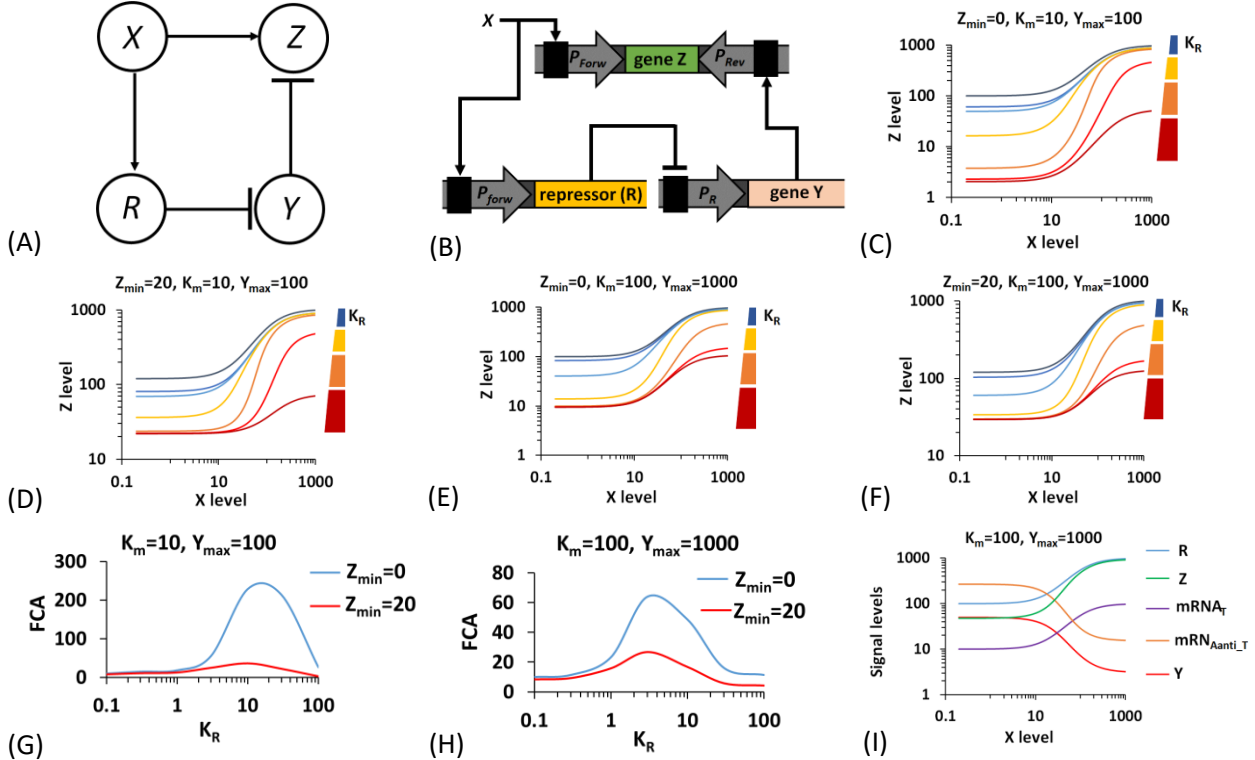


Fig. S12. (A) Schematic diagram of indirect coherent feedforward (ICF) in living cells using four nodes regulated by the input  $X$ . (B) The implementation of ICF design according to the diagram shown in A, based on antisense transcription. (C) and (D) Simulation results of output  $Z$  levels in ICF circuit (Eqs. S28) as a function of  $X$  levels. The circuit acts as a comparator. The dissociation constant between repressor  $R$  and promoter  $P_R$  ( $K_R$ ) is varied across levels with  $Z_{min}=0$  and  $Z_{min}=20$ , respectively. Simulation parameters are  $n_f=1.5$ ,  $n_r=1.5$ ,  $K_{df}=100$ ,  $K_{dr}=100$ ,  $M_f=100$ ,  $M_r=1000$ ,  $\beta_f=0.1$ ,  $\beta_r=0.01$ ,  $Z_{max}=1000$ ,  $Z_{min}=20$ ,  $\alpha_Z \times \tau_Z=10$ ,  $n_R=1.5$ ,  $Y_{max}=100$ ,  $K_m=10$ . (E) and (F) Simulation results of output  $Z$  levels in ICF circuit (Eqs. S28) as a function of  $X$  levels. The circuit acts as a subtractor. The dissociation constant between repressor  $R$  and promoter  $P_R$  ( $K_R$ ) is varied across levels with  $Z_{min}=0$  and  $Z_{min}=20$ , respectively. Simulation parameters are  $n_f=1.5$ ,  $n_r=1.5$ ,  $K_{df}=100$ ,  $K_{dr}=100$ ,  $M_f=100$ ,  $M_r=1000$ ,  $\beta_f=0.1$ ,  $\beta_r=0.01$ ,  $Z_{max}=1000$ ,  $Z_{min}=20$ ,  $\alpha_Z \times \tau_Z=10$ ,  $n_R=1.5$ ,  $Y_{max}=1000$ ,  $K_m=100$ . (G) FCA as a function of  $K_R$ , extracted from data that is shown in Fig. S12C and D. (H) FCA as a function of  $K_R$ , extracted from the data that is shown in Fig. S12E and F. (I) An example for all molecule levels in the ICF circuit based on antisense transcription.

Fig. S13A shows the implementation of ICF using gene regulation based on transcriptional interference model according to schematic diagram shown in Fig. S12A. The output  $Z$  is given by:

$$Z = Z_{max} \cdot \frac{\left(\frac{X}{K_{df}}\right)^{n_f} + \beta}{1 + \left(\frac{X}{K_{df}}\right)^{n_f} + \rho_1 \left(\frac{Y}{K_{dr}}\right)^{n_r} + \beta} \cdot \left( \frac{1}{1 + \rho_2 \cdot \left(\frac{Y}{K_{dr}}\right)^{n_r}} \right) + Z_{min} \quad (S14)$$

$$R = R_{max} \frac{\left(\frac{X}{K_{df}}\right)^{n_f} + \beta_f}{1 + \left(\frac{X}{K_{df}}\right)^{n_f}} \quad (S28)$$

$$Y = Y_{max} \frac{1}{1 + \left(\frac{R}{K_R}\right)^{n_R}} \quad (S29)$$

As we showed that values of  $\rho_1$  and  $\rho_2$  parameters in Eq. S29.1 can determine the functionality of the genetic unit, either shifting the threshold acting as a comparator or repressing the expression level acting as a subtractor. The implementation of an ICF design using transcriptional interference genetic unit is shown in Fig. S13A. The forward promoter regulates the output signal as well as the transcription factor  $R$ , which represses gene  $Y$ . The  $Y$  protein activates the reverse promoter of the transcriptional interference unit. Here we only examine the transcriptional interference unit as a subtractor. The simulation results of ICF design using a transcriptional interference model with  $\rho_1=0$ ,  $\rho_2=1$ , acting as a subtractor, are shown in Fig. S13B for  $Z_{min}=0$  and in Fig. S13C for  $Z_{min}\neq 0$ . The estimated FCA level of this system shows an improvement when  $Y_{max}$  level increases (Fig. S13E). By comparing the FCA of antisense transcription (Fig. S12H) and transcriptional interference models (Fig. S13D), we can find two major differences:

- (1) For  $Z_{min}=0$ , while the FCA level of antisense transcription has an optimum, the FCA level of transcriptional interference monotonically increases with respect to increasing strength activity of the reverse promoter.
- (2) For  $Z_{min}\neq 0$  and for the same reverse promoter activity, the FCA level of antisense transcription is higher than the FCA level of transcriptional interference.

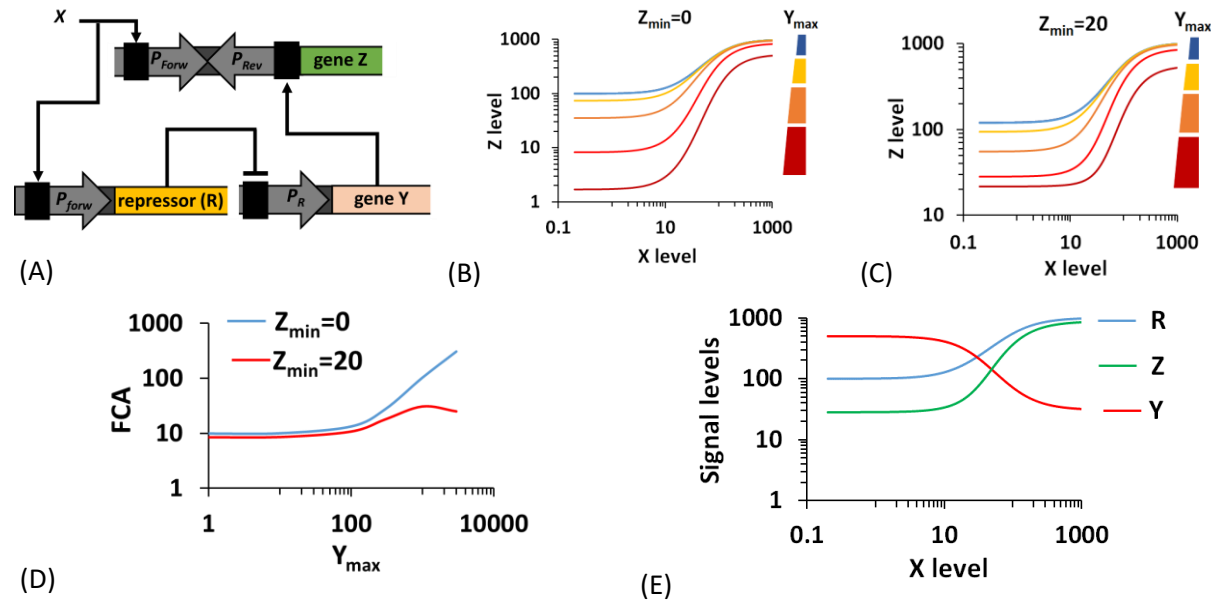


Fig. S13. (A) Implementation of ICF design according to the schematic diagram shown in Fig. S12A, using transcriptional interference model in living cells. (B) and (C) Simulation results of ICF circuit (Eqs. S29) acting as a subtractor, as a function of  $X$  levels. The maximum protein level ( $Y_{max}$ ) is varied by adjusting the repressor  $R$  for  $Z_{min}=0$ , and  $Z_{min}=20$ , respectively. Simulation parameters:  $n_f=1.5$ ,  $n_r=1.5$ ,  $K_{df}=100$ ,  $K_{dr}=100$ ,  $\beta=0.1$ ,  $Z_{max}=1000$ ,  $n_R=1.5$ ,  $K_R=100$ ,  $\rho_1=0$ , and  $\rho_2=1$ . (D) FCA level versus  $Y_{max}$ , extracted from the data that is shown in Fig. S13B and C. (E) An example for all molecular signals in the ICF circuit based on transcriptional interference.

**2.3. Models for DNF design:** We developed two bio-models for the DNF design: (1) Molecular DNF using three nodes, which is based on biochemical reactions only, (2) Genetic DNF using four nodes, which is based on gene regulatory elements.

**2.3.1. Molecular DNF three-nodes model:** The molecular DNF circuit is shown in Fig. S14A. In the circuit, an input molecule  $X$  activates the output molecule  $Z$ . The output  $Z$  inhibits the activity of the

molecule  $Y$ , which in turn inhibits the activity of  $Z$ , leading to a mutual negative feedback between  $Y$  and  $Z$  molecules. The output signal of DNF is given by:

$$Z = Z_{max} \cdot \frac{\left(\frac{X}{K_{df}}\right)^{n_f} + \beta_f}{1 + \left(\frac{X}{K_{df}}\right)^{n_f}} \cdot \frac{1}{1 + \left(\frac{Y}{K_{dr}}\right)^{n_r}} + Z_{min} \quad (\text{S30.1})$$

$$Y = Y_{max} \cdot \frac{1}{1 + \left(\frac{Z}{K_{dz}}\right)^{n_z}} \quad (\text{S30.2})$$

For simplicity we assume that  $n_r=1$ , and  $n_z=1$ ,  $Z_{min}=0$ :

$$Z = Z_{max} \cdot f(x) \cdot \frac{1}{1 + \frac{Y}{K_{dr}}} \quad (\text{S31.1})$$

$$Y = Y_{max} \cdot \frac{1}{1 + \frac{Z}{K_{dz}}} \quad (\text{S31.2})$$

Substituting Eq. S31.2 into Eq. S31.1:

$$Z + Z \cdot \frac{Y_{max}}{K_{dr}} \cdot \frac{1}{1 + \frac{Z}{K_{dz}}} = Z_{max} \cdot f(x) \quad (\text{S32.1})$$

$$Z \cdot \left(1 + \frac{Z}{K_{dz}}\right) + Z \cdot \frac{Y_{max}}{K_{dr}} = Z_{max} \cdot f(x) \cdot \left(1 + \frac{Z}{K_{dz}}\right) \quad (\text{S32.2})$$

$$Z^2 + Z \cdot K_{dz} \cdot \left(1 + \frac{Y_{max}}{K_{dr}} - \frac{Z_{max} \cdot f(x)}{K_{dz}}\right) = K_{dz} \cdot Z_{max} \cdot f(x) \quad (\text{S32.3})$$

$$Z = K_{dz} \cdot \frac{-\left(1 + \frac{Y_{max}}{K_{dr}} - \frac{Z_{max} \cdot f(x)}{K_{dz}}\right) + \sqrt{\left(1 + \frac{Y_{max}}{K_{dr}} - \frac{Z_{max} \cdot f(x)}{K_{dz}}\right)^2 + 4 \cdot \frac{Z_{max}}{K_{dz}} \cdot f(x)}}{2} \quad (\text{S32.4})$$

We then calculated the lowest and highest levels for  $Z$

$$Z_H|_{f(x \gg K_{df})=1} = K_{dz} \cdot \frac{-\left(1 + \frac{Y_{max}}{K_{dr}} - \frac{Z_{max}}{K_{dz}}\right) + \sqrt{\left(1 + \frac{Y_{max}}{K_{dr}} - \frac{Z_{max}}{K_{dz}}\right)^2 + 4 \cdot \frac{Z_{max}}{K_{dz}}}}{2} \quad (\text{S33.1})$$

$$Z_L|_{f(x \ll K_{df})=\beta} = K_{dz} \cdot \frac{-\left(1 + \frac{Y_{max}}{K_{dr}} - \frac{Z_{max} \cdot \beta}{K_{dz}}\right) + \sqrt{\left(1 + \frac{Y_{max}}{K_{dr}} - \frac{Z_{max} \cdot \beta}{K_{dz}}\right)^2 + 4 \cdot \frac{Z_{max} \cdot \beta}{K_{dz}}}}{2} \quad (\text{S33.2})$$

The FCA is defined as:  $FCD = \frac{Z_H}{Z_L}$ , and then, we obtain:

$$FCA = \frac{-\left(1 + \frac{Y_{max}}{K_{dr}} - \frac{Z_{max}}{K_{dz}}\right) + \sqrt{\left(1 + \frac{Y_{max}}{K_{dr}} - \frac{Z_{max}}{K_{dz}}\right)^2 + 4 \cdot \frac{Z_{max}}{K_{dz}}}}{-\left(1 + \frac{Y_{max}}{K_{dr}} - \frac{Z_{max} \cdot \beta}{K_{dz}}\right) + \sqrt{\left(1 + \frac{Y_{max}}{K_{dr}} - \frac{Z_{max} \cdot \beta}{K_{dz}}\right)^2 + 4 \cdot \frac{Z_{max} \cdot \beta}{K_{dz}}}} \quad (\text{S34})$$

The simulation results of molecular DNF are shown in Fig. S14B for  $Z_{min}=0$ . We also analyzed the sensitivity (Fig. S14C) and evaluated the MDL. As we expected, increasing the  $Y_{max}/K_{dr}$  level leads to improvement of the FCA level and worsening the MDL (Fig. S14D). Interestingly, when  $Z_{min}=0$ , the FCA of molecular DNF has an optimum over a range of  $Y_{max}$  level (Fig. S14E), in contrast to molecular ICF design (Fig. S11).

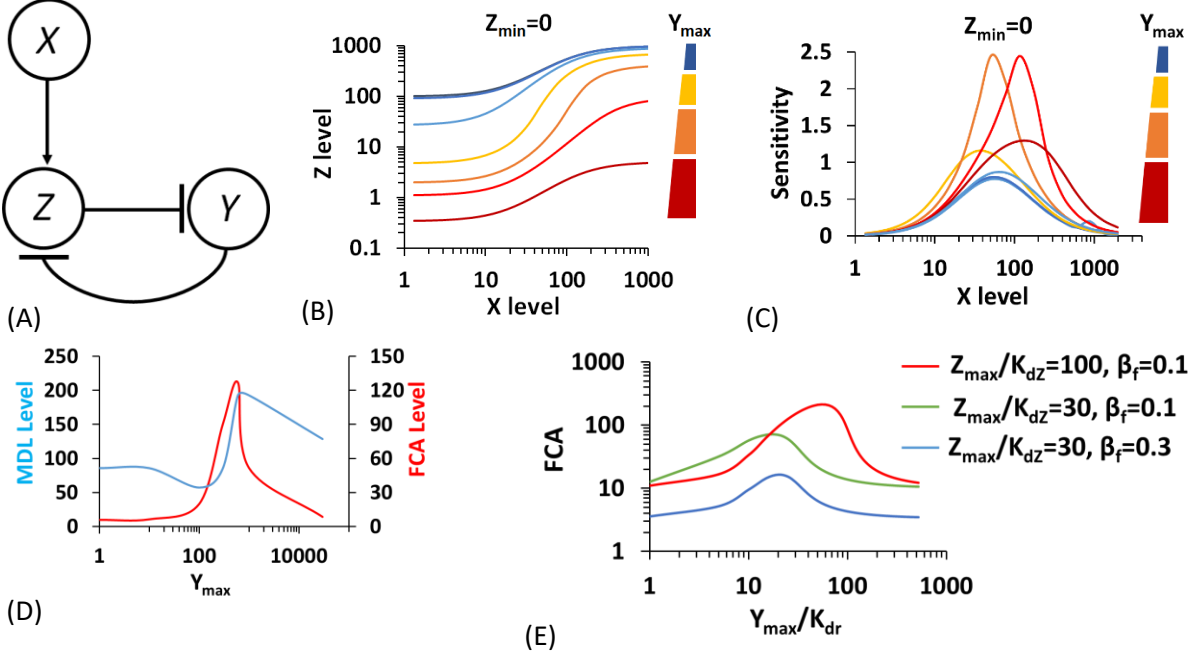


Fig. S14. (A) Schematic diagram of molecular double negative feedback (DNF) design, (B) Simulation results of molecular DNF circuit (Eq. S27) as a function of  $X$  levels for  $Z_{min}=0$ . The  $Y_{max}/K_{dr}$  represents the strength of negative feedback loop. (C) Sensitivity analysis based on the simulation results of molecular DNF circuit. (D) FCA and MDL levels as a function of feedback strength. (E) FCA levels for various circuit parameters. Simulation parameters are:  $n_f=1.5$ ,  $K_{df}=100$ ,  $\beta_f=0.1$ ,  $Z_{max}=1000$ ,  $K_{dz}=10$ ,  $K_{dr}=10$ .

**2.3.2. Genetic DNF four-nodes model:** Implementation of DNF in living cells using gene circuits requires another node as shown Fig. S15A. Here  $R$  and  $Z$  are both controlled by the same nodes ( $X$ ,  $Y$ ) and therefore have similar behavior. In our design,  $Z$  is used as a probe molecule ( $Z$ ). Fig. S15B shows the implementation of DNF using gene regulation based on antisense transcription model, where the output  $Z$  is given by:

$$Z = \alpha_Z \cdot \tau_Z \cdot (mRNA_T - Complex) + Z_{min} \quad (S19)$$

$$R = R_{max} \cdot (mRNA_T - Complex) \quad (S35)$$

$$Complex = \frac{(mRNA_T + RNA_{Anti\_T} + K_m) - \sqrt{(mRNA_T + RNA_{Anti\_T} + K_m)^2 - 4 \cdot mRNA_T \cdot RNA_{Anti\_T}}}{2} \quad (S18)$$

$$mRNA_T = M_f \frac{\left(\frac{X}{K_{df}}\right)^{n_f} + \beta_f}{1 + \left(\frac{X}{K_{df}}\right)^{n_f}} \quad (S20.1)$$

$$RNA_{Anti\_T} = M_r \frac{\left(\frac{Y}{K_{dr}}\right)^{n_r} + \beta_r}{1 + \left(\frac{Y}{K_{dr}}\right)^{n_r}} \quad (S20.2)$$

$$Y = Y_{max} \frac{1}{1 + \left(\frac{R}{K_R}\right)^{n_R}} \quad (S29)$$

The implementation of DNF design using antisense transcription genetic is shown in Fig. S15B. The forward promoter regulates the output signal as well as the repressor  $R$ , which represses the expression of gene  $Y$ . The protein  $Y$  activates the reverse promoter of the antisense transcription units, which are located downstream to gene  $Z$  and repressor  $R$ . Thus,  $R$  and  $Y$  comprise a double negative feedback. Here, we assumed that the binding affinity of mRNA- antisense mRNA is weak ( $K_m$  is large), and therefore, the antisense transcription unit acts as a subtractor. The simulation results of such systems are shown in Fig. S15C for  $Z_{min}=0$ , in Fig. S15D for  $Z_{min}\neq 0$ , and in Fig. S15E for  $Y$  signal. We also evaluated the FCA level of this system. In both cases for  $Z_{min}=0$  and  $Z_{min}\neq 0$ , an improvement of the FCA can be achieved for a range of  $K_R$  (Fig. S15.F). The  $K_R$  is the dissociation constant between repressor  $R$  and promoter  $P_{forw\_R}$ .

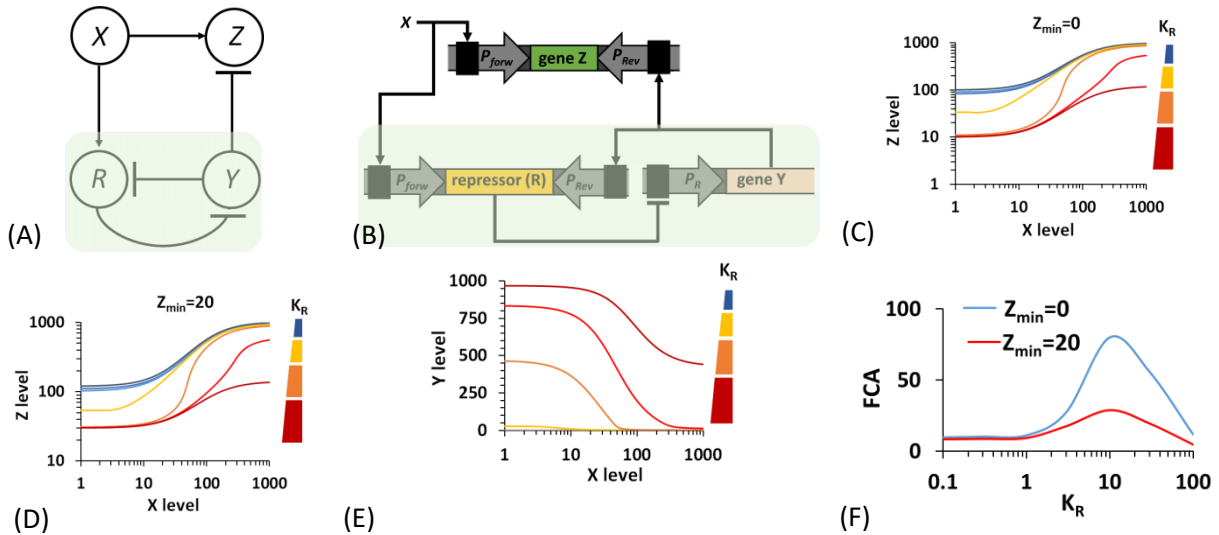


Fig. S15. (A) Schematic diagram of double negative feedback (DNF) design in living cells using four nodes. The area marked in green is the DNF loop. (B) The implementation of DNF design according to the diagram in A, using antisense transcription model in living cells. The area marked in green is the DNF loop. (C), (D) and (E) Simulation results of DNF circuit (Eqs. S35) as a function of  $X$  levels. The DNF circuit acts as a subtractor for various  $K_R$  values.  $K_R$  is the dissociation constant for the binding of repressor  $R$  to the promoter  $P_{R}$ . (C)  $Z$  level at  $Z_{min}=0$ . (D)  $Z$  level at  $Z_{min}=20$ . (E)  $Y$  level. Simulation parameters are:  $n_f=1.5$ ,  $n_r=1.5$ ,  $K_{df}=100$ ,  $K_{dr}=100$ ,  $M_f=100$ ,  $M_r=1000$ ,  $\beta_f=0.1$ ,  $\beta_r=0.01$ ,  $Z_{max}=1000$ ,  $Z_{min}=20$ ,  $\alpha_Z \times \tau_Z=10$ ,  $n_R=1$ ,  $Y_{max}=1000$ ,  $K_m=100$ . (F) FCA as a function of  $K_R$  derived from the data from Fig. S15C and D.

Fig. S16A shows the implementation of DNF using gene regulation based on transcriptional interference model according to schematic diagram shown in Fig. S15A. The output  $Z$  is given by:

$$Z = Z_{max} \cdot \frac{\left(\frac{X}{K_{df}}\right)^{n_f} + \beta}{1 + \left(\frac{X}{K_{df}}\right)^{n_f} + \rho_1 \cdot \left(\frac{Y}{K_{dr}}\right)^{n_r} + \beta} \cdot \left( \frac{1}{1 + \rho_2 \cdot \left(\frac{Y}{K_{dr}}\right)^{n_r}} \right) + Z_{min} \quad (S14)$$

$$R = R_{max} \cdot \frac{\left(\frac{X}{K_{df}}\right)^{n_f} + \beta}{1 + \left(\frac{X}{K_{df}}\right)^{n_f} + \rho_1 \cdot \left(\frac{Y}{K_{dr}}\right)^{n_r} + \beta} \cdot \left( \frac{1}{1 + \rho_2 \cdot \left(\frac{Y}{K_d}\right)^{n_r}} \right) \quad (S36)$$

$$Y = Y_{max} \frac{1}{1 + \left(\frac{R}{K_R}\right)^{n_R}} \quad (S29)$$

The forward promoter regulates the output signal and also the repressor  $R$ , which represses the expression of gene  $Y$ . The protein  $Y$  activates the reverse promoter of the transcriptional interference unit. The reverse promoter downregulates both the output signal (gene  $Z$ ) and the repressor  $R$ . As a result,  $R$  and  $Y$  comprise a double negative feedback. DNF circuit that uses transcriptional interference model with  $\rho_1=0$ ,  $\rho_2=1$ , acts as a comparator. The simulation results are shown in Fig. S16B for  $Z_{min}=0$  and in Fig. S16C for  $Z_{min}\neq 0$ . We also evaluated the FCA level of this system (Fig. S16E), which can reach an optimal value at a specific  $Y_{max}$  level (Fig. S16F)

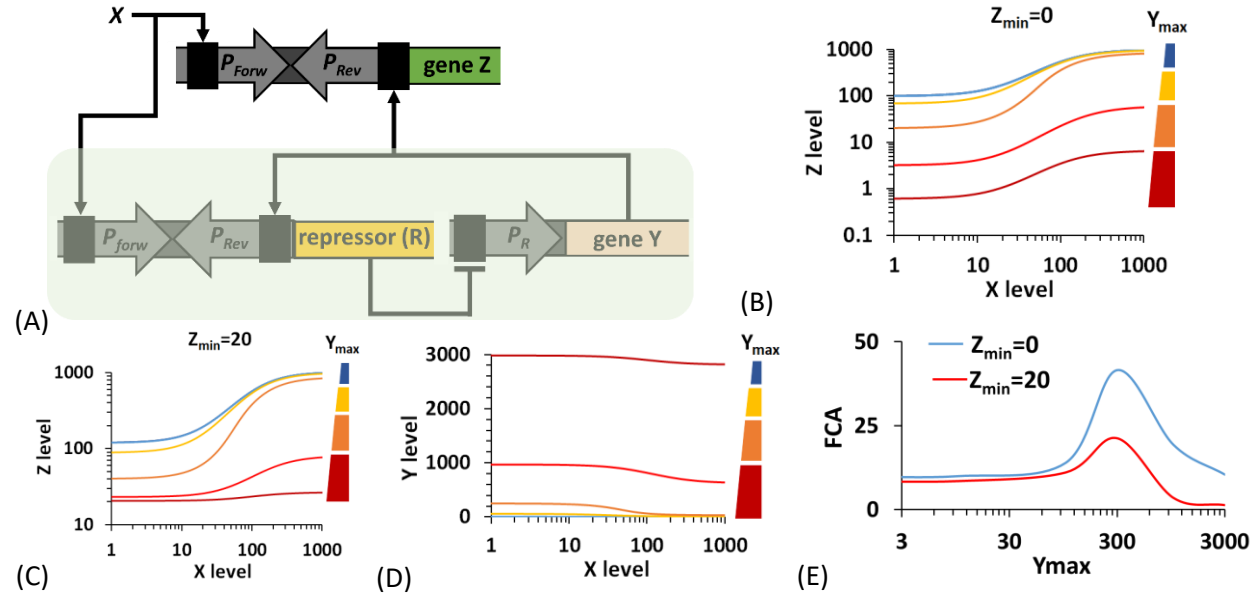


Fig. S16. (A) Implementation of DNF design according to the schematic diagram in Fig. S15A, using transcriptional interference model in living cells. The area marked in green is the DNF loop. (B), (C) and (D) Simulation results of DNF circuit (Eq. S36) as a function of  $X$  levels. The circuit acts as a subtractor and is regulated under various maximum levels of  $Y$  protein ( $Y_{max}$ ). (B) Output  $Z$  level when  $Z_{min}=0$ . (C) Output  $Z$  level when  $Z_{min}=20$ . (D)  $Y$  signals. Simulation parameters are  $n_f=1.5$ ,  $n_r=1.5$ ,  $K_{df}=100$ ,  $K_{dr}=100$ ,  $\beta=0.1$ ,  $Z_{max}=1000$ ,  $n_R=1.5$ ,  $K_R=100$ ,  $\rho_1=0$ , and  $\rho_2=1$ . (E) FCA level as a function of  $Y_{max}$  derived from the data from Fig. S15B and C.

### 3. Experimental results:

#### 3.1 The synthetic promoter $P_{BADsyn}$

The synthetic promoter  $P_{BADsyn}$  used in OL, ICF and DNF circuits contains only  $I_1$  and  $I_2$  binding sites, without  $O_2$  DNA sites.<sup>2</sup>

Various synthetic circuits sensitive to arabinose were transformed into bacterial cells, where arabinose-inducible synthetic promoter  $P_{BADsyn}$  (w/o  $O_2$  binding site for araC) was used as forward promoter and AHL-inducible promoter  $P_{lux}$  was used as a reverse promoter, located upstream to  $gfp$  gene. Arabinose and AHL

bind to their cognate transcriptional activators, araC and LuxR, generating complexes which bind to forward and reverse promoters, respectively. The transcriptional activator araC was constitutively expressed. LuxR was placed under the control of  $P_{tetO}$ , which functioned as a constitutive promoter when TetR wasn't included in the circuit .

Overnight grown bacterial cells containing and maintaining the circuit under test were diluted 50 times in the morning into fresh M9 minimal media and incubated for 2h before the induction with arabinose and additional inducers. Fluorescence was measured 3h after induction.

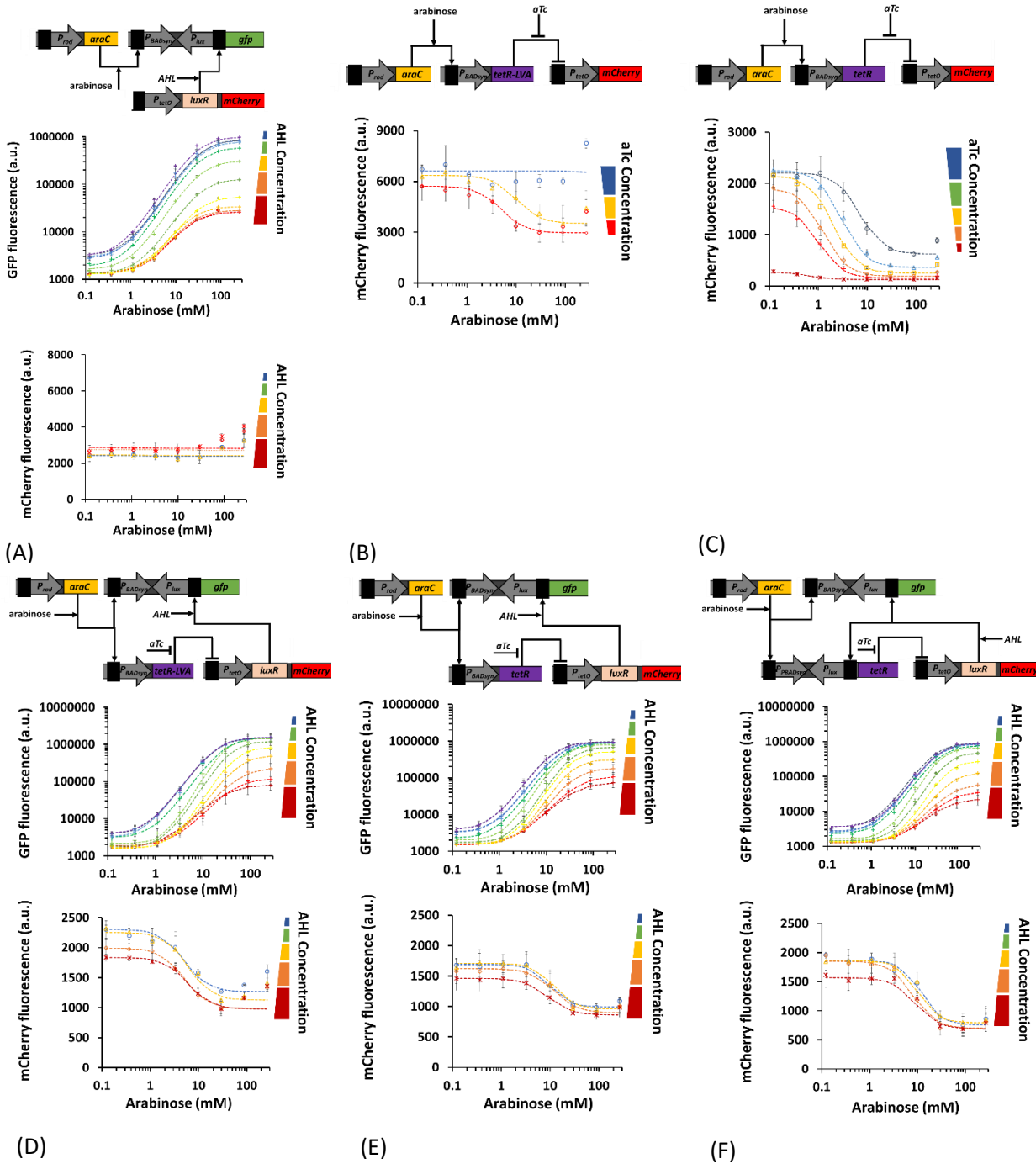


Fig. S17.  $P_{BADsyn}$  circuits in OL, ICF and DNF designs implemented using transcription interference. The upper panel contains the scheme for the synthetic circuit encompassing the promoter under test ( $P_{PUT}$ ) and the lower panel shows the measured fluorescence for the tested circuit (Flow cytometry data for building this figure is described in Fig. S24-S33).

- 3.1.1 OL: At high AHL concentrations, the transcription of GFP by RNAPs from forward promoter is inhibited upon binding of AHL-LuxR complexes to the reverse promoter  $P_{lux}$ . With higher AHL concentrations, the transcriptional interference becomes stronger. The transcriptional interference originated from this RNAPs collision could be detected by the reduction of both minimum and maximum promoter activities of synthetic  $P_{BADsyn}$ . LuxR is constitutively expressed along entire range of arabinose concentrations and remains constant at various AHL concentrations, as can be seen by mCherry levels (Fig. S17A).
- 3.1.2 Arabinose-aTc inverting switch (TetR-LVA): The activity of  $P_{tetO}$  represented by mCherry levels in response to arabinose can be adjusted under various concentrations of aTc. At intermediate aTc concentrations, mCherry level is repressed as arabinose concentration increases from low to high. At high aTc concentrations, more aTc-TetR-LVA complexes are formed and are released from promoter  $P_{tetO}$ , allowing transcription of mCherry. The LVA-degradation tag is responsible for reducing TetR (LVA) expression level and decreasing the ON/OFF ratio of  $P_{tetO}$  activity. An optimal concentration of anhydrotetracycline( aTc ) was deduced to give the highest ON/OFF ratio to work with in the ICF and DNF circuits (explained below in 3.1.4, 3.1.5 and 3.1.6). If no significant differences in mCherry levels were observed between different concentrations of aTc then no aTc was added in the ICF and DNF circuits. In addition, the mCherry gene was later replaced by LuxR-mCherry operon to be integrated with the transcriptional interference in ICF and DNF circuits (Fig. S17B).
- 3.1.3 Arabinose-aTc inverting switch (TetR): The same as in 3.1.2 but with TetR instead of TetR-LVA (Fig. S17C).
- 3.1.4 ICF-TetR-LVA: The arabinose-inducible synthetic promoter  $P_{BADsyn}$  was regulated by adjusting between its minimum expression level (basal level) and its maximum expression level (the ON state). The basal level was controlled through the activity of  $P_{lux}$  induced by AHL-LuxR complex. Whereas the maximum expression level was controlled by TetR-LVA protein, which represses the expression of LuxR. To regain the maximum promoter activity level of synthetic  $P_{BADsyn}$  that was reduced in OL (see 3.1.1) we engineered transcriptional repressor TetR-LVA regulated by synthetic  $P_{BADsyn}$ . When arabinose concentration is high the TetR-LVA levels are also high, which in turn bind to  $P_{tetO}$  promoter and inhibit LuxR expression, thereby arresting the transcriptional interference formed by RNAPs transcribing from the reverse promoter  $P_{lux}$  and reducing the strength of feedforward loop. At low arabinose concentrations, TetR-LVA levels are not sufficient to bind  $P_{tetO}$  to repress LuxR expression, therefore -AHL- LuxR complexes bind to the reverse promoter  $P_{lux}$ , inducing transcriptional interference and in turn increase the strength of the feedforward loop. This tuning is required to obtain low basal level at low arabinose concentration, and to reach maximum activity of promoter at high arabinose levels. The mCherry gene engineered downstream to LuxR under control of the same promoter  $P_{tetO}$ , acted as an indicator of  $P_{tetO}$  activity and LuxR levels. Thus, at low arabinose concentrations, LuxR and mCherry levels were high whereas at high arabinose concentrations, LuxR and mcherry levels were low. Overall, the combination of transcriptional interference with inverting switch improved the activity of  $P_{BADsyn}$  (Fig. S17D).
- 3.1.5 ICF-TetR: The same as in 3.1.4 but with TetR instead of TetR-LVA (Fig. S17E).

3.1.6 DNF-TetR: The same as in 3.1.4 but with TetR instead of TetR-LVA. AHL-inducible reverse promoter  $P_{lux}$  was also incorporated upstream to *tetR* gene. Thus, TetR levels were controlled not only by arabinose but also by AHL concentrations (Fig. S17F).

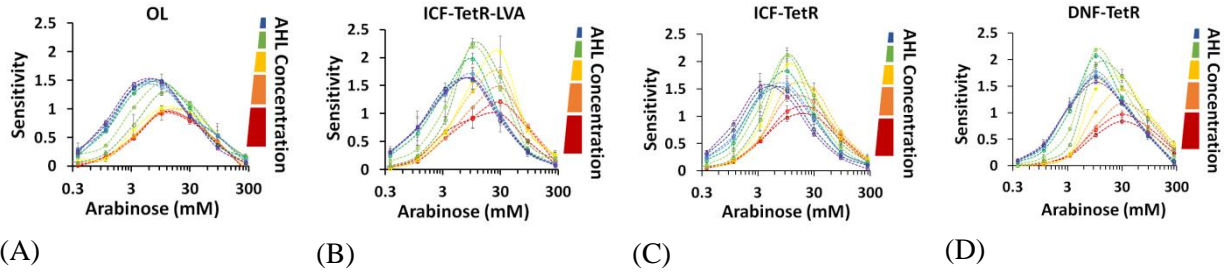


Fig. S18. Sensitivity analysis for various  $P_{BADsyn}$  circuits. The sensitivity analysis of OL (A), ICF-TetR-LVA (B), ICF-TetR (C) and DNF-TetR (D) circuits with a diagrams described in Fig. S17A, Fig. S17D, S17E and S17F, respectively. The results were calculated based on equation S3.

### 3.2 The synthetic promoter $P_{lacO}$

IPTG is a commonly used inducer for  $P_{lacO}$  as a lactose analog. A synthetic circuit sensitive for IPTG was implemented based on transcriptional interference.  $P_{lacO}$  was used as forward promoter and AHL-inducible promoter  $P_{lux}$  was used as the reverse promoter. LacI was constitutively expressed. IPTG binds to transcriptional repressor LacI and releases the complex of lacI-IPTG from forward promoter  $P_{lacO}$ , allowing the expression of GFP. AHL binds to its transcriptional activators LuxR, creating AHL-LuxR complexes, which bind the reverse promoter  $P_{lux}$ , thereby interfering with the transcription of  $P_{lacO}$  from the opposite direction. LuxR was placed under the control of  $P_{tetO}$ , which functioned as a constitutive promoter when TetR wasn't included in the circuit. An LVA-degradation tag was fused to LacI to increase LacI degradation.

Overnight grown bacterial cells containing and maintaining the circuit under test were diluted 100 times in the morning into fresh LB media and incubated for 0.5h before the induction with IPTG and additional inducers if required. Fluorescence was measured 4h after the induction.

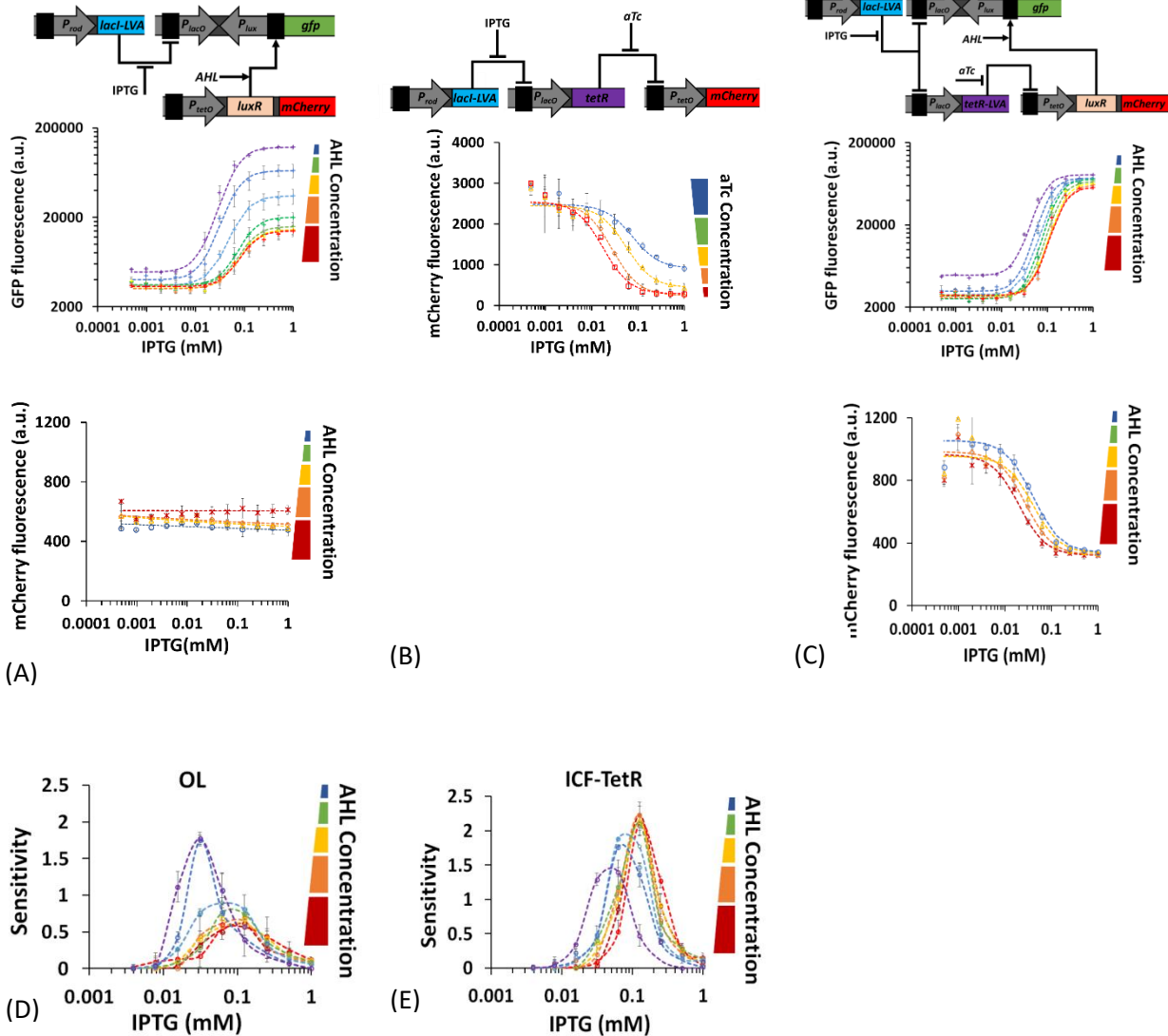


Fig. S19. Various  $P_{lacO}$  circuits implemented based on transcriptional interference. (A-C): The upper panel contains the scheme for the synthetic circuit encompassing the promoter under test  $P_{PUT}$  and the lower panel shows the measured fluorescence for the tested circuit. (D-E): The sensitivity analysis of OL and ICF-TetR-LVA circuits with schematic diagrams described in A and C, respectively. The results were calculated based on equation S3. ( Flow cytometry data for building this figure is described in Fig. S34-S38).

- 3.2.1 OL:** At high AHL concentrations, the transcription of GFP by RNAPs from forward promoter  $P_{lacO}$  is inhibited by RNAPs recruited by reverse promoter  $P_{lux}$  upon binding of AHL-LuxR complexes. With higher AHL concentrations, the transcriptional interference becomes stronger. The transcriptional interference could be detected by the reduction of both minimum and maximum promoter activity of  $P_{lacO}$ . LuxR is constitutively expressed through different concentrations of IPTG and can be seen by constant mCherry levels at different AHL concentrations (Fig. S19A).
- 3.2.2 IPTG-aTc inverting switch:** The activity of  $P_{tetO}$  in response to IPTG can be adjusted using different concentrations of aTc, and is reported by mCherry level. At intermediate aTc concentrations, mCherry level is decreased as IPTG concentration increases from low to high. At high aTc concentrations, more aTc-TetR-LVA complexes are formed and are released from promoter  $P_{lacO}$ ,

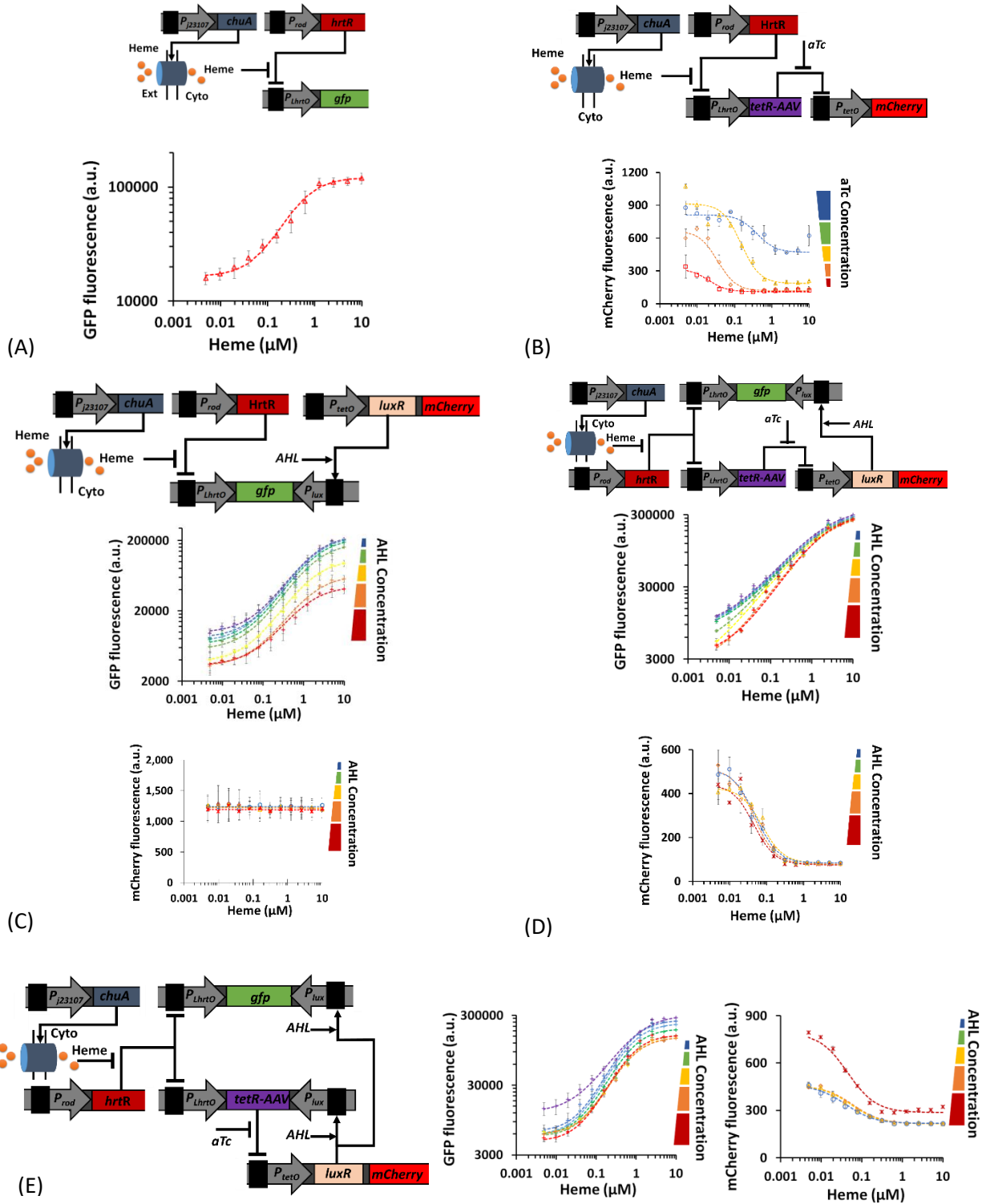
allowing transcription of mCherry. The LVA-degradation tag is responsible for reducing TetR-LVA expression. An optimal concentration of anhydrotetracycline( aTc ) was deduced to give the highest ON/OFF ratio to work with in the ICF circuit (explained below in 3.2.3). If no significant differences in mCherry levels between the various concentrations of aTc were observed, then no aTc was added in the ICF circuit. The mCherry gene was later replaced by LuxR-mCherry operon to be integrated with the transcriptional interference in ICF circuit (Fig. S19B).

3.2.3 ICF-TetR-LVA: The IPTG-inducible promoter  $P_{lacO}$  was regulated by adjusting between its minimum expression level ( basal level or the OFF state ) and its maximum expression level (the ON state). The basal level was controlled through the activity of  $P_{lux}$  induced by AHL-LuxR complex. Whereas the maximum expression level was controlled by TetR-LVA protein, which represses the expression of LuxR. To regain the maximum promoter activity level of  $P_{lacO}$  that was reduced in OL (see 3.2.1) we engineered transcriptional repressor TetR-LVA regulated by  $P_{lacO}$ . When IPTG concentration is high, the level of TetR-LVA levels is high, allowing TetR-LVA to bind the promoter  $P_{tetO}$  and reduce LuxR expression, thereby arresting the transcriptional interference formed by RNAPs transcribing from the reverse promoter  $P_{lux}$ . Reducing the strength of feedforward loop results in restoring the maximum activity of  $P_{lacO}$  at high IPTG levels. At low IPTG concentrations, TetR-LVA levels are not sufficient to bind  $P_{tetO}$  to repress LuxR expression. Thus, AHL-LuxR complexes activate reverse promoter  $P_{lux}$  and induce transcriptional interference, which in turn increase the strength of the feedforward loop. The mCherry gene engineered downstream to LuxR under control of the same promoter  $P_{tetO}$ , acted as an indicator of  $P_{tetO}$  activity and subsequently as indicator of LuxR levels. Thus, at low IPTG concentrations, LuxR and mCherry levels were high whereas at high IPTG concentrations, LuxR and mcherry levels were low. Overall, the combination of transcriptional interference with inverting switch improved the activity of  $P_{lacO}$  (Fig. S19C).

### 3.3 The native specific promoter $P_{LhrtO}$

Hemin or heme-group containing molecule, is a type of molecules commonly found in blood. A synthetic circuit sensitive for heme was transformed into bacterial cells, where heme-inducible promoter  $P_{LhrtO}$  was used as forward promoter and AHL-inducible promoter  $P_{lux}$  was used as reverse promoter engineered downstream to gene *gfp*. Heme enters bacterial cells through outer membrane protein ChuA and binds with the transcriptional repressor HrtR to form HrtR-heme complex, which is released from heme-inducible promoter  $P_{LhrtO}$  allowing the expression of genes that are regulated (Mimee et al., 2018). AHL binds with transcriptional activators LuxR, forming AHL- LuxR complexes, which bind reverse promoter  $P_{lux}$ . The transcriptional repressor HrtR and outer membrane protein ChuA were constitutively expressed. LuxR was placed under the control of  $P_{tetO}$ , which functioned as a constitutive promoter when TetR wasn't included in the circuit. The reverse promoter regulates the forward promoter through antisense transcription, in which one transcriptional unit interferes with the second transcriptional unit.

Overnight grown bacterial cells containing and maintaining the circuit under test were diluted 100 times in the morning into fresh LB media and incubated for 0.5h before the induction with heme and additional inducers. Fluorescence was measured 4h after induction with heme.



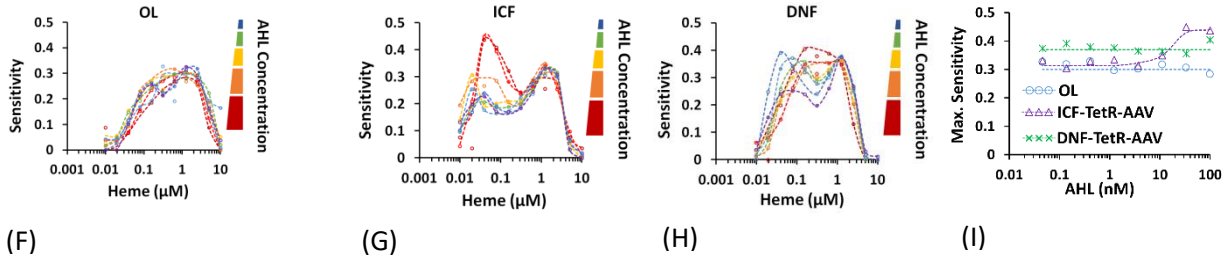


Fig. S20. Heme biosensor circuits implemented based on antisense transcription and sensitivity analyses for the circuits. (A)-(D): The upper panel contains the scheme for the synthetic circuit encompassing the promoter under test  $P_{PUT}$  and the lower panel shows the measured fluorescence for the tested circuit. (E): The left panel contains the scheme for the synthetic circuit encompassing the promoter under test  $P_{PUT}$  and the right panel shows the measured fluorescence for the tested circuit. (F-H): The sensitivity analysis of OL, ICF-TetR-AAV and DNF-TetR-AAV circuits with schematic diagrams described in C, D and E, respectively. (I) Maximum sensitivity for OL, ICF-TetR-AAV and DNF-TetR-AAV circuits. The results were calculated based on equation S3 (Flow cytometry data for building this figure is described in Fig. S39-S46).

3.3.1 Heme-sensing system. The expression of GFP is controlled by heme-inducible promoter  $P_{LhtO}$  (Fig. S20A).

3.3.2 OL: The higher the AHL concentrations, the larger the inhibition from antisense transcription. The effect of antisense transcription due to this specific design could be detected by the reduction of both minimum and maximum promoter activities of  $P_{LhtO}$ . LuxR is constitutively expressed and remained constant through different concentrations of heme at different concentrations of AHL as can be seen by mCherry levels (Fig. S20C).

3.3.3 Heme-aTc inverting switch (TetR-AAV): The activity of  $P_{tetO}$  represented by mCherry level in response to heme can be adjusted under various concentrations of aTc. At intermediate aTc concentrations, mCherry level is repressed as heme concentration increases from low to high (the yellow curve). At high aTc concentrations, more aTc-TetR-AAV complexes are formed, which are released from promoter  $P_{tetO}$  allowing transcription of mCherry. The AAV-degradation tag is responsible for reducing TetR expression levels. An optimal concentration of anhydrotetracycline (aTc) was deduced to give the highest ON/OFF ratio to work with in the ICF and DNF circuits (explained below in 3.3.4 and 3.3.5). If no significant differences in mCherry levels were observed between the various concentrations of aTc then no aTc was added in the ICF and DNF circuits. The mCherry gene was later replaced by LuxR-mCherry operon to be integrated in ICF and DNF circuits (Fig. S20B).

3.3.4 ICF-TetR-AAV: The heme-inducible promoter  $P_{LhtO}$  was regulated by adjusting between its minimum expression level (basal level) and its maximum expression level (the ON state). The basal level was controlled through the activity of reverse promoter  $P_{lux}$  induced by AHL-LuxR complex. Whereas the maximum expression level was controlled by TetR-AAV protein, which represses the expression of LuxR. To regain the maximum promoter activity level of  $P_{LhtO}$  that was reduced in OL (see 3.3.2) we engineered transcriptional repressor TetR-AAV under the control of  $P_{LhtO}$  to obtain high TetR-AAV levels when heme concentrations are high. In this way, TetR-AAV bind promoter  $P_{tetO}$  and inhibit LuxR expression, thereby decreasing the antisense transcription formed by RNAPs from the reverse promoter  $P_{lux}$  and reducing the strength of feedforward loop. Thus, the maximum activity of  $P_{LhtO}$  is restored at high heme levels. At low heme concentrations, TetR-AAV levels are

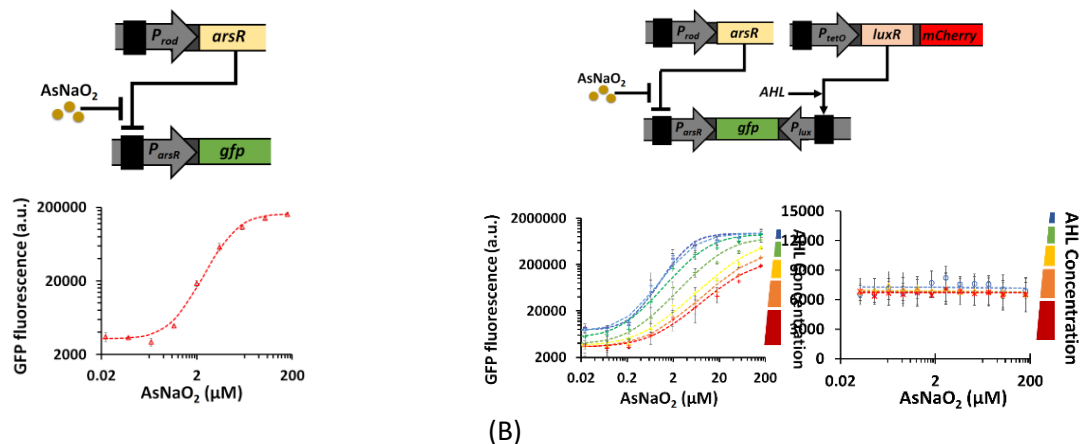
not sufficient to bind  $P_{tetO}$  to repress LuxR expression, therefore AHL-LuxR complexes bind to reverse promoter  $P_{lux}$  and activate antisense transcription, which in turn increase the strength of the feedforward loop. The mCherry gene engineered downstream to LuxR under control of the same promoter  $P_{tetO}$ , acted as an indicator of  $P_{tetO}$  activity and LuxR levels. Thus, at low heme concentrations LuxR and mCherry levels were high, whereas at high heme concentrations the LuxR and mcherry levels were low. Overall, the combination of transcriptional interference with inverting switch improved the activity of  $P_{LhtO}$  (Fig. S20D).

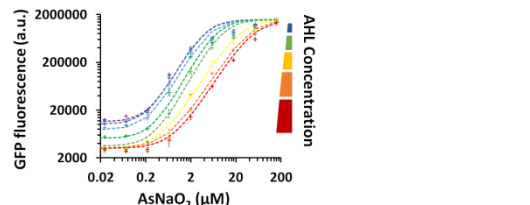
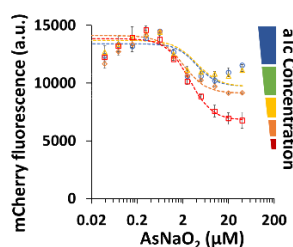
- 3.3.5 DNF-TetR-AAV: The same as 3.3.4 but with reverse promoter  $P_{lux}$  incorporated downstream to TetR-AAV. In this way TetR-AAV was controlled not only by heme but also by AHL concentrations (Fig. S20E).

### 3.4 The native specific promoter $P_{arsR}$

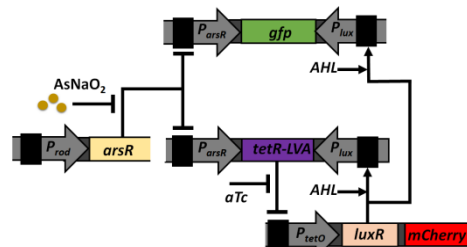
A synthetic circuit sensitive to arsenic was introduced into bacterial cells. The circuit was implemented using antisense transcription, where the forward promoter was an arsenic-inducible promoter  $P_{arsR}$  and the reverse promoter was an AHL-inducible promoter  $P_{lux}$ , engineered downstream to gene *gfp*. Transcriptional repressor *arsR* senses and binds with  $\text{AsNaO}_2$  molecule, forming *arsR*- $\text{AsNaO}_2$  complex, which is then released from forward promoter  $P_{arsR}$  to allow the expression of genes that are regulated. (Wan et al., 2019). AHL binds with its transcriptional activators LuxR, creating AHL-LuxR complexes, which activate reverse promoter  $P_{lux}$  and initiate antisense transcription from  $P_{lux}$ . The transcriptional repressor *arsR* were constitutively expressed. LuxR was placed under the control of  $P_{tetO}$ , which functioned as a constitutive promoter when TetR wasn't included in the circuit. The reverse promoter  $P_{lux}$  downregulates the forward promoter through antisense transcription, in which one transcriptional unit interferes with the second transcriptional unit.

Overnight grown bacterial cells containing and maintaining the circuit under test were diluted 100 times in the morning into fresh LB media and supplemented with  $\text{AsNaO}_2$  (Wan et al., 2019). The fluorescence was measured 5h after induction with  $\text{AsNaO}_2$  and additional inducers.

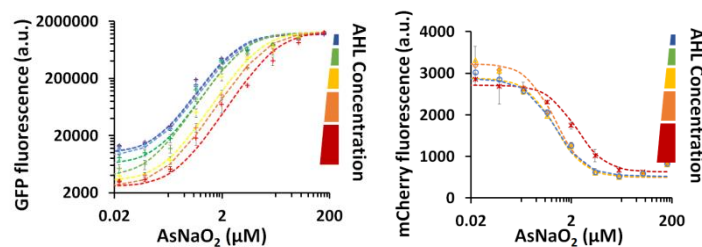




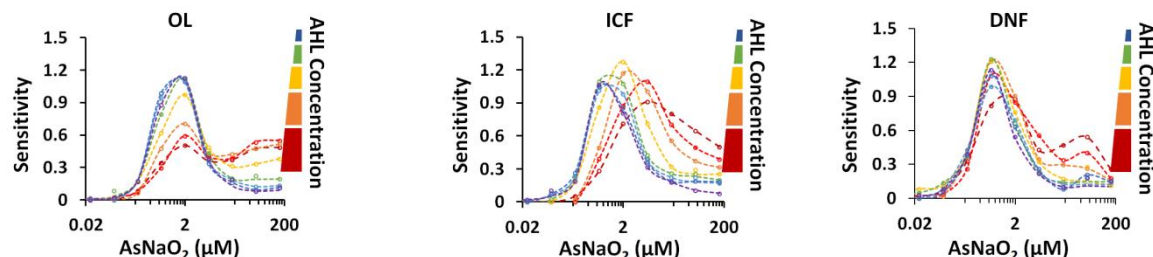
(C)



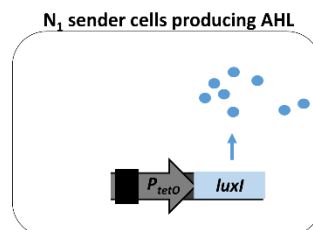
(D)



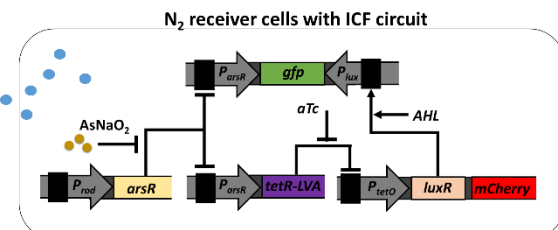
(E)



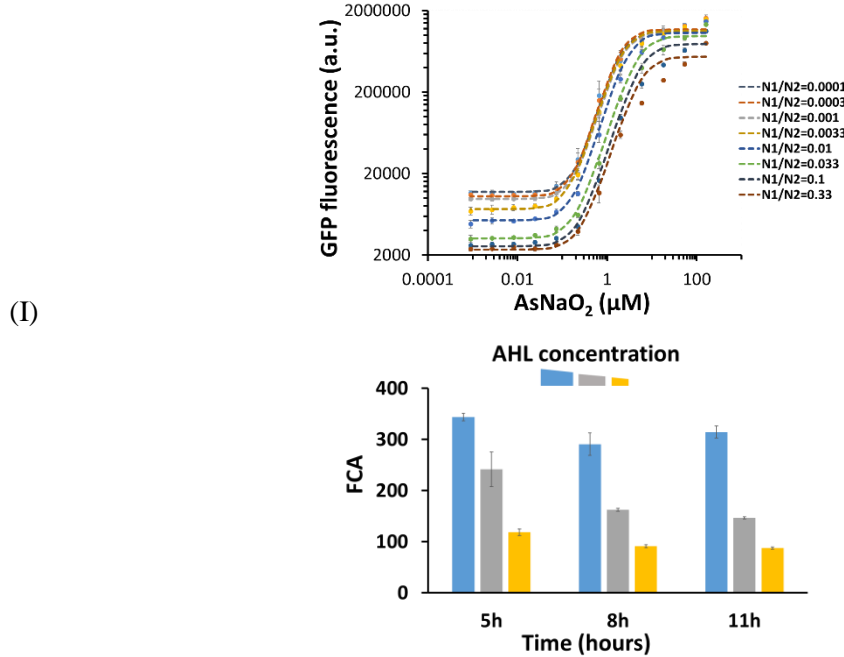
(F)



(G)



(H)



(J)

Fig. S21. Arsenic biosensing circuits and sensitivity analyses implemented based on antisense transcription. (A)-(D): The upper panel contains the scheme for the synthetic circuit encompassing the  $P_{arsR}$  as  $P_{PUT}$  and the lower panel shows the measured fluorescence for the tested circuit. (E): The left panel contains the scheme for the synthetic circuit encompassing the  $P_{arsR}$  as  $P_{PUT}$  and the right panel shows the measured fluorescence for the tested circuit. (F-H): The analysis sensitivity of OL, ICF-TetR-LVA and DNF-TetR-LVA circuits with schematic diagrams described in B, D and E, respectively. The results were calculated based on equation S3. (I) Cell-cell communication experiment between sender cells producing AHL and receiver cells containing the ICF circuit. The upper panel contains the scheme of the circuit and the lower panel shows the measured fluorescence for the communication circuit. The  $N_1$  sender cells produce AHL quorum-sensing molecule by constitutively expressing *luxI* gene.  $N_1$  strain contains two additional plasmids, we call them empty plasmids because they don't contain any part but used only to match the antibiotics used for  $N_2$  strain. The  $N_2$  strain contains the  $P_{arsR}$ -based ICF circuit. The various concentrations of AHL were obtained by mixing the strains  $N_1$  and  $N_2$  in different ratios. As the ratio  $N_1/N_2$  increases the AHL concentration also is increased. This experiment demonstrates how ICF circuit can operate without the need of adding AHL externally. (J) Kinetics experiment made at several time points that demonstrates that ICF circuit can be optimized by AHL and operate for extended periods of time ( Flow cytometry data for building this figure is described in Fig. S47-S53).

3.4.1 Arsenic-sensing system from *E. coli*. The expression of GFP is controlled by arsenic-inducible promoter  $P_{arsR}$  (Fig. S21A).

3.4.2 OL: The higher the AHL concentrations, the stronger is the strength of inhibition due to antisense transcription. The antisense transcription originated from this special orientation could be detected by the reduction of both minimum and maximum promoter activity of  $P_{arsR}$ . LuxR is constitutively expressed through different concentrations of AsNaO<sub>2</sub> and AHL which can be seen by constant mCherry levels at different AHL concentrations (Fig. S21B).

3.4.3 AsNaO<sub>2</sub>-aTc inverting switch: At intermediate aTc concentrations, mCherry level becomes repressed as AsNaO<sub>2</sub> concentration increases from low to high. At high aTc concentrations, more aTc-TetR-LVA complexes are formed, which are released from promoter  $P_{tetO}$ , allowing transcription of mCherry. The LVA-degradation tag is responsible for reducing TetR-LVA expression levels. An optimal

concentration of anhydrotetracycline( aTc ) was deduced to give the highest ON/OFF ratio to work with in the ICF and DNF circuits (explained below in 3.4.4 and 3.4.5). If no significant differences in mCherry levels were observed between the various concentrations of aTc then no aTc was added in the ICF and DNF circuits. The mCherry gene was later replaced by LuxR-mCherry operon to be integrated with the antisense transcription in ICF and DNF circuits (Fig. S21C).

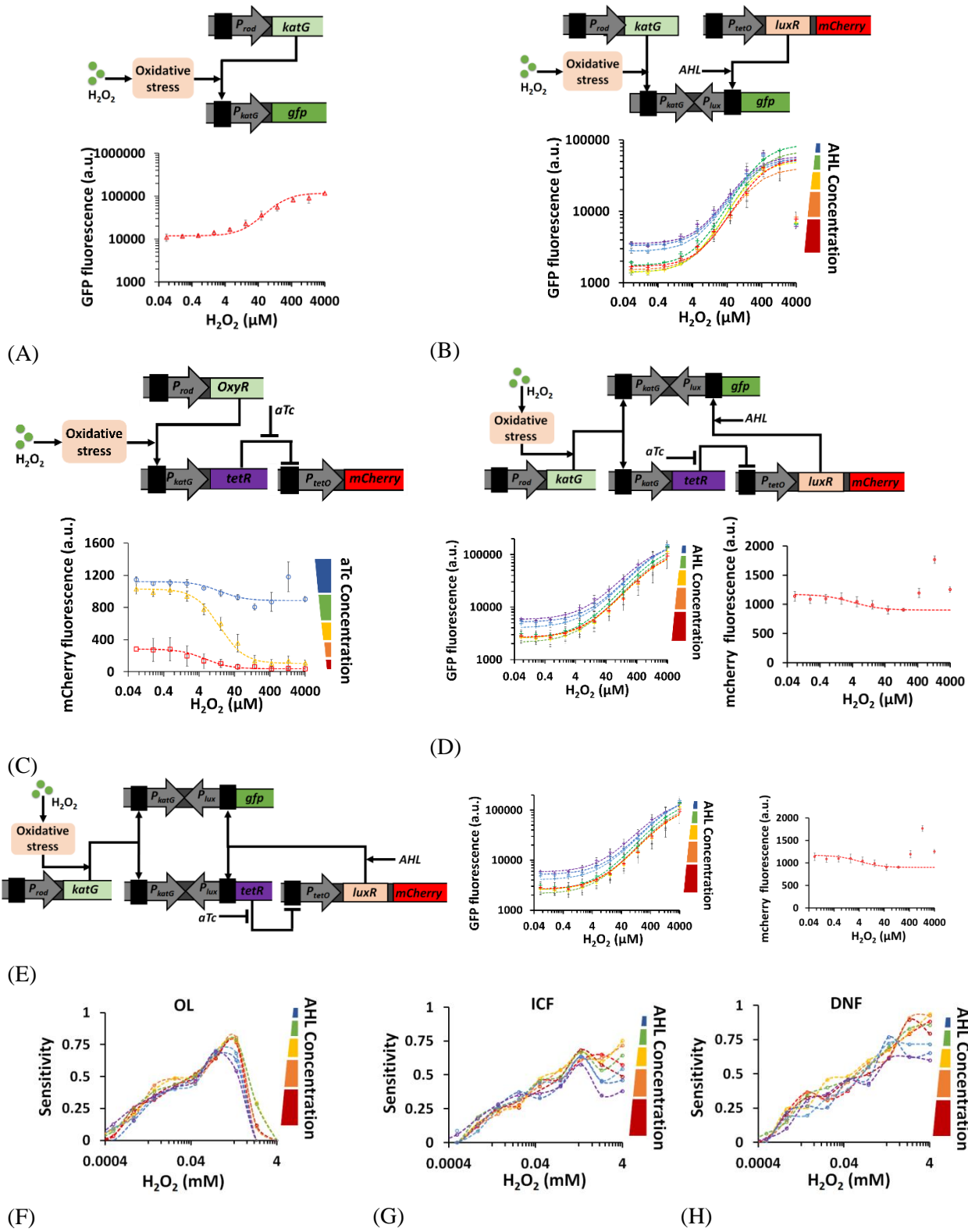
- 3.4.4 ICF-TetR-LVA based on antisense transcription. The arsenic-inducible promoter  $P_{arsR}$  was regulated by adjusting between its minimum expression level ( basal level ) and its maximum expression level ( the ON state). The basal level was controlled through the activity of  $P_{lux}$  induced by AHL-LuxR complex. Whereas the maximum expression level was controlled by TetR-LVA protein, which represses the expression of LuxR. To regain the maximum promoter activity level of  $P_{arsR}$  that was reduced in OL (see 3.4.2), we engineered transcriptional repressor TetR-LVA under the control of  $P_{arsR}$  to obtain high TetR-LVA levels when AsNaO<sub>2</sub> concentration is high. In this way, high levels of TetR-LVA binds promoter  $P_{tetO}$  and inhibit LuxR expression. The decreasing level of LuxR reduces the antisense transcription formed by RNAPs transcribing from the reverse promoter  $P_{lux}$ , as well as the strength of feedforward loop, thereby restoring the maximum activity of  $P_{arsR}$  at high AsNaO<sub>2</sub> levels. At low AsNaO<sub>2</sub> concentrations, TetR-LVA levels are not sufficient to bind  $P_{tetO}$  to repress LuxR expression, therefore AHL-LuxR complexes bind to reverse promoter  $P_{lux}$  to induce antisense transcription, which in turn increase the strength of the feedforward loop. The mCherry gene engineered downstream to LuxR under control of the same promoter  $P_{tetO}$ , acted as an indicator of  $P_{tetO}$  activity and LuxR levels. In this way, at low AsNaO<sub>2</sub> concentrations LuxR and mcherry levels were high, whereas at high AsNaO<sub>2</sub> concentrations the LuxR and mcherry levels were low. Overall, the combination of transcriptional interference with inverting switch improved the activity of  $P_{arsR}$  (Fig. S21D).
- 3.4.5 DNF-TetR-LVA based on antisense transcription. The same as in D but with reverse promoter  $P_{lux}$  incorporated downstream to TetR-LVA. In this way, TetR-LVA was controlled not only by AsNaO<sub>2</sub> but also by AHL concentrations (Fig. S21E).

### 3.5 The native stress promoter $P_{katG}$

Hydrogen peroxide, H<sub>2</sub>O<sub>2</sub>, cause oxidative stress to cells inflicting damage to proteins, nucleic acid, lipids and membranes. Upon exposure of the bacterial cells to H<sub>2</sub>O<sub>2</sub> at least 30 antioxidant genes are induced when half of them being activated by transcriptional activator OxyR (Aslund et al., 2002; Belkin et al., 1996). A synthetic circuit sensitive to oxidative stress was inserted into bacterial cells. In this native stress circuit, the H<sub>2</sub>O<sub>2</sub>-inducible promoter  $P_{katG}$  was used as forward promoter and AHL-inducible promoter  $P_{lux}$  was used as the reverse promoter, comprising the transcriptional interference. H<sub>2</sub>O<sub>2</sub> and AHL bind to their cognate transcriptional activators, OxyR and LuxR, generating complexes, which bind to the forward and reverse promoters, respectively. The transcriptional activator OxyR is constitutively expressed. LuxR was placed under the control of  $P_{tetO}$ , which functioned as a constitutive promoter where TetR wasn't included in the circuit .

Overnight grown bacterial cells containing and maintaining the circuit under test were diluted 50 times in the morning into fresh M9 minimal media and incubated for 3h before the induction with H<sub>2</sub>O<sub>2</sub> and additional inducers if needed. H<sub>2</sub>O<sub>2</sub> was added to the media every one hour for two times more, to enable 4 hours needed for response to AHL and aTc, since the H<sub>2</sub>O<sub>2</sub> is degraded by a product of *KatG* gene

(Panek & Brian, 2004) and has a peak at about 50min followed by signal reduction (Barger et al., 2019; Belkin et al., 1996). Fluorescence was measured 2.5h after the last induction.



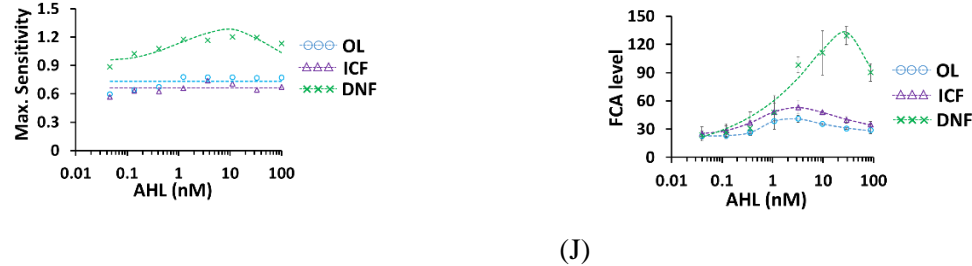


Fig. S22. KatG biosensing circuits based on transcriptional interference and corresponding sensitivity analyses. (A)-(D): The upper panel contains the scheme for the synthetic circuit encompassing the promoter under test  $P_{PUT}$  and the lower panel shows the measured fluorescence for the tested circuit. (E): The left panel contains the scheme for the synthetic circuit encompassing the promoter under test  $P_{PUT}$  and the right panel shows the measured fluorescence for the tested circuit. (F-H): The sensitivity analysis of OL, ICF and DNF circuits with schematic diagrams described in B, D and E. (I): Maximum sensitivity of OL, ICF and DNF circuits. The results were calculated based on equation S3. (J) FCA of OL, ICF and DNF circuits as function of  $F_S$  strengths, which are controlled by AHL levels (Flow cytometry data for building this figure is described in Fig. S54-S58).

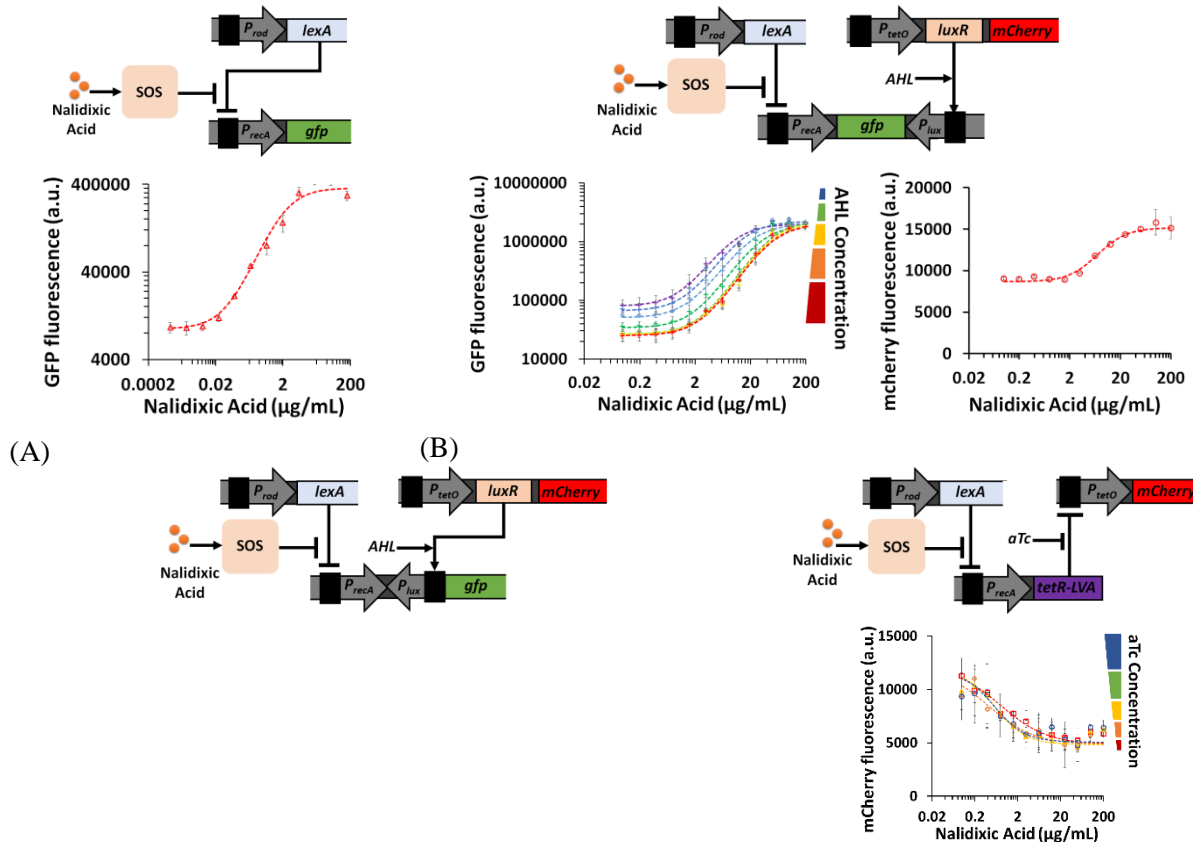
- 3.5.1  $H_2O_2$ -sensing system from *E. coli*. The expression of GFP is controlled by  $H_2O_2$ -inducible promoter  $P_{katG}$  (Fig. S22A).
- 3.5.2 OL: At high AHL concentrations, the transcription of GFP by RNAPs from forward promoter  $P_{katG}$  is inhibited by the reverse promoter  $P_{lux}$ , creating transcriptional interference that can be detected by the reduction of minimum and maximum promoter. The higher the AHL concentrations, the stronger is the strength of transcriptional inhibition (Fig. S22B).
- 3.5.3  $H_2O_2$ -aTc inverting switch. At intermediate aTc concentrations, the mCherry level is repressed as concentration increases from low to high. At high aTc concentrations, more aTc-TetR complexes are formed, which are released from promoter  $P_{tetO}$ , allowing transcription of mCherry. An optimal concentration of anhydrotetracycline (aTc) was deduced to give the highest ON/OFF ratio to work with in following circuits (explained below in 3.5.4 and 3.5.5). If no significant differences in mCherry levels were observed between the various concentrations of aTc then no aTc was added in the ICF and DNF circuits. The mCherry gene was later replaced by LuxR-mCherry operon to be integrated with the transcriptional interference in ICF and DNF circuits (Fig. S22C).
- 3.5.4 ICF-TetR. The  $H_2O_2$ -inducible promoter  $P_{katG}$  was regulated by adjusting between its minimum expression level (basal level) and its maximum expression level (the ON state). The basal level was controlled through the activity of  $P_{lux}$  induced by AHL-LuxR complex. Whereas the maximum expression level was controlled by TetR protein, which represses the expression of LuxR. To regain the maximum promoter activity level of  $P_{katG}$  that was reduced in OL (see 3.5.2), we designed the transcriptional repressor TetR to be under control of  $H_2O_2$ -inducible promoter  $P_{katG}$ . At high  $H_2O_2$  concentrations, the TetR levels are high, increasing the binding of TetR to  $P_{tetO}$  and reducing the LuxR levels, thereby inhibiting transcriptional interference from  $P_{lux}$ . At low  $H_2O_2$  concentrations, TetR levels are not sufficient and therefore allow binding of AHL-LuxR complex with antisense promoter  $P_{lux}$ , inducing transcriptional interference and inhibiting the transcription of  $P_{katG}$ . The mCherry gene engineered downstream to LuxR under control of the same promoter  $P_{tetO}$ , acted as an indicator of  $P_{tetO}$  activity and LuxR levels. In this way, at low  $H_2O_2$  concentrations LuxR and mCherry levels were high, whereas at high  $H_2O_2$  concentrations the LuxR and mCherry levels were low. LuxR levels exhibited high expression at high  $H_2O_2$  concentration. The reason for this effect could be because the autofluorescence of the cells is enhanced when the bacterial cells are in stress (Surre et al., 2018) (Fig. S22D).

3.5.5 DNF-TetR: The same as in 3.5.4 with the addition of reverse promoter  $P_{lux}$  to control TetR levels. In this way TetR was controlled not only by  $H_2O_2$  but also by AHL concentrations (Fig. S22E).

### 3.6 The native stress promoter $P_{recA}$

Nalidixic acid (NA) is an inhibitor of DNA gyrase enzyme required for DNA replication in living cells. Treatment with NA induces DNA damage through SOS response in which 30 genes are being de/activated upon autocleavage of the SOS-transcriptional repressor LexA by product of gene *recA* (Davidov et al., 2000; Vollmer et al., 1997). A synthetic circuit sensitive to SOS response was transformed into MG1655 *E. coli* cells since the strain 10-beta *E. coli* has mutations in *recA* gene. In this circuit, NA activates indirectly promoter  $P_{recA}$ , which was used as a forward promoter. AHL-inducible promoter  $P_{lux}$  was used as reverse promoter engineered either upstream to *gfp* gene for transcriptional interference or downstream to *gfp* gene for antisense transcription. AHL binds to its transcriptional activators LuxR, creating AHL-LuxR complexes which bind to reverse promoter  $P_{lux}$ . A gene *lexA* was used as transcriptional repressor (Little et al., 1981). The transcriptional repressor LexA was constitutively expressed. LuxR was placed under the control of  $P_{tetO}$ , which functioned as a constitutive promoter when TetR wasn't included in the circuit.

Overnight grown bacterial containing and maintaining the circuit under test cells were diluted 50 times in the morning into fresh M9 minimal media and incubated for 3.5h before the induction with NA and additional inducers. Fluorescence was measured 3.5h after the induction.



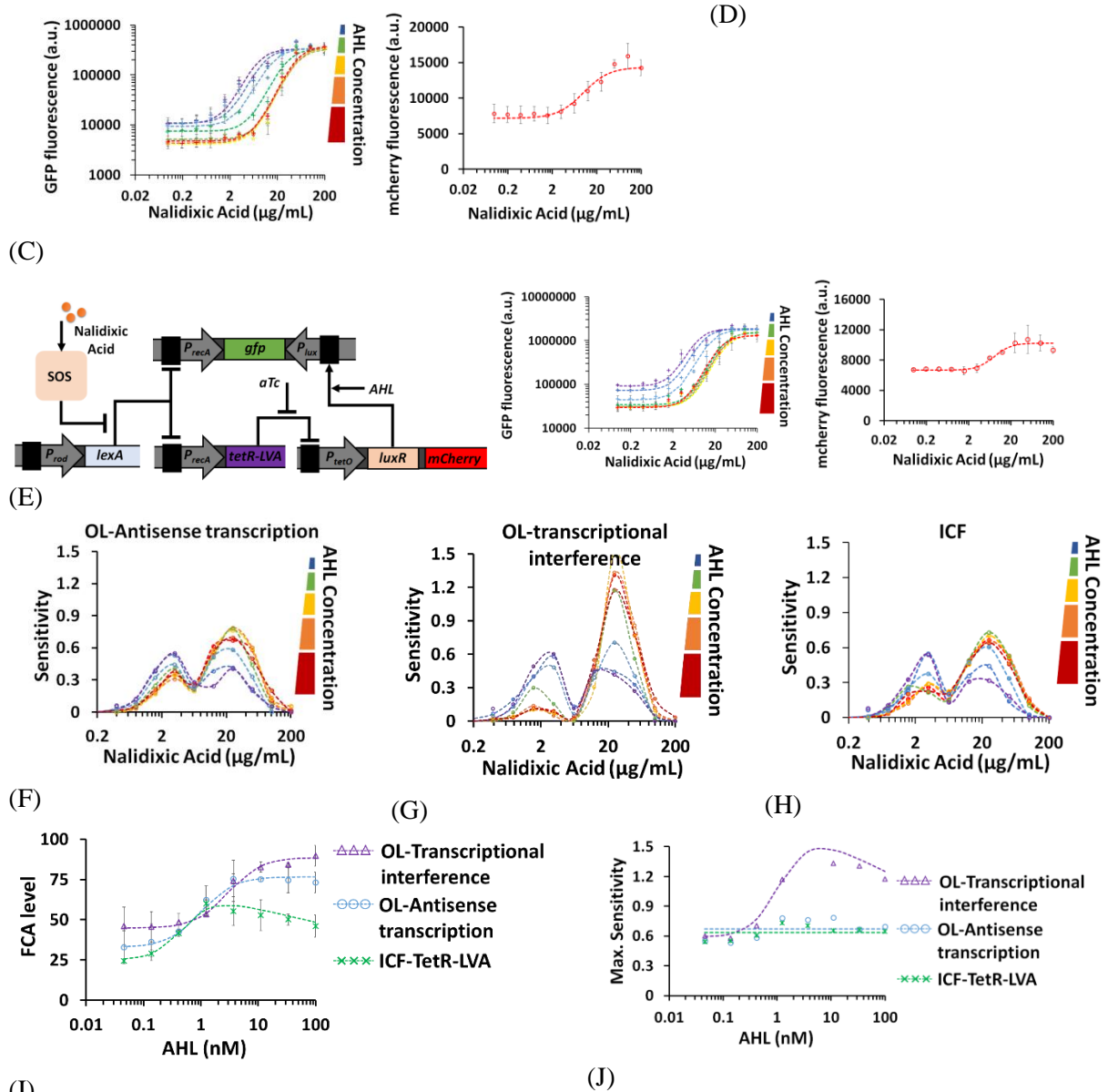


**Fig. S23.  $P_{recA}$  biosensing circuits and corresponding sensitivity analyses.** (A)-(D): The upper panel contains the scheme for the synthetic circuit encompassing the promoter under test  $P_{PUT}$  and the lower panel shows the measured fluorescence for the tested circuit. (E): The left panel contains the scheme for the synthetic circuit encompassing the promoter under test  $P_{PUT}$  and the right panel shows the measured fluorescence for the tested circuit. (F-H): The sensitivity analysis of antisense transcription based OL, transcriptional interference based OL and ICF-TetR-LVA circuits with schematic diagrams described in B, C and E, respectively. The results were calculated based on equation S3. (I) FCA for antisense transcription based OL circuit, transcriptional Interference based OL circuit, and ICF-TetR-LVA circuit as function of  $F_S$  strengths. (J) Maximum sensitivity for antisense transcription based OL circuit, transcriptional Interference based OL circuit, and ICF-TetR-LVA circuit were calculated based on equations S3 ( Flow cytometry data for building this figure is described in Fig. S59-S63).

- 3.6.1 NA-sensing system from *E. coli*. The expression of GFP is controlled by NA-inducible promoter  $P_{recA}$  (Fig. S23A).
- 3.6.2 Antisense transcription based OL circuit. At high AHL concentrations, the transcription of  $P_{recA}$  promoter is inhibited by antisense RNA transcribed from  $P_{lux}$ , which resulted in basal level reduction while keeping the maximum activity of the forward promoter  $P_{recA}$  intact (Fig. S23B).
- 3.6.3 Transcriptional interference based OL circuit. At high AHL concentrations, the transcription of  $P_{recA}$  promoter is inhibited by transcriptional interference from  $P_{lux}$ , which resulted in basal level reduction while keeping the maximum activity of the forward promoter  $P_{recA}$  intact (Fig. S23C).
- 3.6.4 NA-aTc inverting switch. At low aTc concentrations, at low NA concentrations mcherry levels were high whereas at high NA concentrations the mcherry levels were low. The LVA-degradation tag is responsible for reducing TetR-LVA expression levels and for decreasing the ON/OFF ratio of  $P_{tetO}$ . An optimal concentration of anhydrotetracycline( aTc ) was deduced to give the highest ON/OFF ratio to work with in following circuits (explained in 3.6.5). If no significant differences in mCherry levels were observed between the various concentrations of aTc then no aTc was added in the ICF circuit. The mCherry gene was later replaced by LuxR-mCherry operon to be integrated with the transcriptional interference in ICF circuit (Fig. S23D).
- 3.6.5 ICF-TetR-LVA. The NA-inducible promoter  $P_{recA}$  was regulated by adjusting between its minimum expression level (basal level) and its maximum expression level (the ON state). The basal level was controlled through  $P_{lux}$  activity inducible by AHL. Whereas the maximum expression level was controlled by TetR-LVA protein, which represses the expression of LuxR. The transcriptional repressor TetR-LVA was under the control of  $P_{recA}$ . The mCherry gene engineered downstream to LuxR under control of the same promoter  $P_{tetO}$ , acted as an indicator of  $P_{tetO}$  activity and LuxR levels. LuxR levels exhibited high expression at high NA concentration. The reason for this effect could be because the autofluorescence of the cells is enhanced when the bacterial cells are in stress (Surre et al., 2018) (Fig. S23E).

#### 4. Experimental data from Flow cytometry

This section contains flow cytometry data for one representative experiment which was independently repeated for two more times.

##### 4.1 Experimental data for synthetic promoter $P_{BADsyn}$

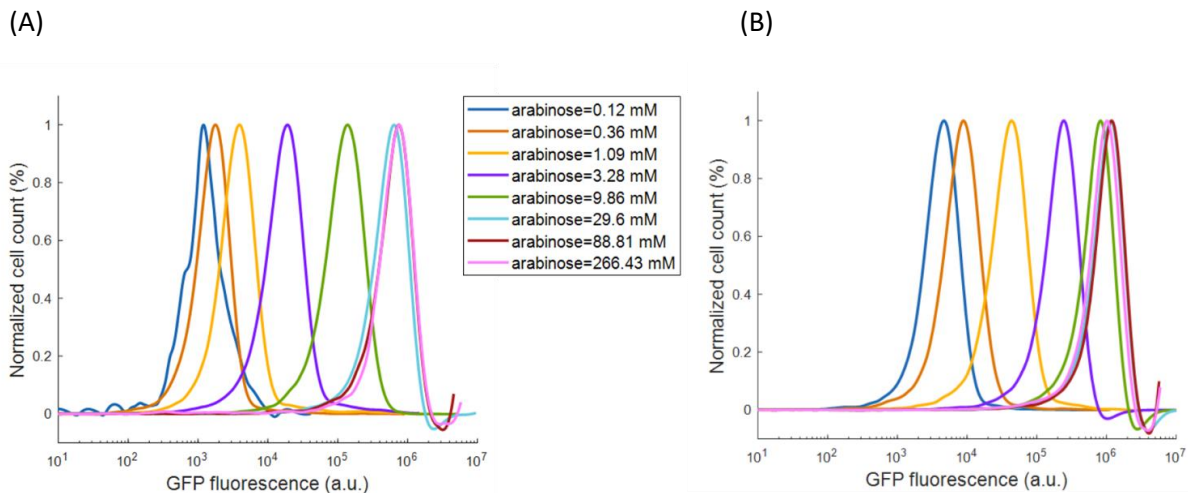
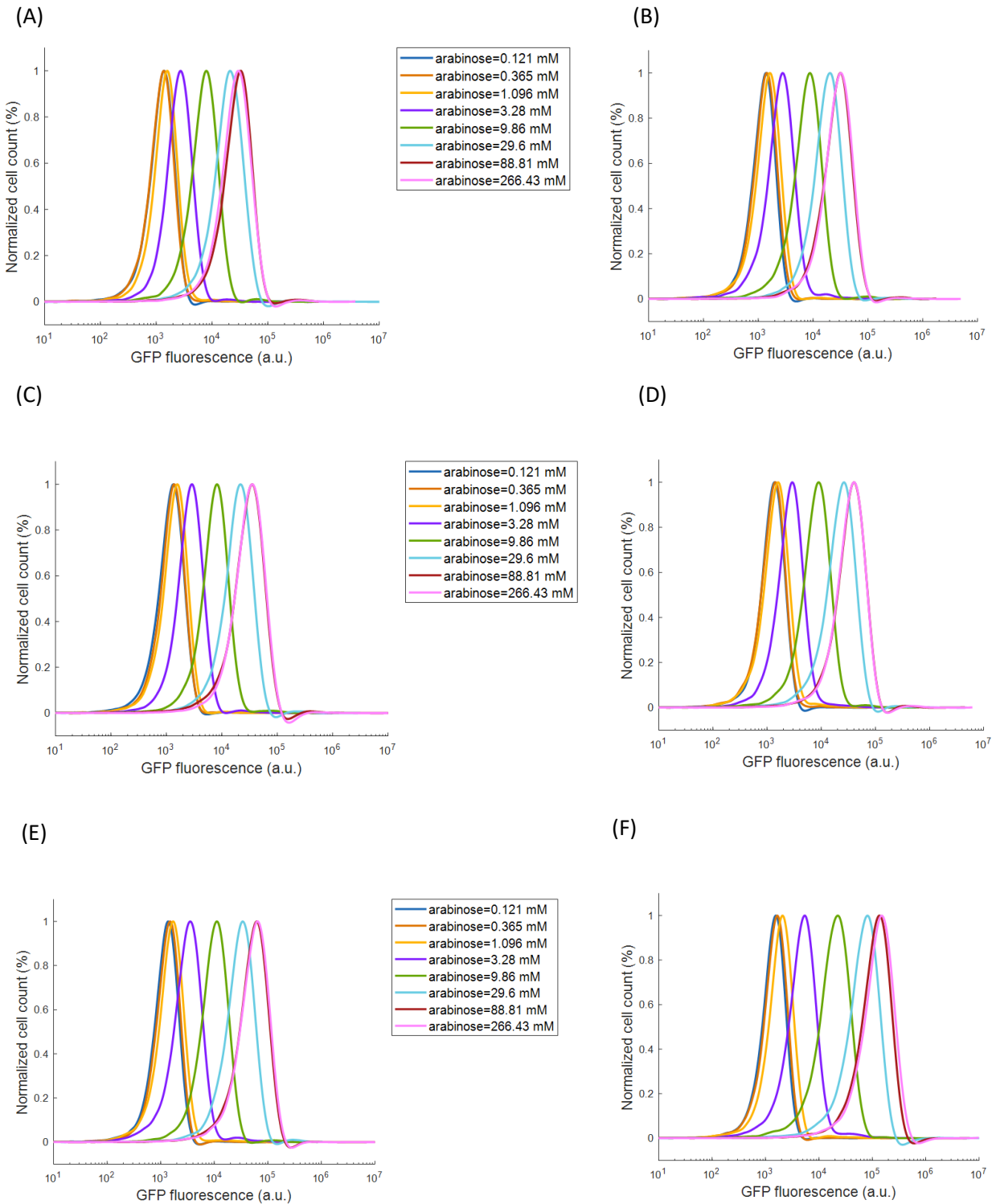
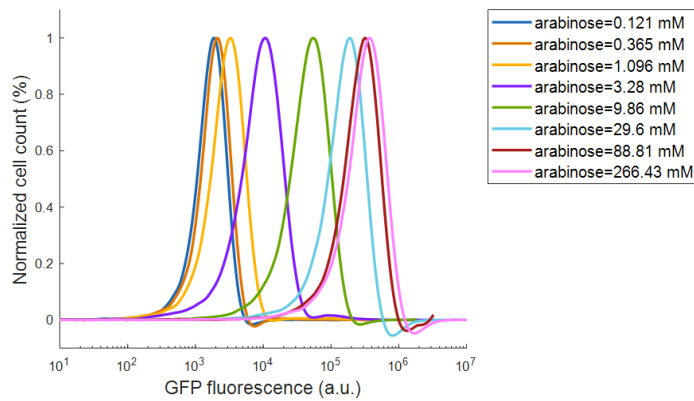


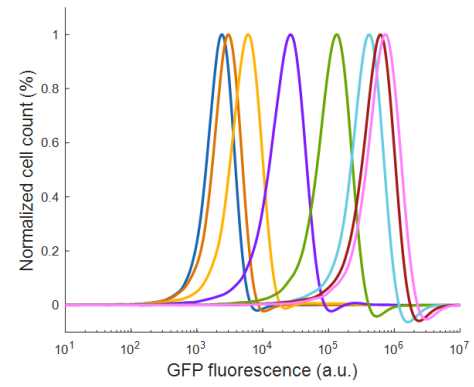
Fig. S24. Flow cytometry data for GFP over bacterial cells population. (A) containing the wild-type topology of  $P_{BAD}$ . (B) containing the wild-type topology of synthetic  $P_{BADsyn}$ . This experimental data was used for generating Fig. 4C.



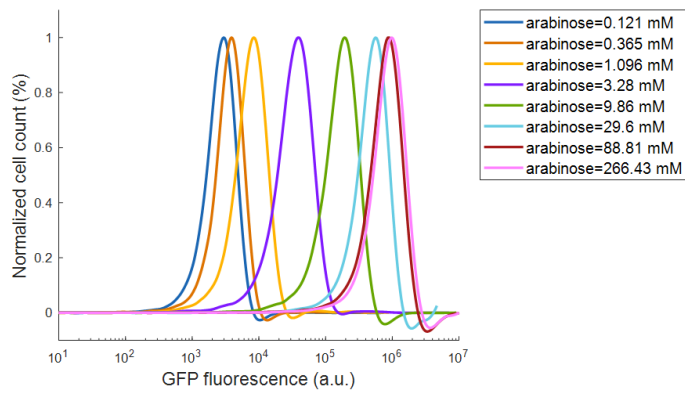
(G)



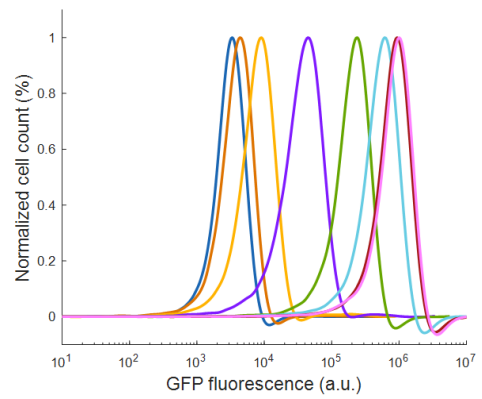
(H)



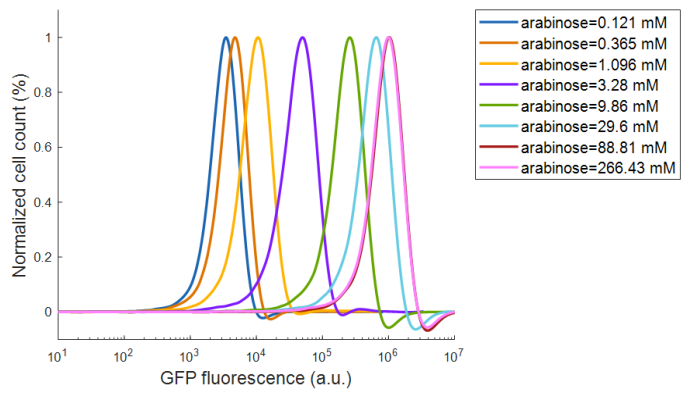
(I)



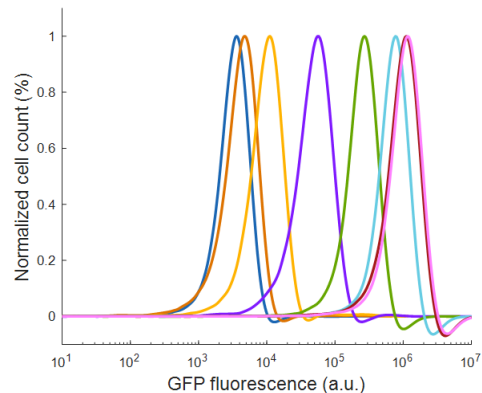
(J)



(K)



(L)



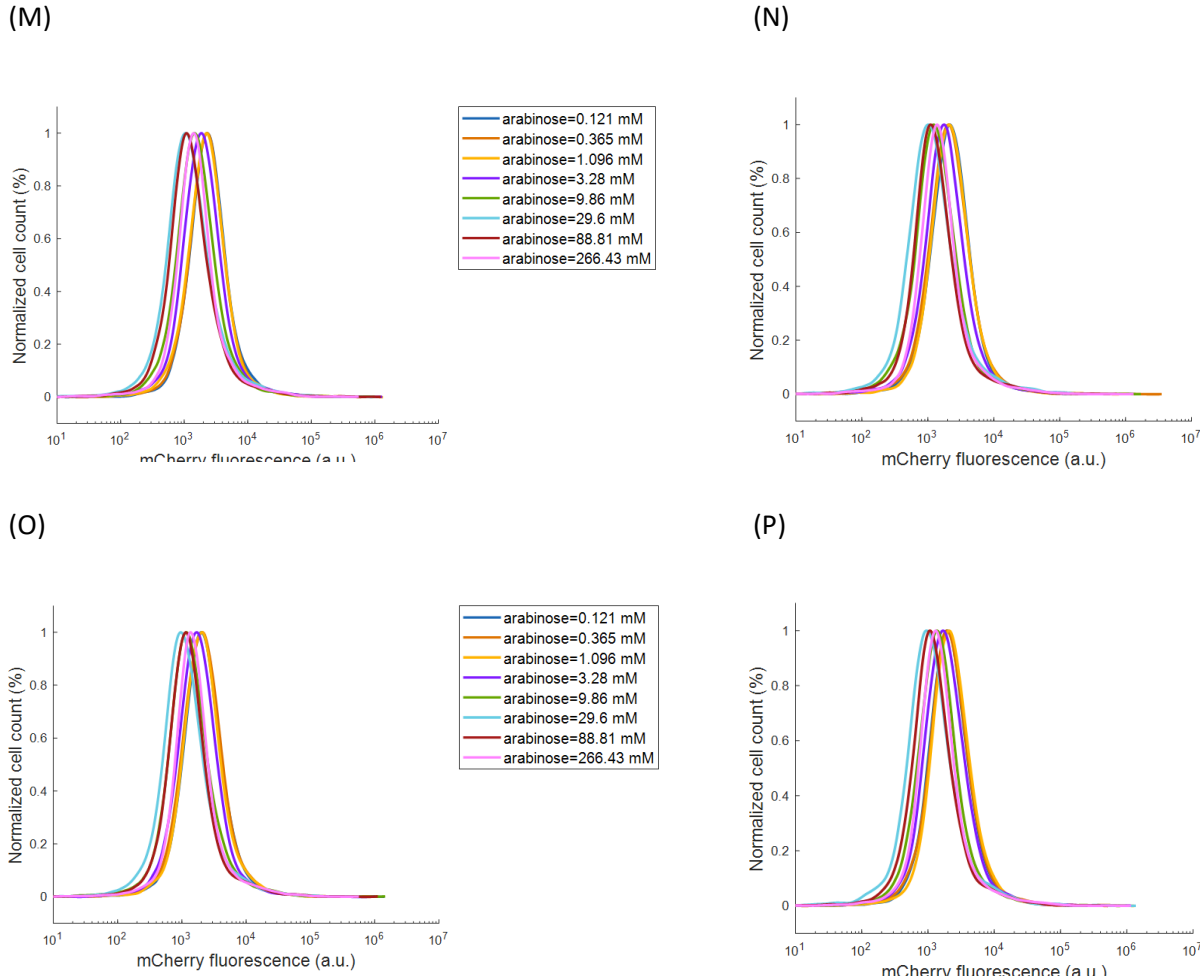
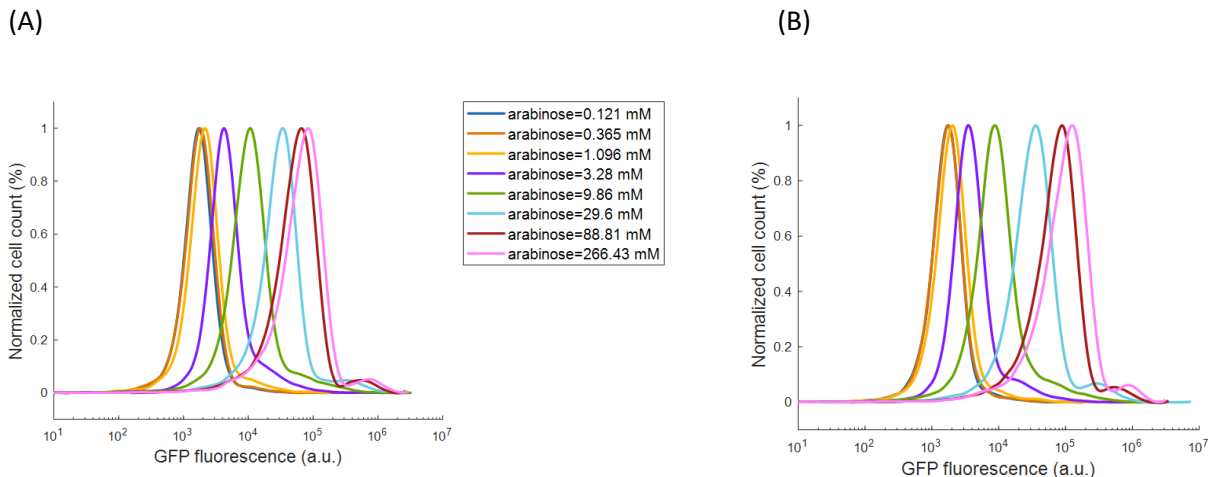
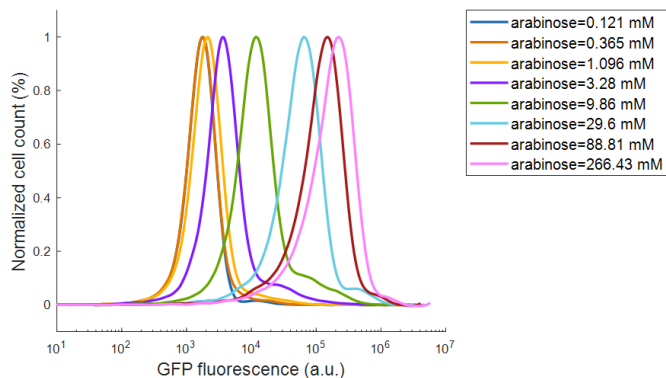


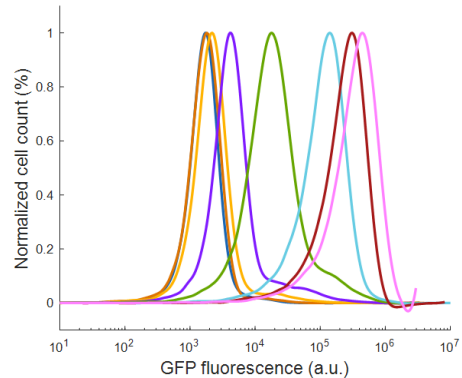
Fig. S25. Flow cytometry data for GFP over bacterial cells population containing OL design of  $P_{BADsyn}$ . (A)  $[AHL]=0.5 \mu M$ , (B)  $[AHL]=0.25 \mu M$ , (C)  $[AHL]=0.125 \mu M$ , (D)  $[AHL]=0.0625 \mu M$ , (E)  $[AHL]=0.0313 \mu M$ , (F)  $[AHL]=0.0156 \mu M$ , (G)  $[AHL]=0.0078 \mu M$ , (H)  $[AHL]=0.0039 \mu M$ , (I)  $[AHL]=0.002 \mu M$ , (J)  $[AHL]=0.001 \mu M$ , (K)  $[AHL]=0.0005 \mu M$ , (L)  $[AHL]=0.0002 \mu M$ . (M-P) Flow cytometry data for mCherry over bacterial cells population containing OL design. (M)  $[AHL]=0.0078 \mu M$ , (N)  $[AHL]=0.0039 \mu M$ , (O)  $[AHL]=0.00098 \mu M$ , (P)  $[AHL]=0.0005 \mu M$ . This experimental data was used for generating Fig. 6A and Fig.S17A.



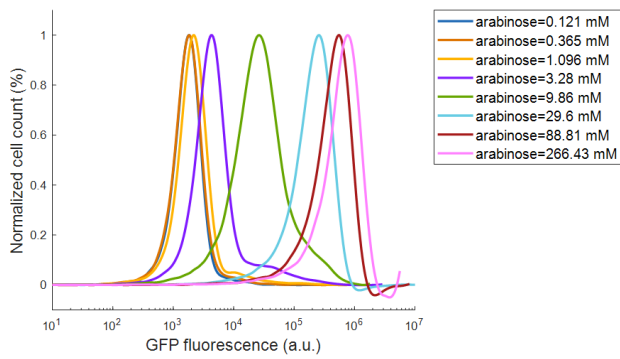
(C)



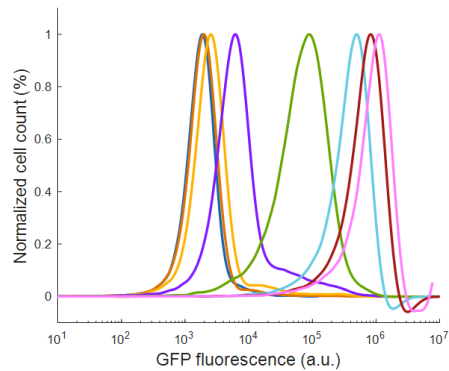
(D)



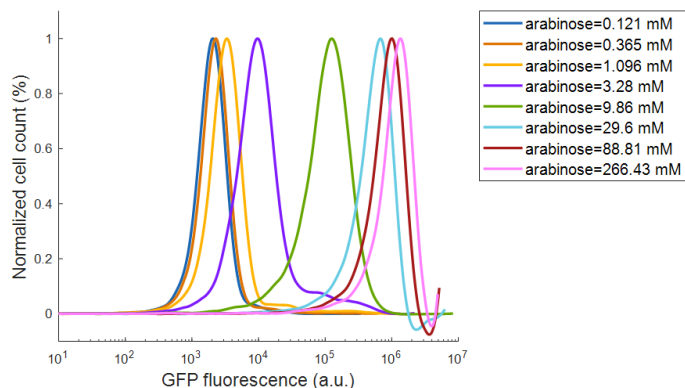
(E)



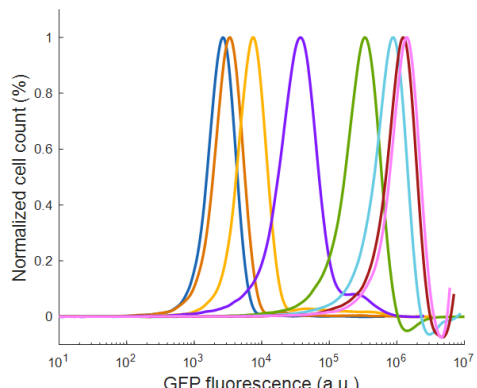
(F)



(G)



(H)



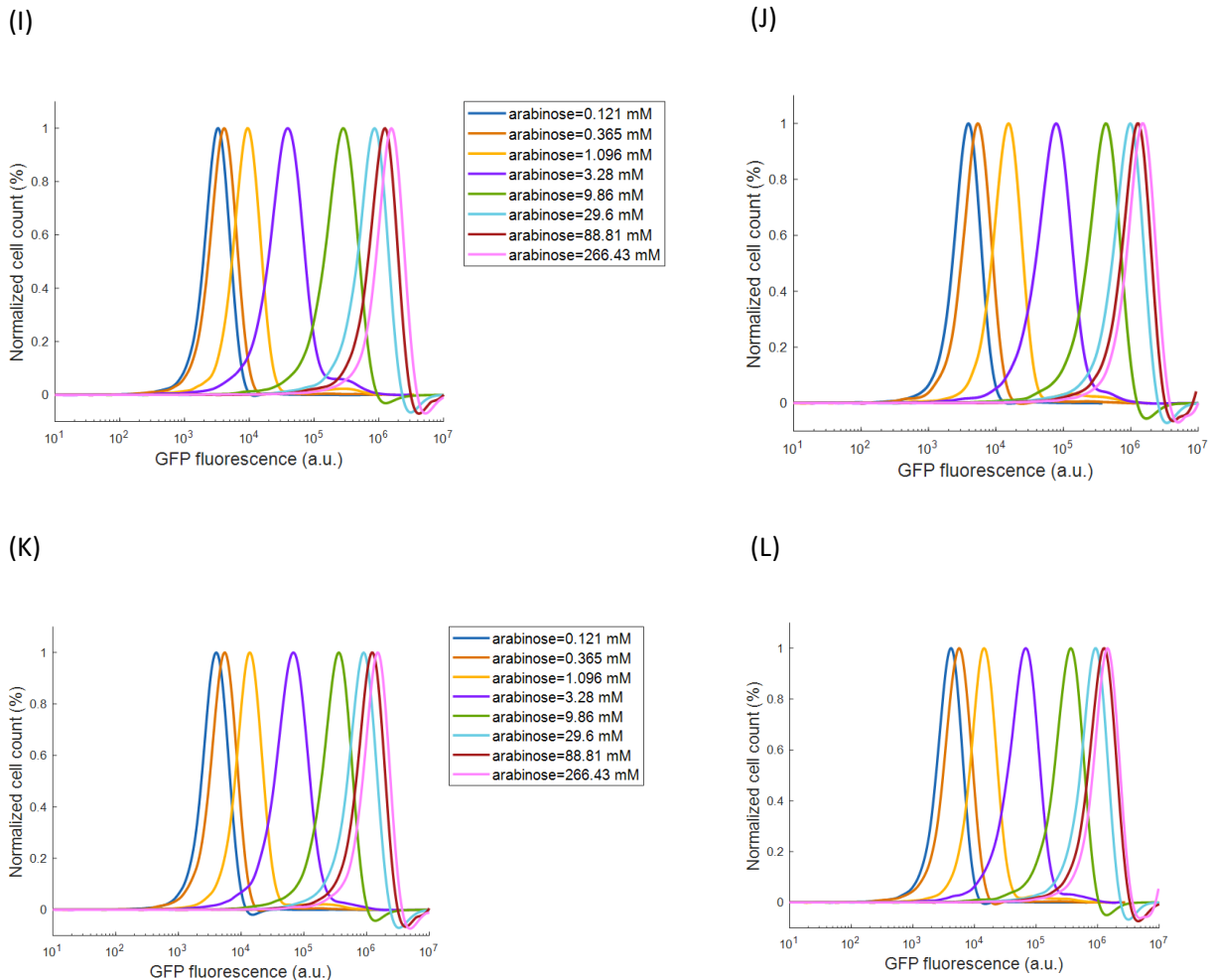
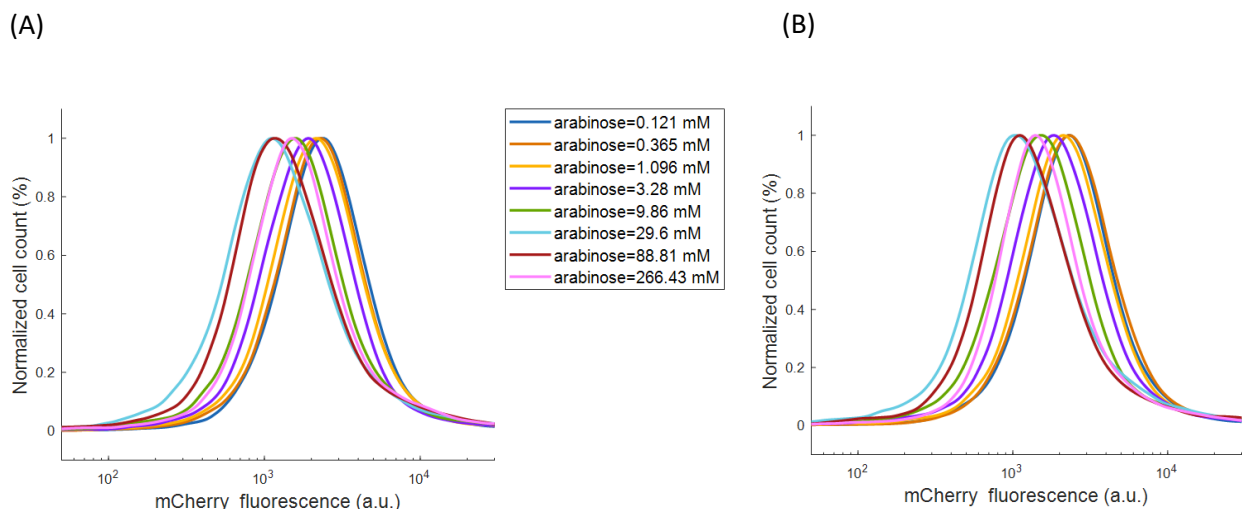


Fig. S26. Flow cytometry data for GFP over bacterial cells population containing ICF-TetR-LVA design of  $P_{BADsyn}$ . (A)  $[AHL]=0.5 \mu\text{M}$ , (B)  $[AHL]=0.25 \mu\text{M}$ , (C)  $[AHL]=0.125 \mu\text{M}$ , (D)  $[AHL]=0.625 \mu\text{M}$ , (E)  $[AHL]=0.0313 \mu\text{M}$ , (F)  $[AHL]=0.0156 \mu\text{M}$ , (G)  $[AHL]=0.0078 \mu\text{M}$ , (H)  $[AHL]=0.0039 \mu\text{M}$ , (I)  $[AHL]=0.002 \mu\text{M}$ , (J)  $[AHL]=0.001 \mu\text{M}$ , (K)  $[AHL]=0.0005 \mu\text{M}$ , (L)  $[AHL]=0.0002 \mu\text{M}$ . This experimental data was used for generating Fig. 6B and Fig.S17D.



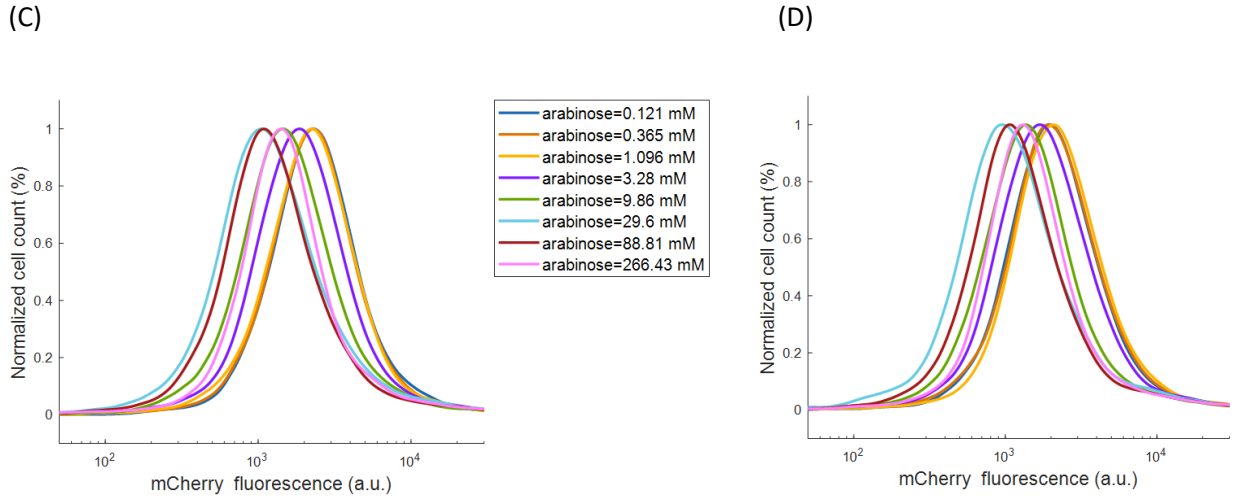
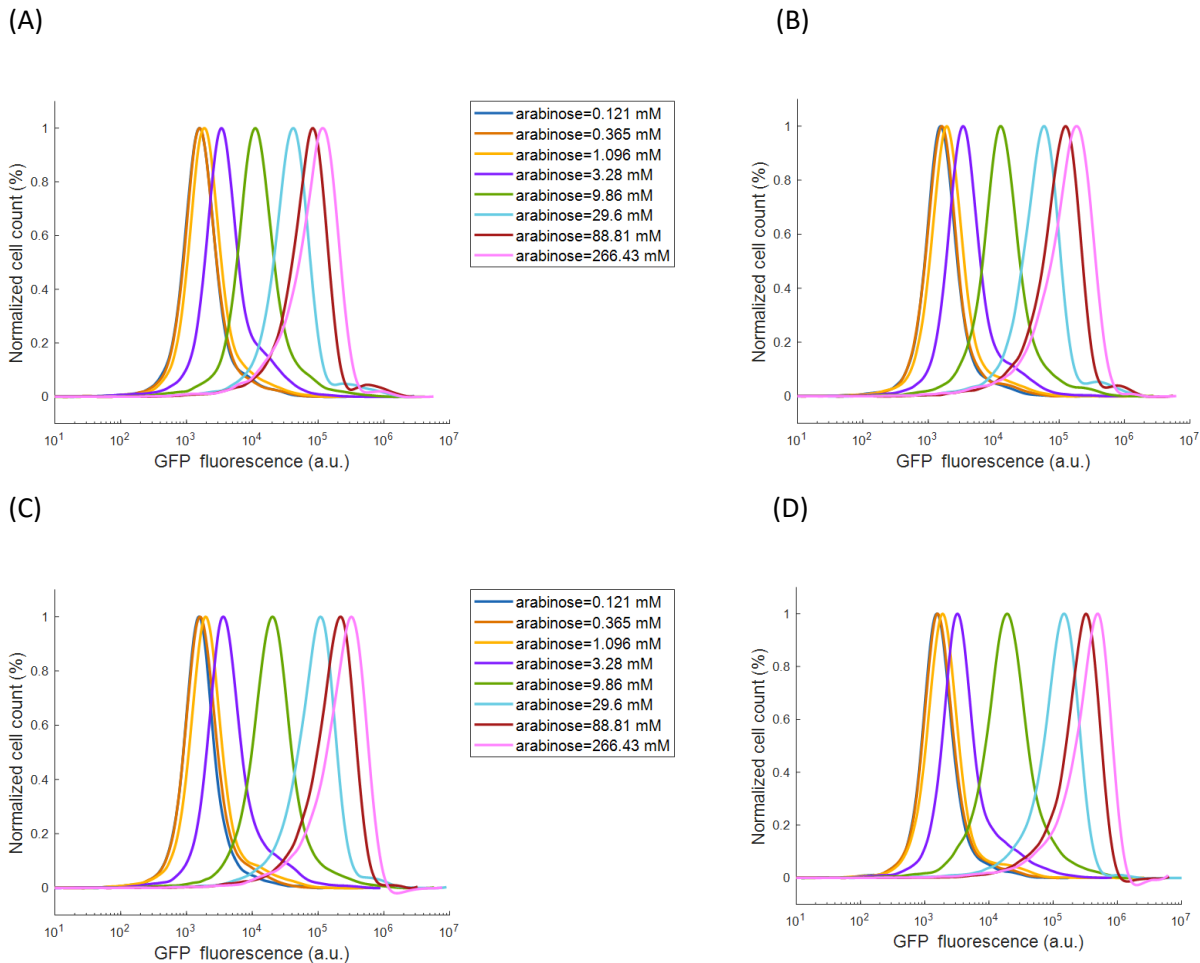
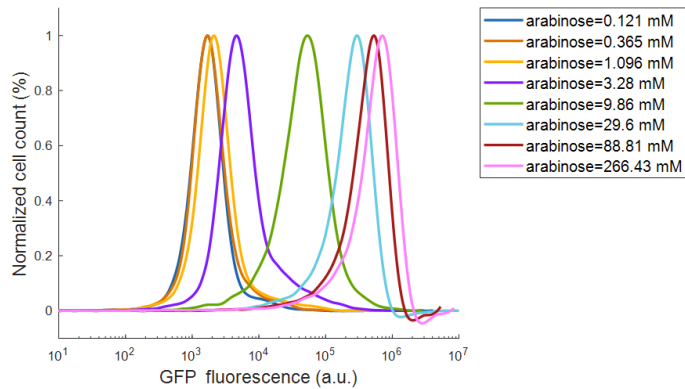


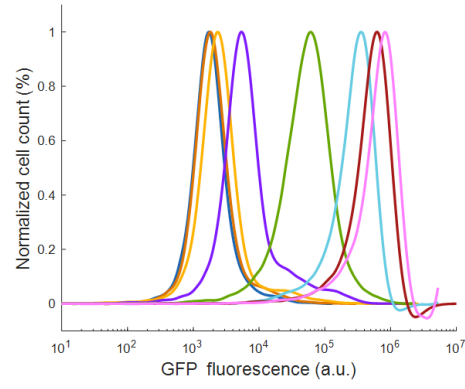
Fig. S27. Flow cytometry data for mCherry over bacterial cells population containing ICF-TetR-LVA design of  $P_{BADsyn}$ . (A)  $[AHL]=0.0313 \mu\text{M}$ , (B)  $[AHL]=0.0156 \mu\text{M}$ , (C)  $[AHL]=0.0078 \mu\text{M}$ , (D)  $[AHL]=0.0005 \mu\text{M}$ . This experimental data was used for generating Fig. 6B and Fig.S17D.



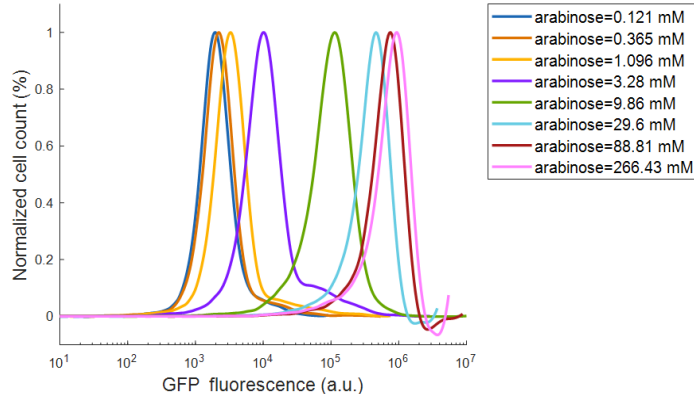
(E)



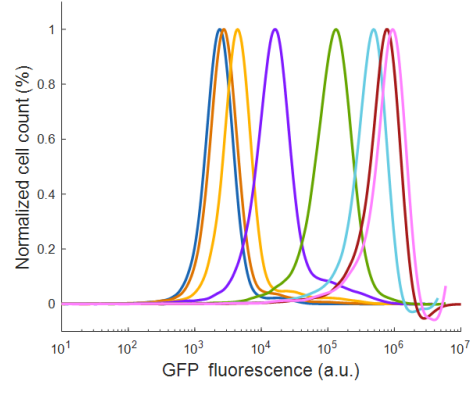
(F)



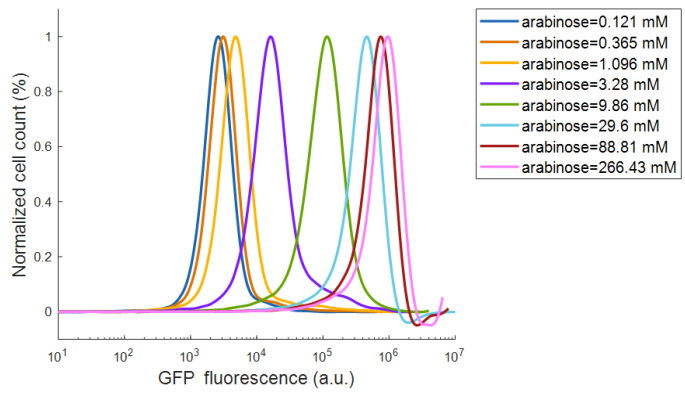
(G)



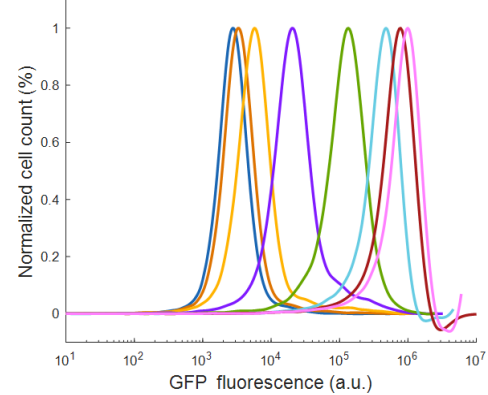
(H)



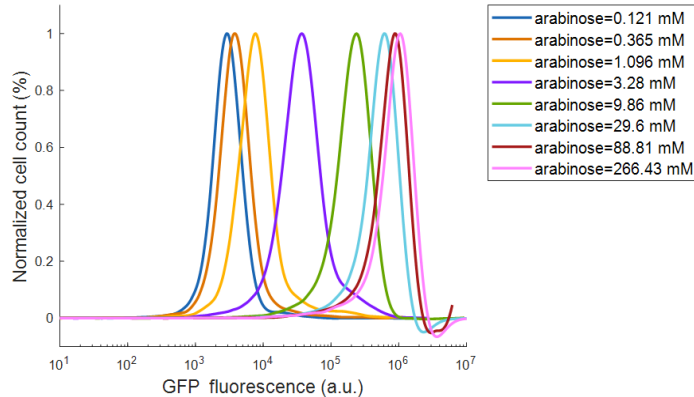
(I)



(J)



(K)



(L)

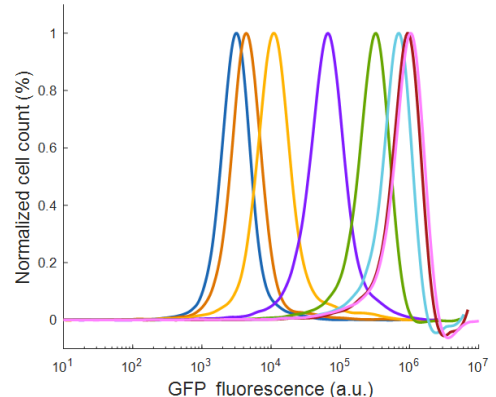
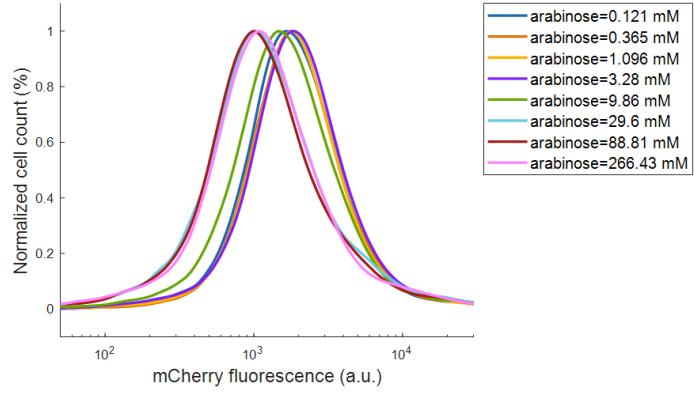
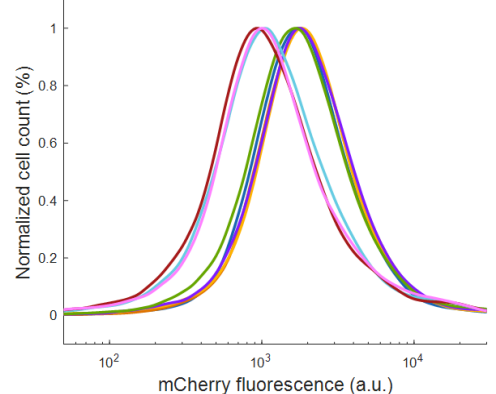


Fig. S28. Flow cytometry data for GFP over bacterial cells population containing ICF-TetR design of P<sub>BADsyn</sub>. (A) [AHL]=0.5  $\mu$ M, (B)[AHL]=0.25  $\mu$ M, (C)[AHL]=0.125  $\mu$ M, (D)[AHL]=0.625  $\mu$ M, (E)[AHL]=0.0313  $\mu$ M, (F)[AHL]=0.0156  $\mu$ M, (G)[AHL]=0.0078  $\mu$ M, (H)[AHL]=0.0039  $\mu$ M, (I)[AHL]=0.002  $\mu$ M, (J)[AHL]=0.001  $\mu$ M, (K)[AHL]=0.0005  $\mu$ M, (L)[AHL]=0.0002  $\mu$ M. In all ICF-TetR experiments [aTc]=11.11ng/ml. This experimental data was used for generating Fig.S17E.

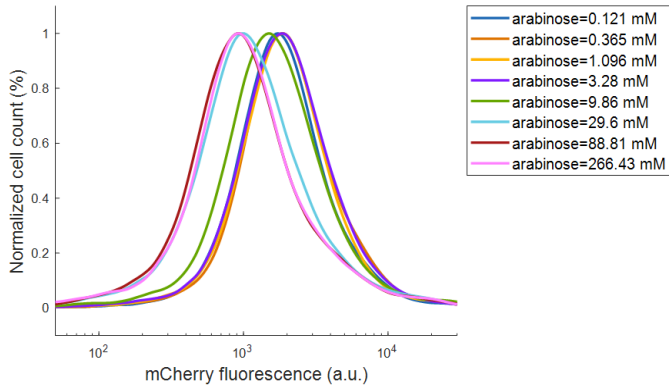
(A)



(B)



(C)



(D)

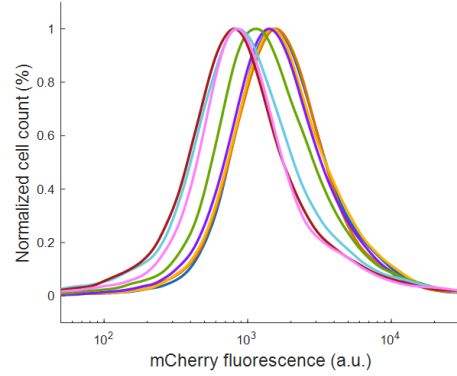
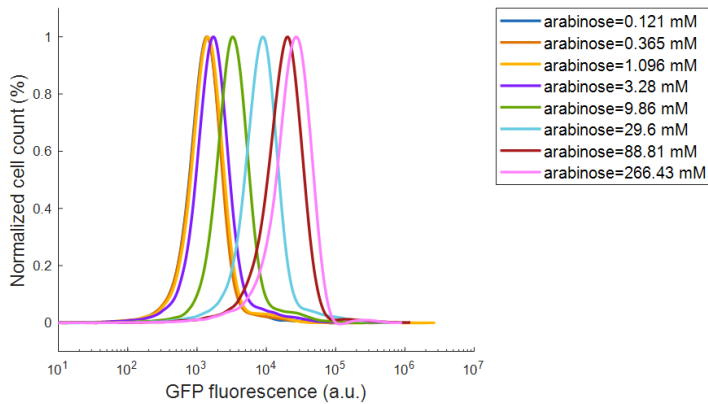
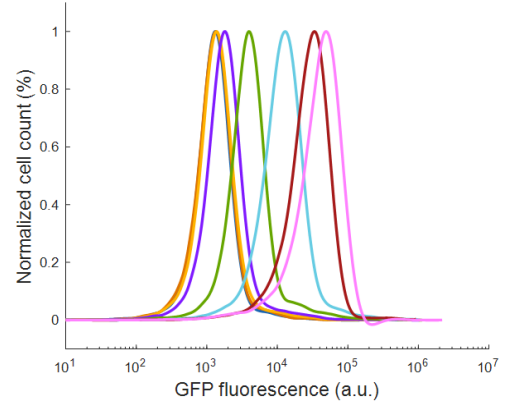


Fig. S29. Flow cytometry data for mCherry over bacterial cells population containing ICF-TetR design of P<sub>BADsyn</sub>. (A) [AHL]=0.5  $\mu$ M, (B) [AHL]=0.0625  $\mu$ M, (C) [AHL]=0.0313  $\mu$ M, (D) [AHL]=0.0002  $\mu$ M. In all ICF-TetR experiments [aTc]=11.11ngr/ml. This experimental data was used for generating Fig.S17E.

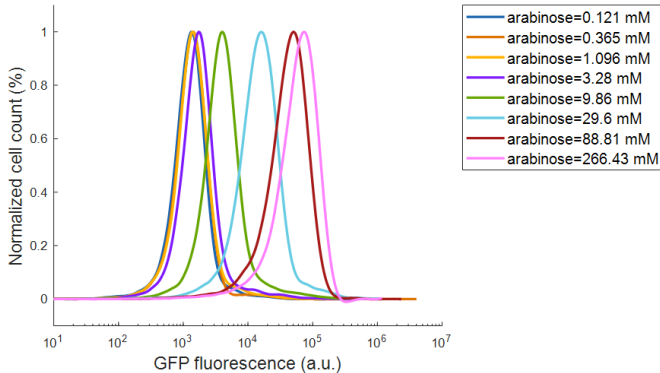
(A)



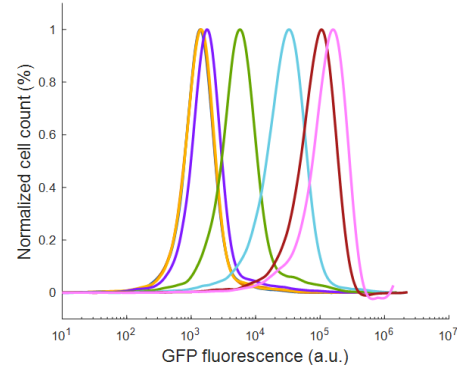
(B)



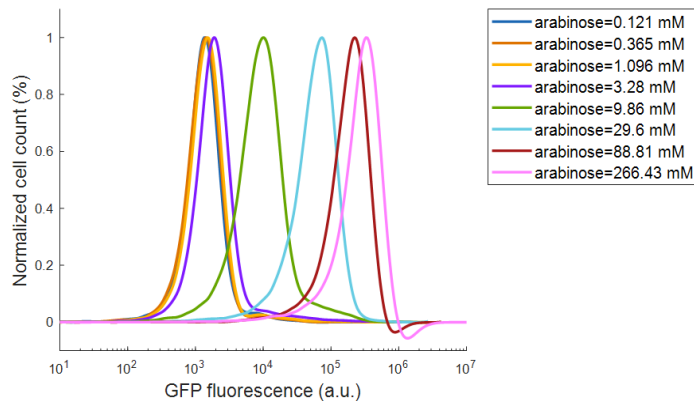
(C)



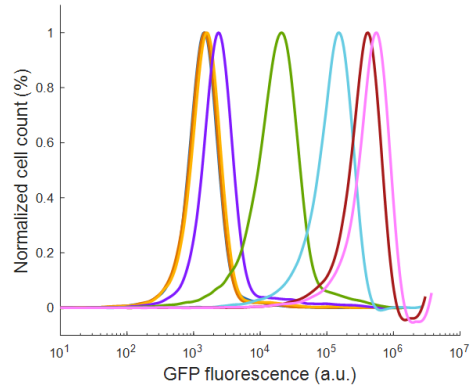
(D)



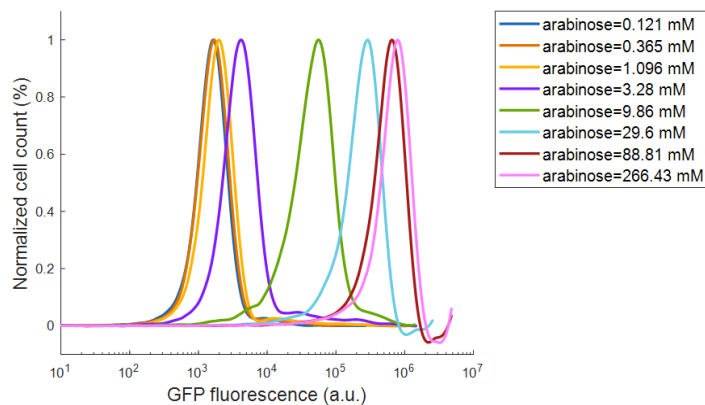
(E)



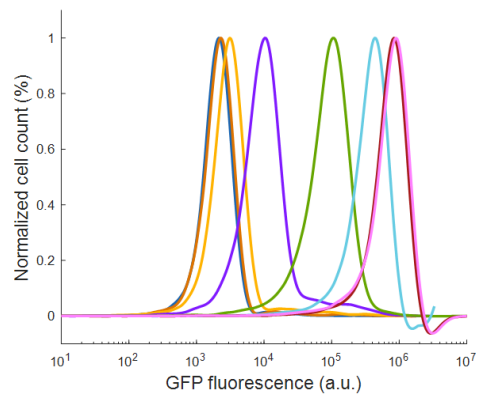
(F)



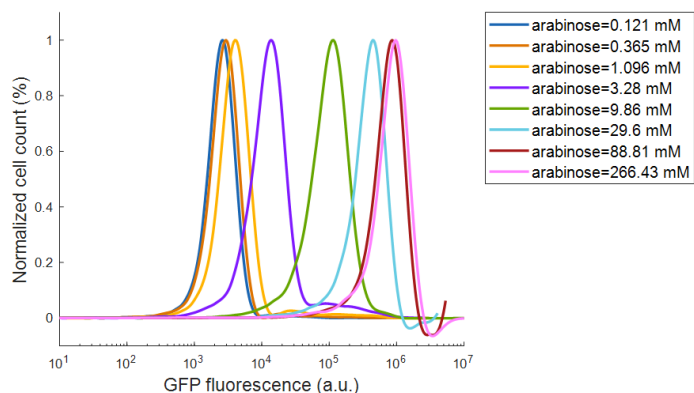
(G)



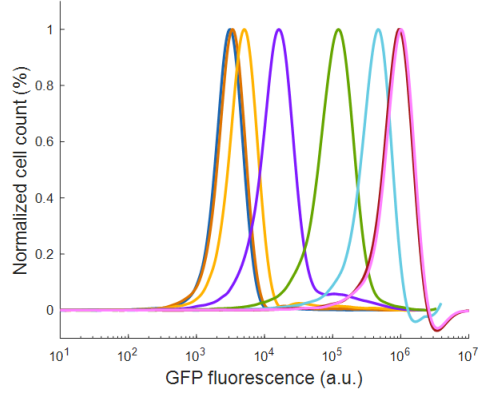
(H)



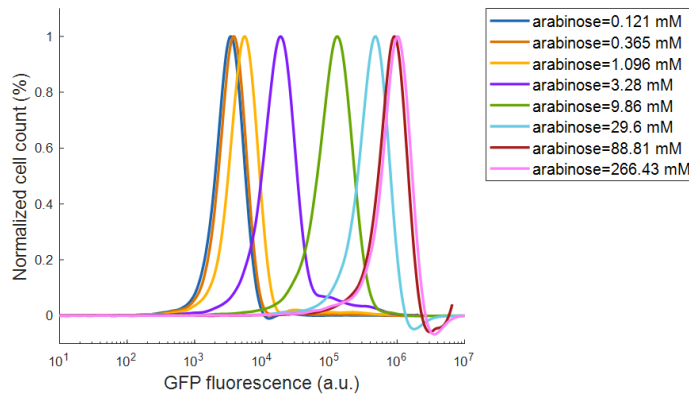
(I)



(J)



(K)



(L)

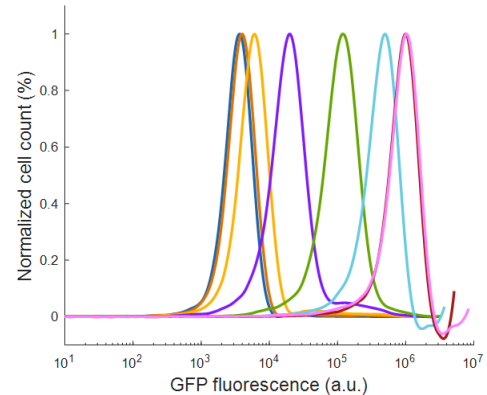
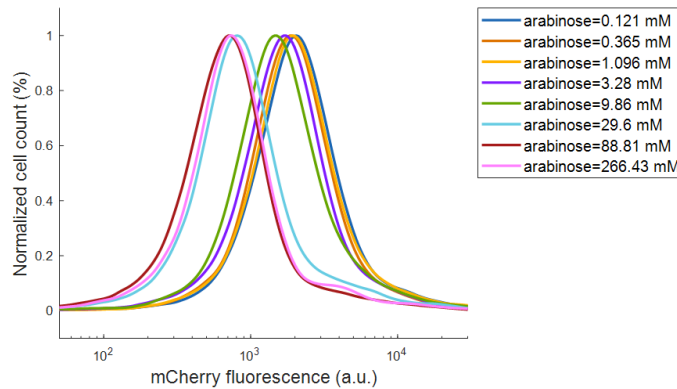
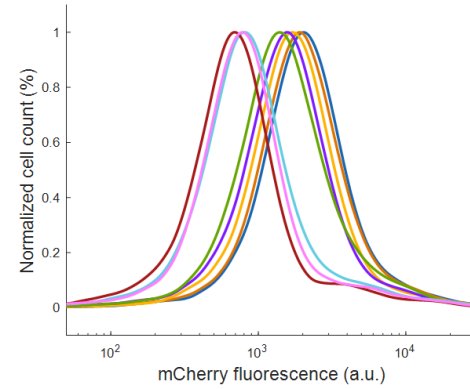


Fig. S30. Flow cytometry data for GFP over bacterial cells population containing DNF-TetR design of  $P_{BADsyn}$ . (A) [AHL]=0.5  $\mu$ M, (B)[AHL]=0.25  $\mu$ M, (C)[AHL]=0.125  $\mu$ M, (D)[AHL]=0.625  $\mu$ M, (E)[AHL]=0.0313  $\mu$ M, (F)[AHL]=0.0156  $\mu$ M, (G)[AHL]=0.0078  $\mu$ M, (H)[AHL]=0.0039  $\mu$ M, (I)[AHL]=0.002  $\mu$ M, (J)[AHL]=0.001  $\mu$ M, (K)[AHL]=0.0005  $\mu$ M, (L)[AHL]=0.0002  $\mu$ M. In all ICF-TetR experiments [aTc]=11.11ng/ml. This experimental data was used for generating Fig.S17F.

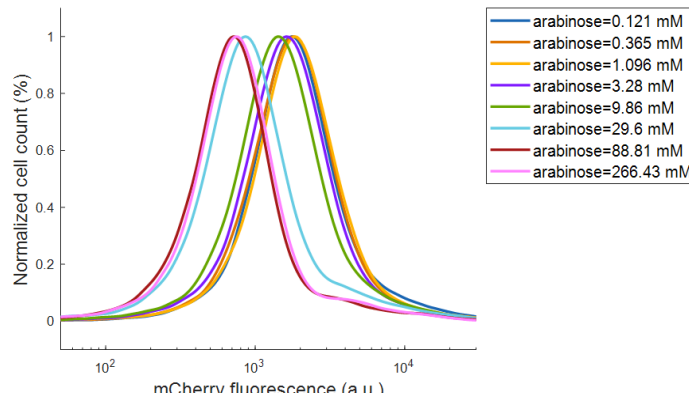
(A)



(B)



(C)



(D)

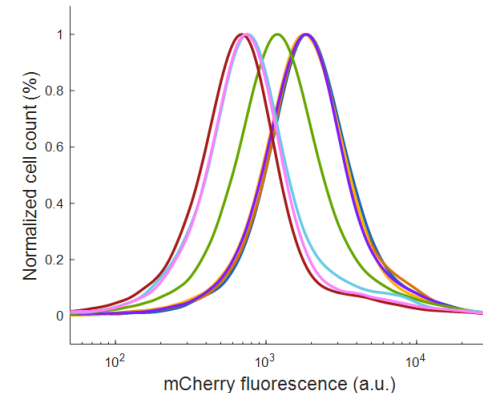
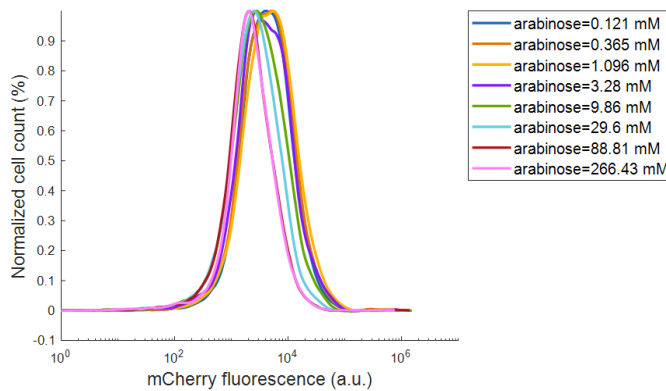
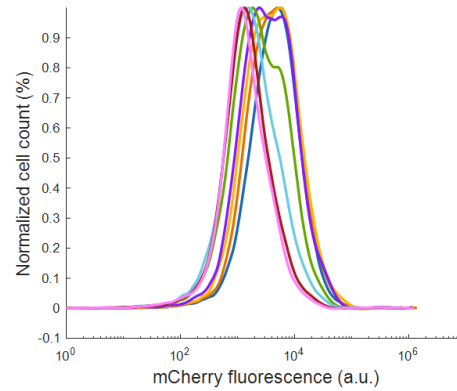


Fig. S31. Flow cytometry data for mCherry over bacterial cells population containing DNF-TetR design of  $P_{BADsyn}$ . (A)  $[AHL]=0.5 \mu\text{M}$ , (B)  $[AHL]=0.0625 \mu\text{M}$ , (C)  $[AHL]=0.0313 \mu\text{M}$ , (D)  $[AHL]=0.0078 \mu\text{M}$ . In all DNF-TetR experiments  $[aTc]=11.11\text{ngr/ml}$ . This experimental data was used for generating Fig.S17F.

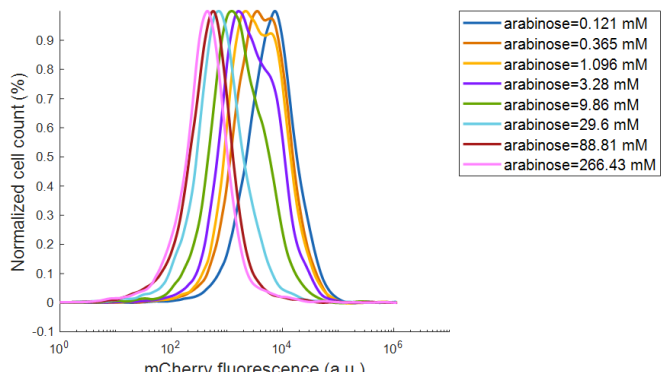
(A)



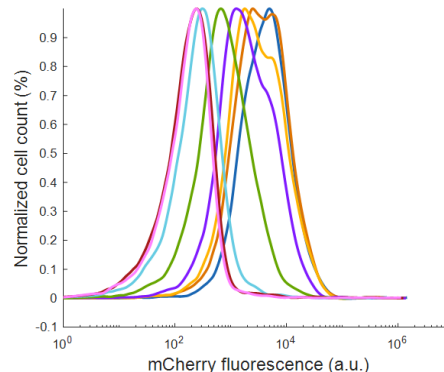
(B)



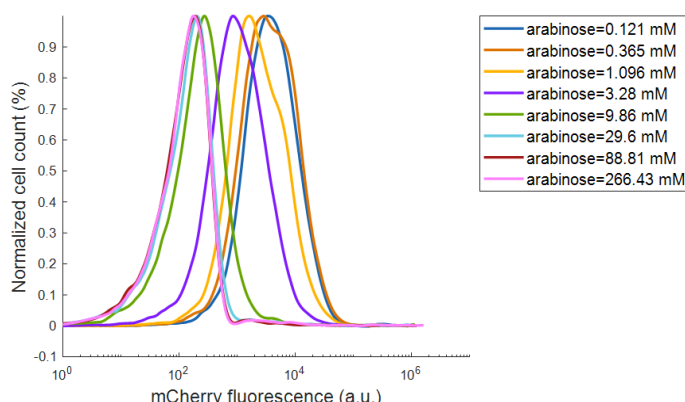
(C)



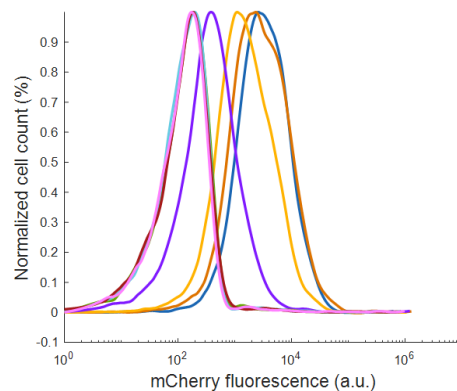
(D)



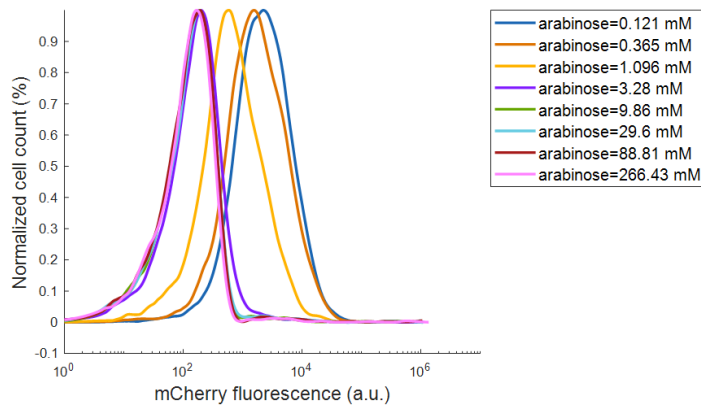
(E)



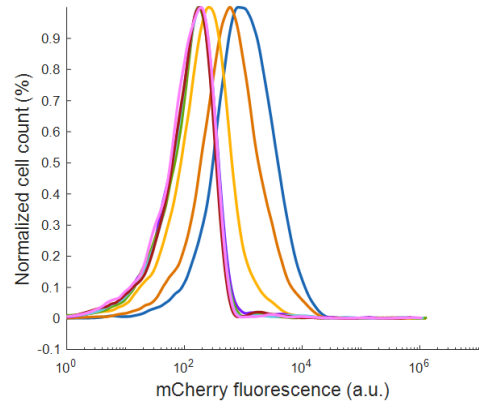
(F)



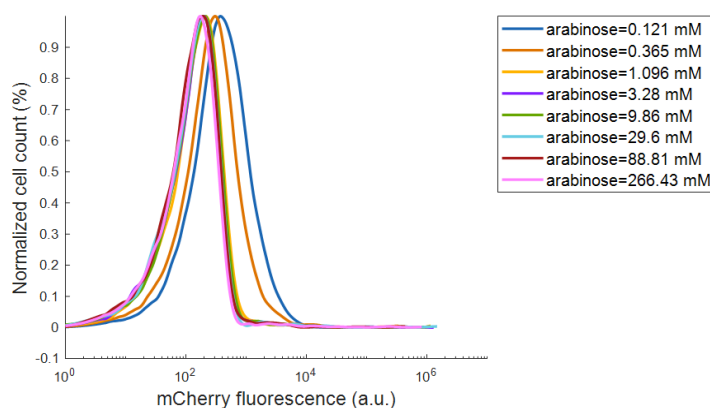
(G)



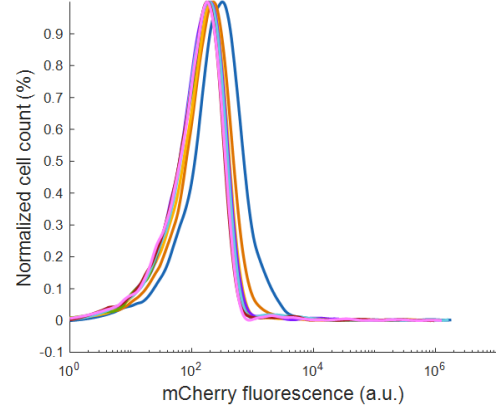
(H)



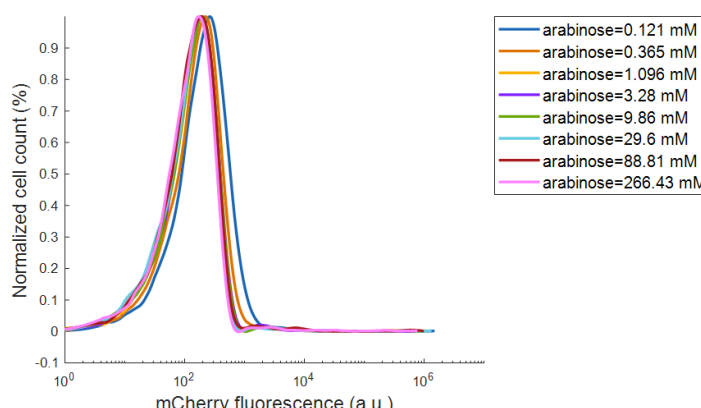
(I)



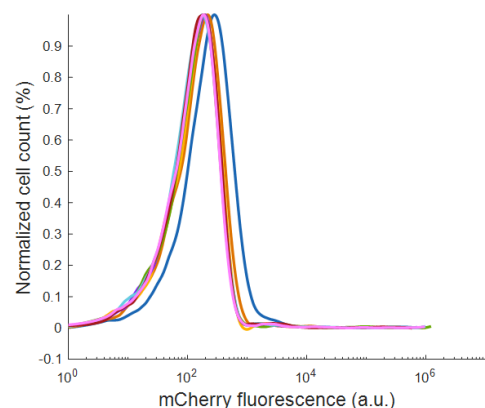
(J)



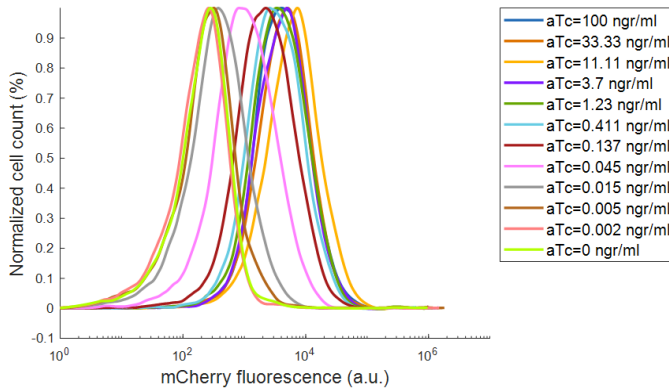
(K)



(L)



(O)



(P)

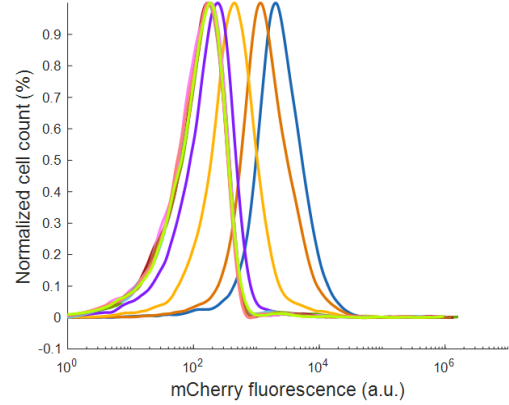
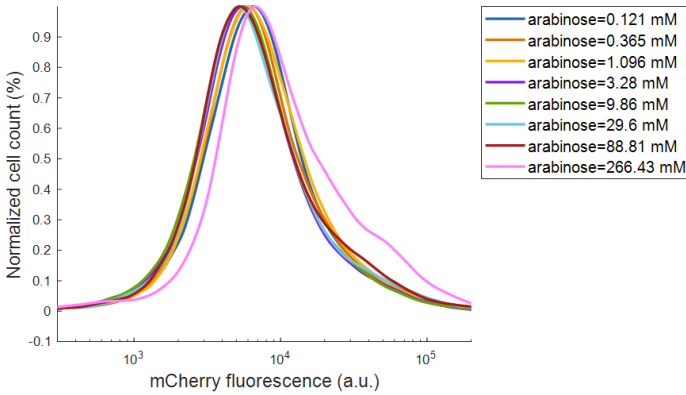
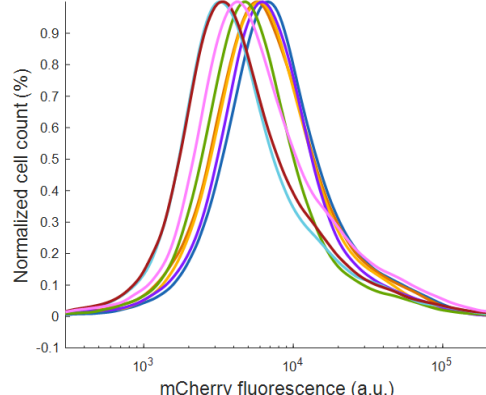


Fig. S32. Flow cytometry data for mCherry over bacterial cells population containing arabinose-aTc inverting switch (TetR) design of P<sub>BADsyn</sub>. (A) [aTc]=100ngr/ml, (B) [aTc]=33.33ngr/ml, (C) [aTc]=11.11ngr/ml, (D) [aTc]=3.7ngr/ml, (E) [aTc]=1.23ngr/ml, (F) [aTc]=0.411ngr/ml, (G) [aTc]=0.137ngr/ml, (H) [aTc]=0.045ngr/ml, (I) [aTc]=0.015ngr/ml, (J) [aTc]=0.005ngr/ml, (K) [aTc]=0.002ngr/ml, (L) [aTc]=0ngr/ml. (O)[arabinose]=0.121mM, (P) [arabinose]=266.43mM. This experimental data was used for generating Fig.S17C.

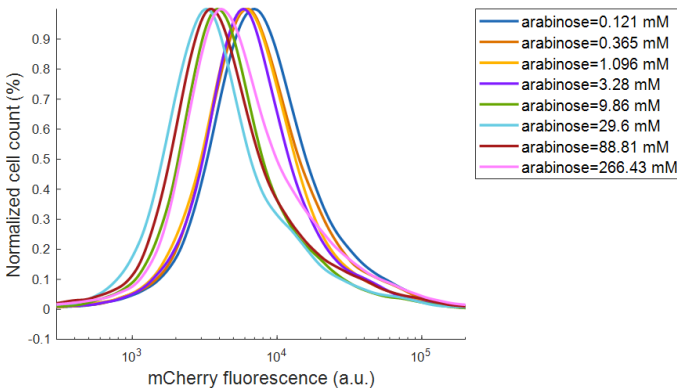
(A)



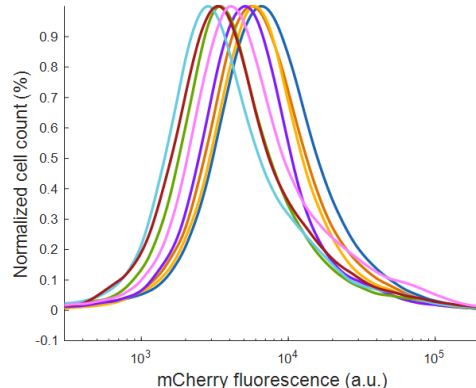
(B)



(C)



(D)



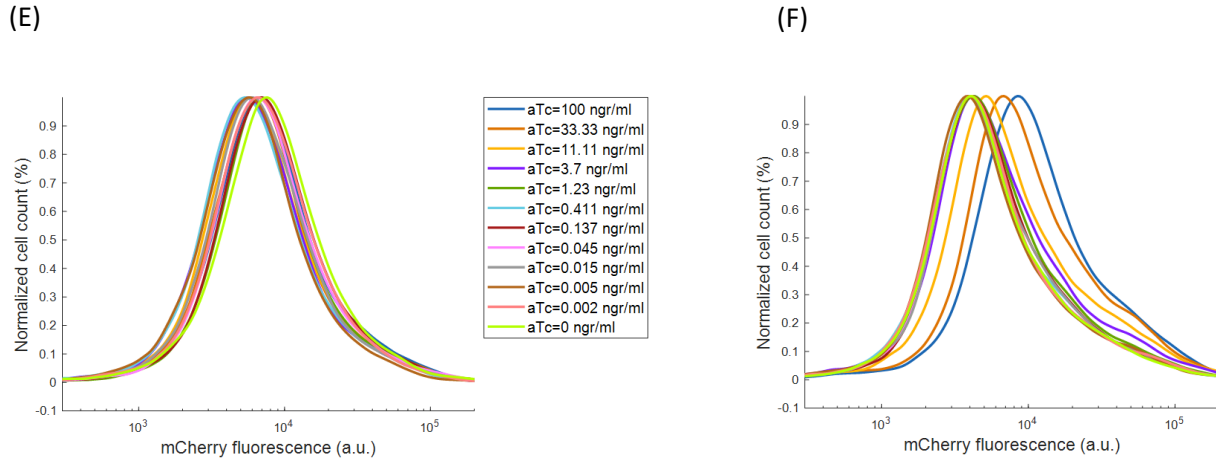
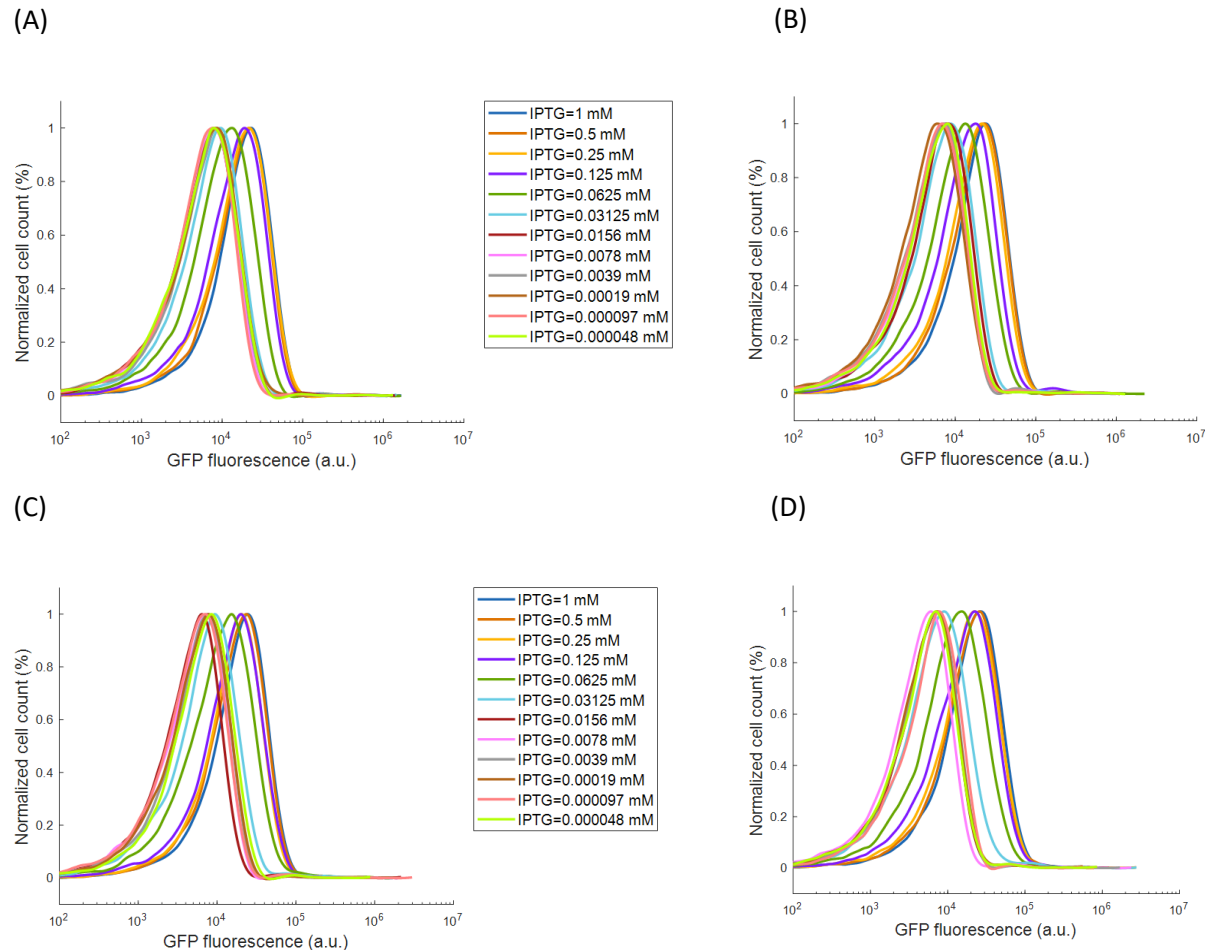


Fig. S33. Flow cytometry data for mCherry over bacterial cells population containing arabinose-aTc inverting switch (TetR-LVA) design of  $P_{BADsyn}$ . (A)[aTc]=33.33ngr/ml, (B)[aTc]=1.23ngr/ml, (C)[aTc]=0.137ngr/ml, (D) [aTc]=0.02ngr/ml, (E) [arabinose]=0.121mM, (F) [arabinose]=266.43mM. This experimental data was used for generating Fig.S17B.

#### 4.2 Experimental data for synthetic promoter $P_{lacO}$



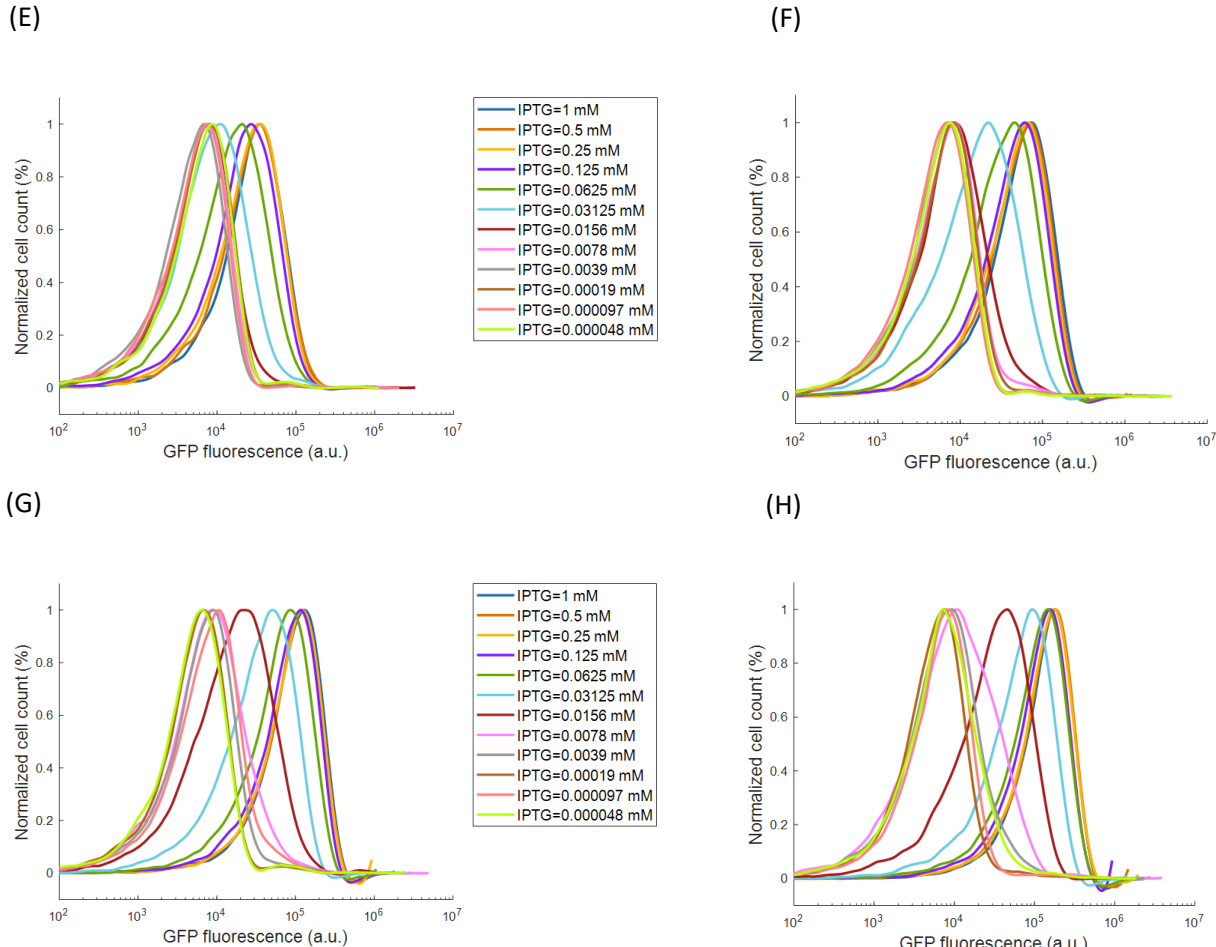
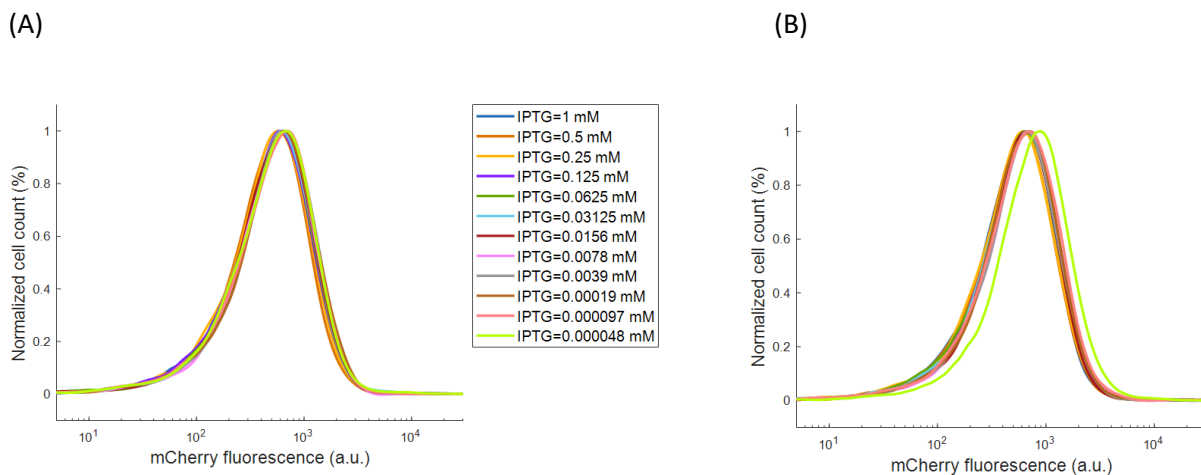


Fig. S34. Flow cytometry data for GFP over bacterial cells population containing OL design of  $P_{lacO}$ . (A) [AHL]=6.66  $\mu$ M, (B) [AHL]=2.22  $\mu$ M, (C) [AHL]=0.74  $\mu$ M, (D) [AHL]=0.24  $\mu$ M, (E) [AHL]=0.08  $\mu$ M, (F) [AHL]=0.03  $\mu$ M (G) [AHL]=0.009  $\mu$ M, (H) [AHL]=0.00  $\mu$ M. This experimental data was used for generating Fig.S19A.



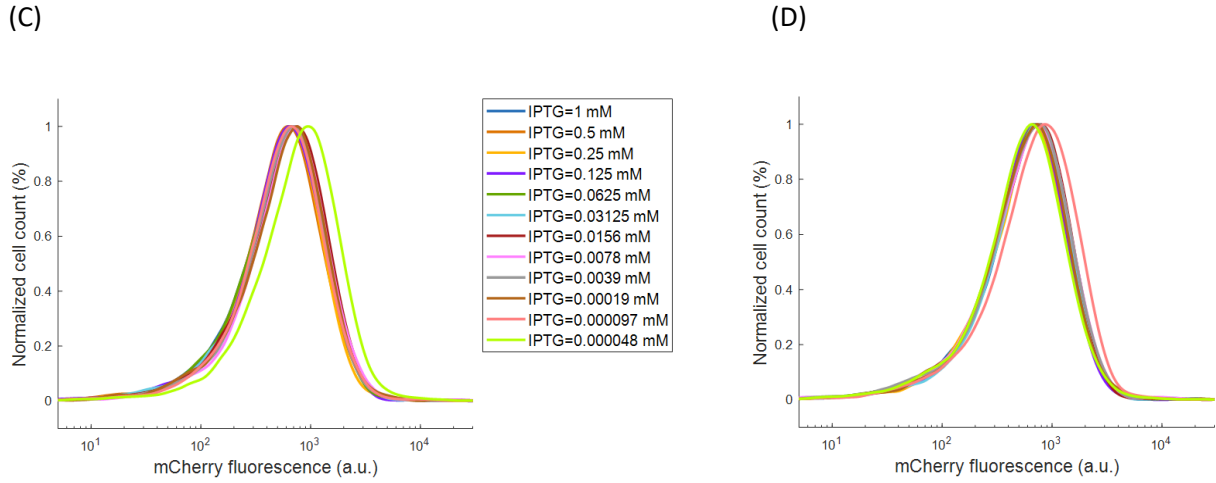
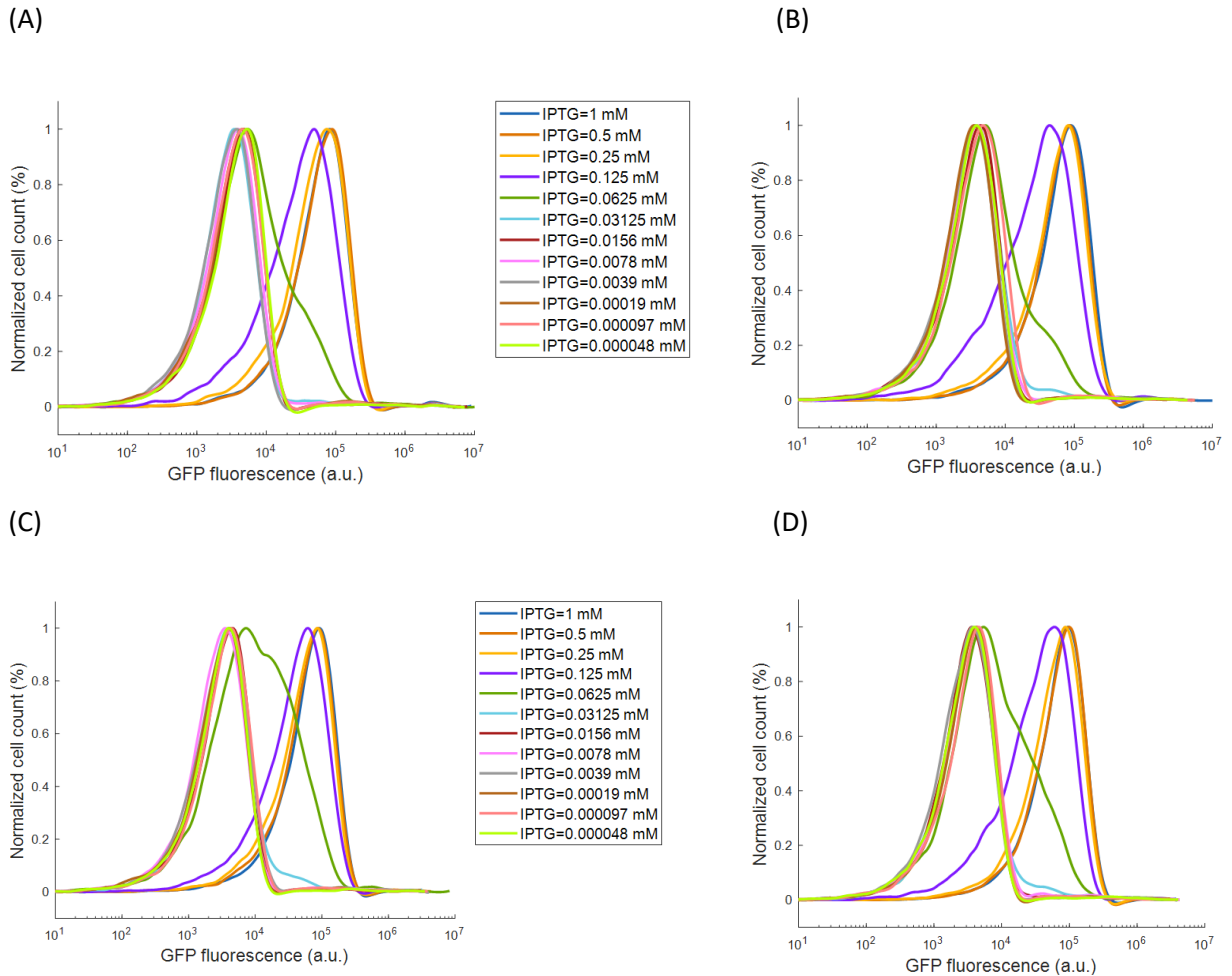


Fig. S35. Flow cytometry data for mCherry over bacterial cells population containing OL design of  $P_{lacO}$ . (A)  $[AHL]=6.66 \mu M$ , (B)  $[AHL]=0.74 \mu M$ , (C)  $[AHL]=0.08 \mu M$ , (D)  $[AHL]=0.00 \mu M$ . This experimental data was used for generating Fig.S19A.



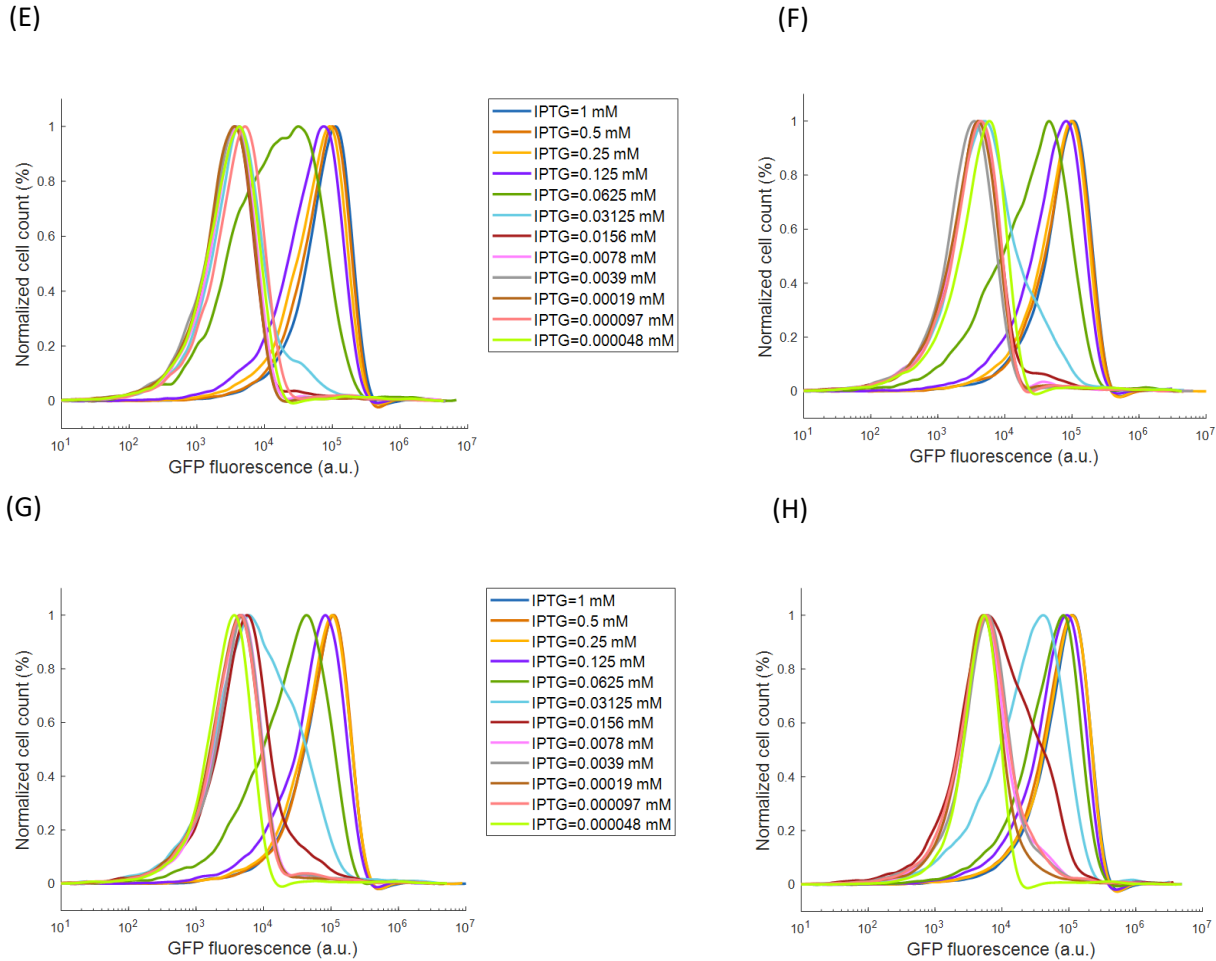
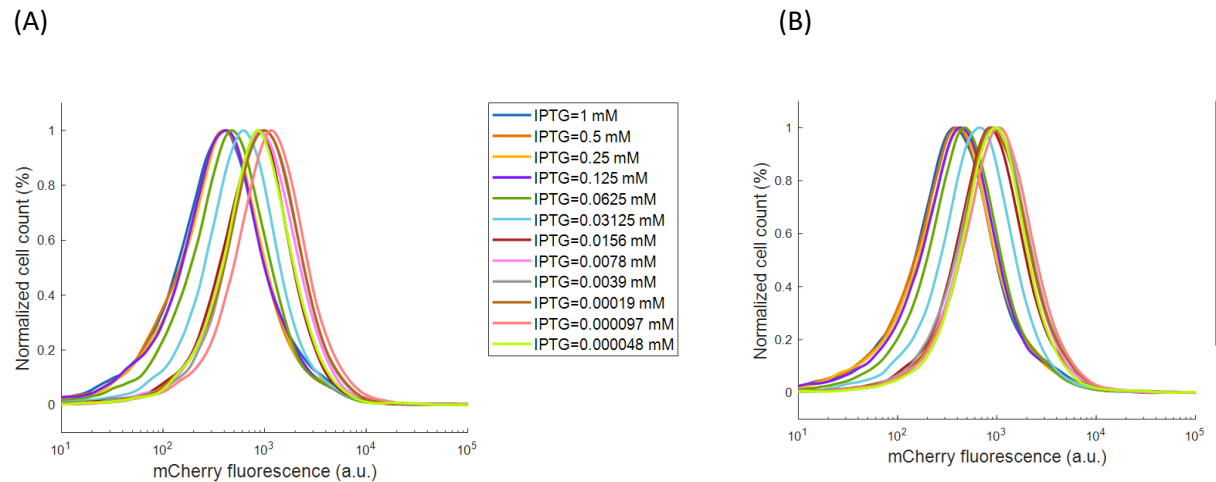


Fig. S36. Flow cytometry data for GFP over bacterial cells population containing ICF-TetR-LVA design of  $P_{lacO}$ . (A)  $[AHL]=6.66 \mu\text{M}$ , (B)  $[AHL]=2.22 \mu\text{M}$ , (C)  $[AHL]=0.74 \mu\text{M}$ , (D)  $[AHL]=0.24 \mu\text{M}$ , (E)  $[AHL]=0.08 \mu\text{M}$ , (F)  $[AHL]=0.03 \mu\text{M}$  (G)  $[AHL]=0.009 \mu\text{M}$ , (H)  $[AHL]=0.00 \mu\text{M}$ . This experimental data was used for generating Fig.S19C.



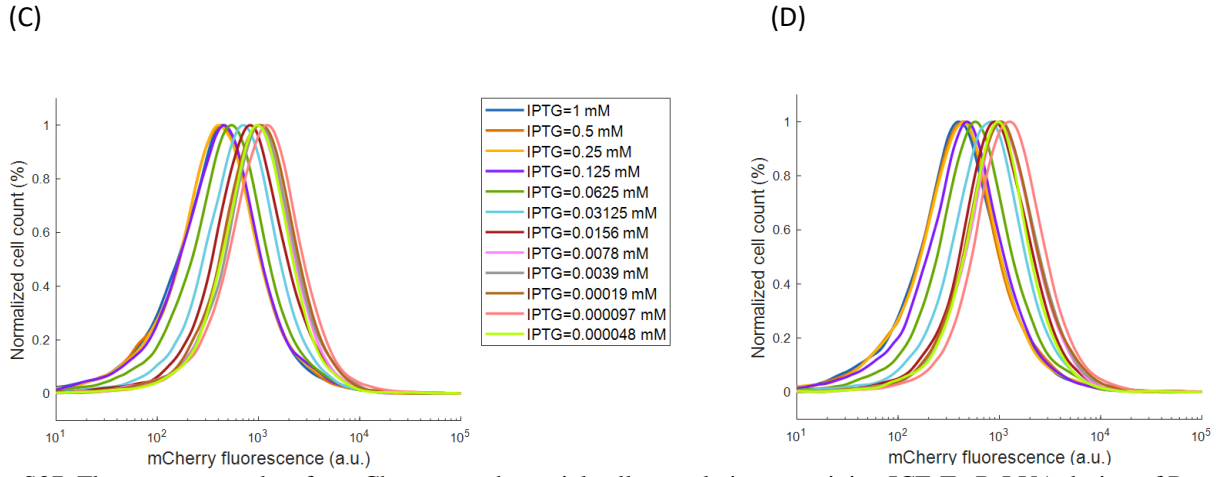
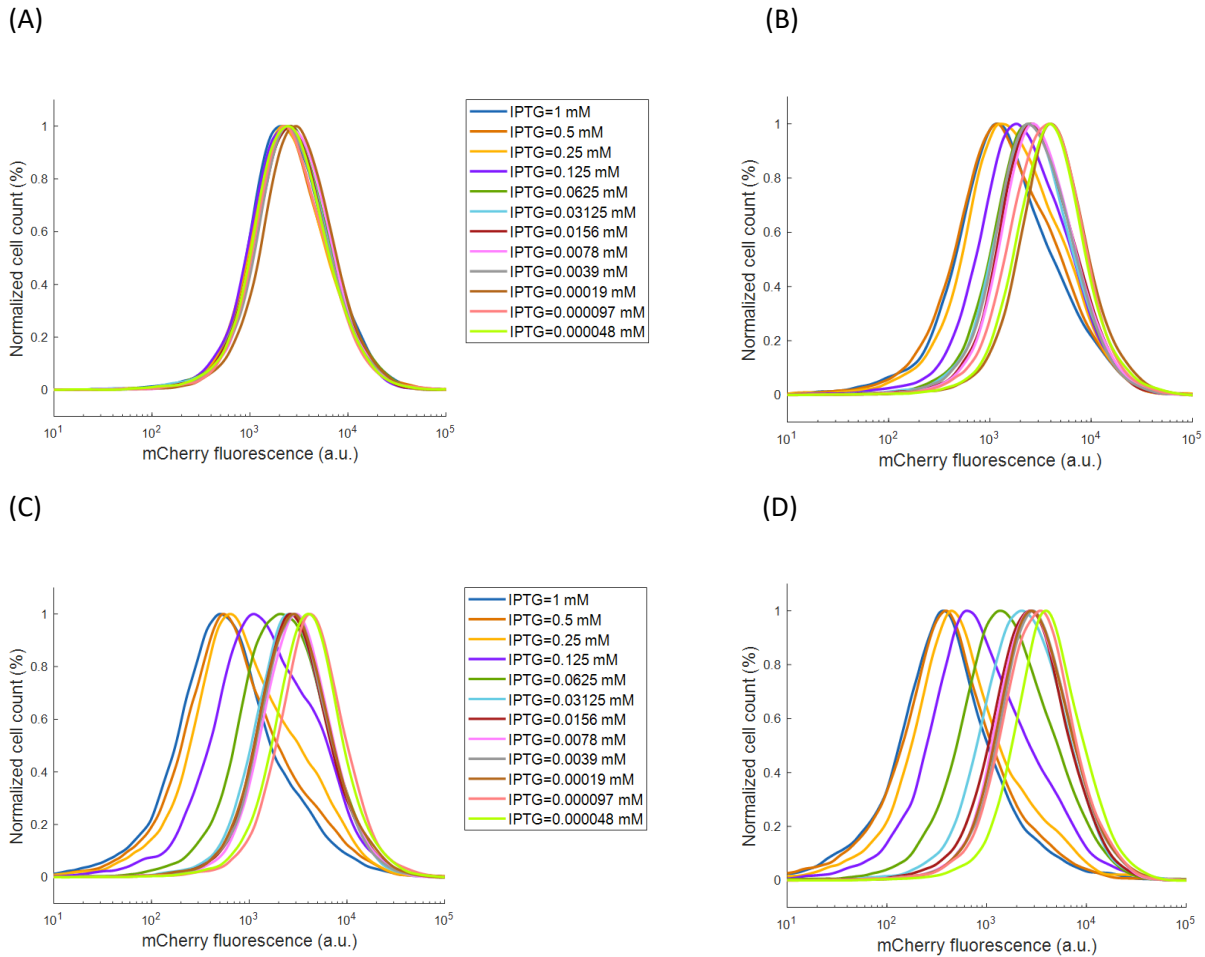


Fig. S37. Flow cytometry data for mCherry over bacterial cells population containing ICF-TetR-LVA design of  $P_{lacO}$ . (A)  $[AHL]=6.66 \mu M$ , (B)  $[AHL]=0.74 \mu M$ , (C)  $[AHL]=0.08 \mu M$ , (D)  $[AHL]=0.009 \mu M$ . This experimental data was used for generating Fig.S19C.



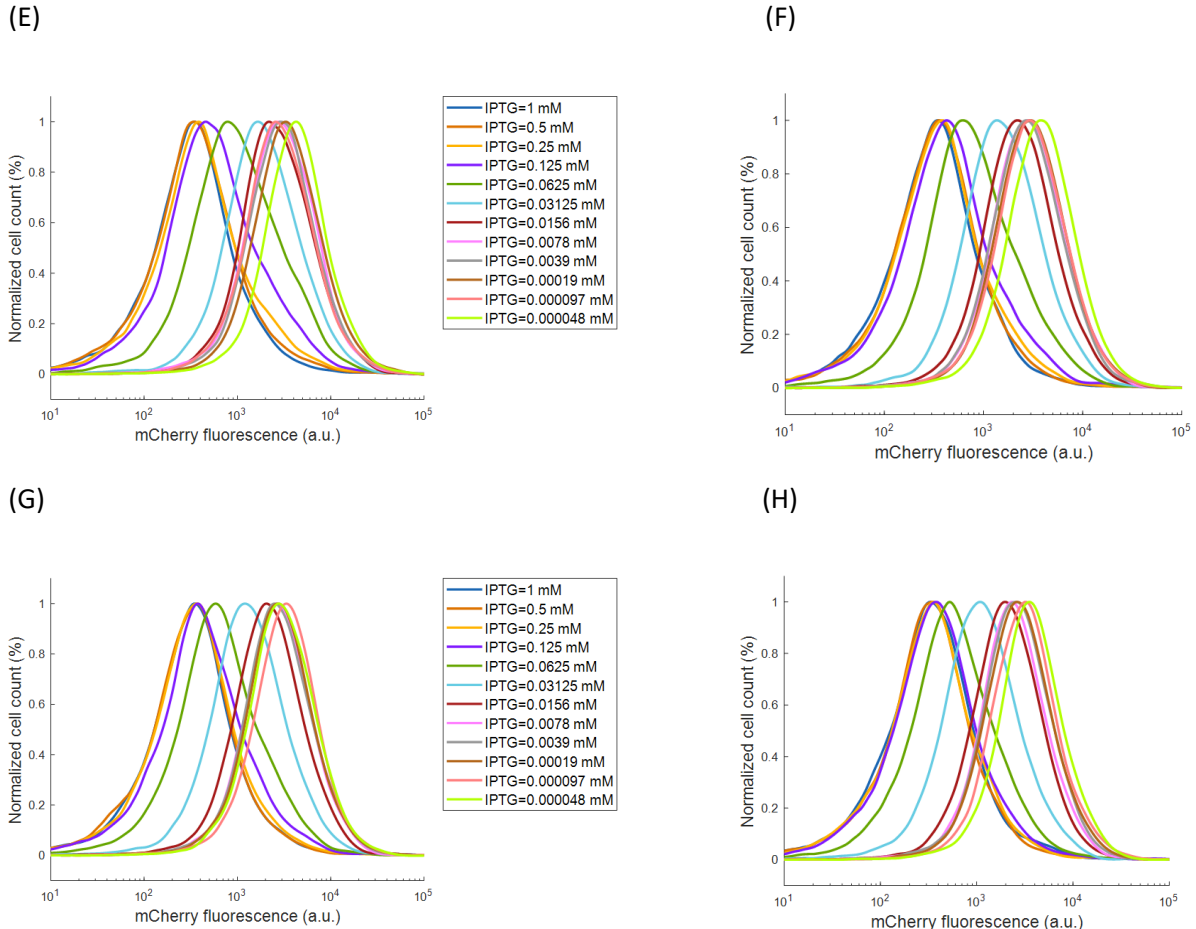


Fig. S38. Flow cytometry data for mCherry over bacterial cells population containing IPTG-aTc inverting switch design of  $P_{laco}$ . (A)[aTc]=100ngr/ml, (B)[aTc]=33.33ngr/ml, (C)[aTc]=11.11ngr/ml, (D) [aTc]=3.7ngr/ml, (E) [aTc]=1.23ngr/ml, (F) [aTc]=0.411ngr/ml, (G) [aTc]=0.137ngr/ml, (H) [aTc]=0ngr/ml. This experimental data was used for generating Fig.S19B.

#### 4.3 Experimental data for native specific promoter $P_{LhrtO}$ .

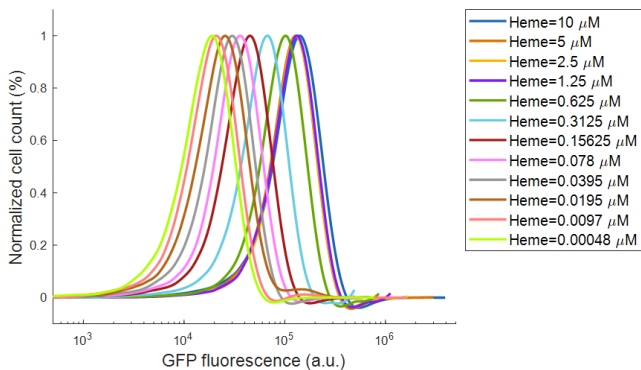
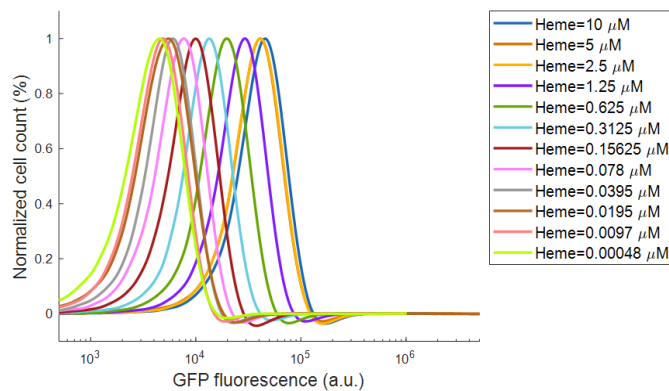
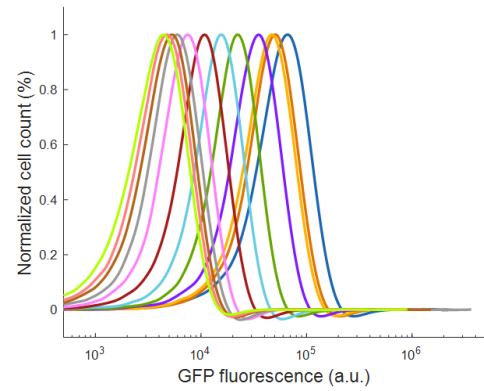


Fig. S39. Flow cytometry data for GFP over bacterial cells population containing wild-type design of  $P_{LhrtO}$ . This experimental data was used for generating Fig.7A and Fig.S20A.

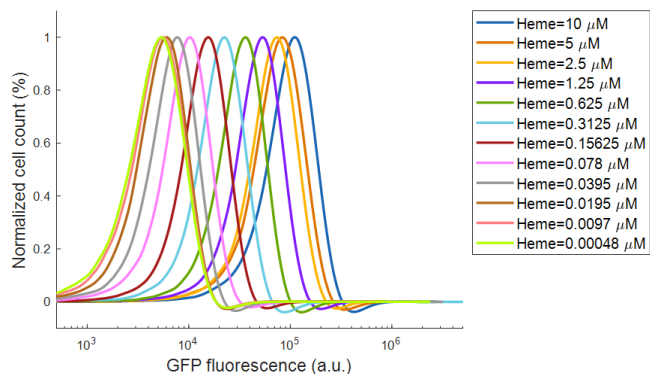
(A)



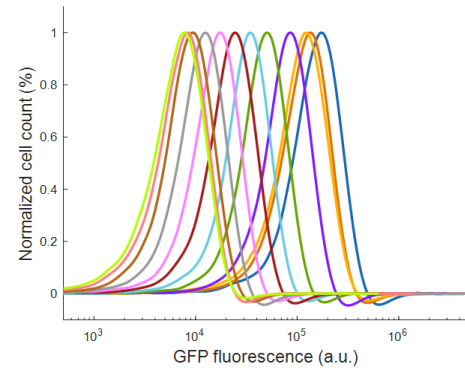
(B)



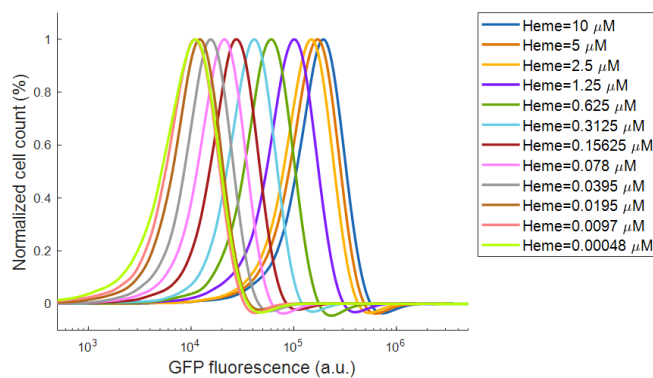
(C)



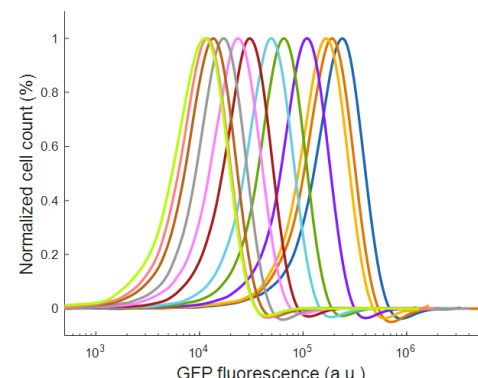
(D)



(E)



(F)



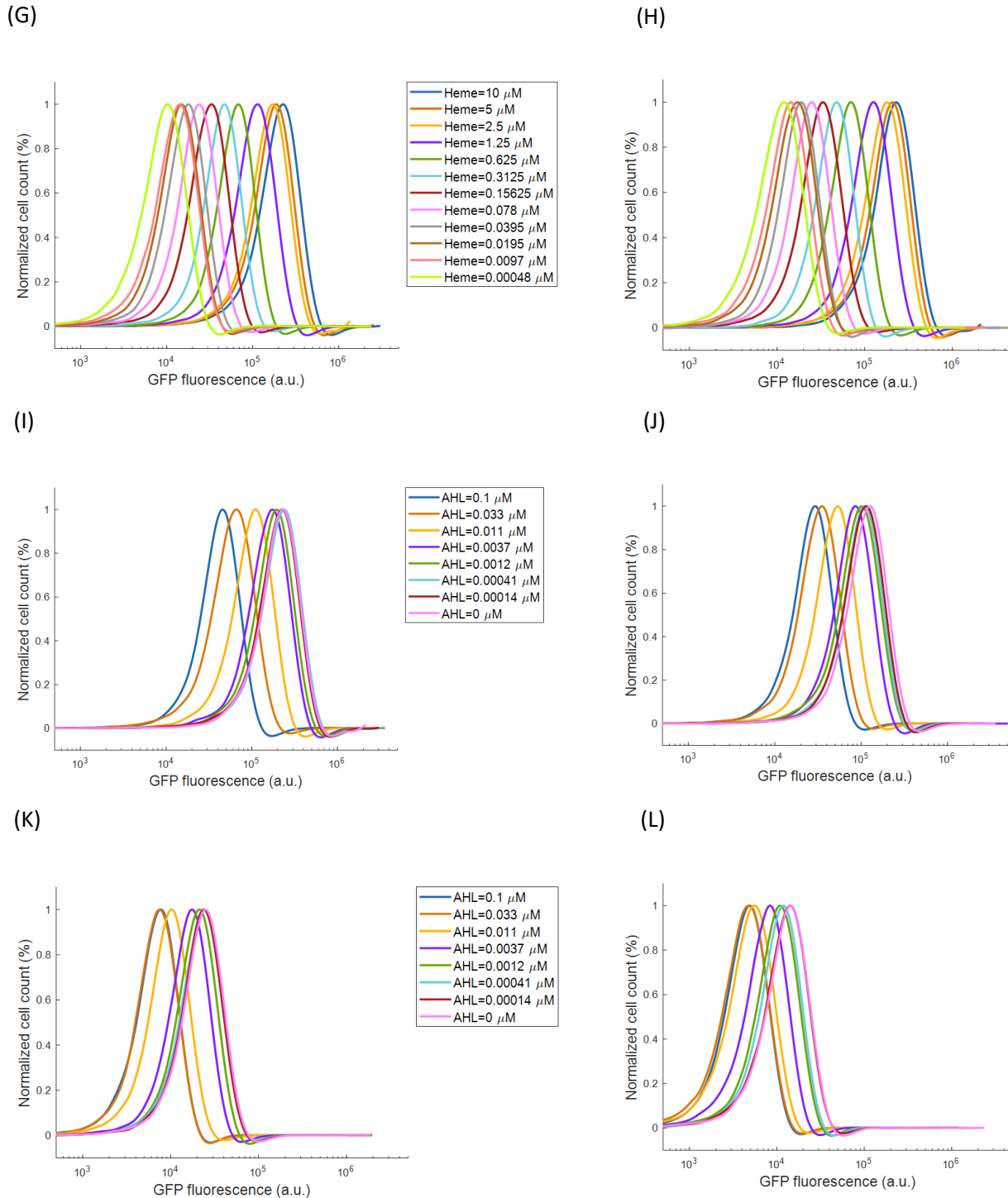


Fig. S40. Flow cytometry data for GFP over bacterial cells population containing OL design of  $P_{LhrtO}$ . (A)  $[AHL]=0.1 \mu M$ , (B)  $[AHL]=0.033 \mu M$ , (C)  $[AHL]=0.011 \mu M$ , (D)  $[AHL]=0.0037 \mu M$ , (E)  $[AHL]=0.0012 \mu M$ , (F)  $[AHL]=0.00041 \mu M$ , (G)  $[AHL]=0.00014 \mu M$ , (H)  $[AHL]=0 \mu M$ , (I)  $[Heme]=10 \mu M$ , (J)  $[Heme]=1.25 \mu M$ , (K)  $[Heme]=0.078 \mu M$ , (L)  $[Heme]=0.00977 \mu M$ . This experimental data was used for generating Fig.7B and Fig.S20B.

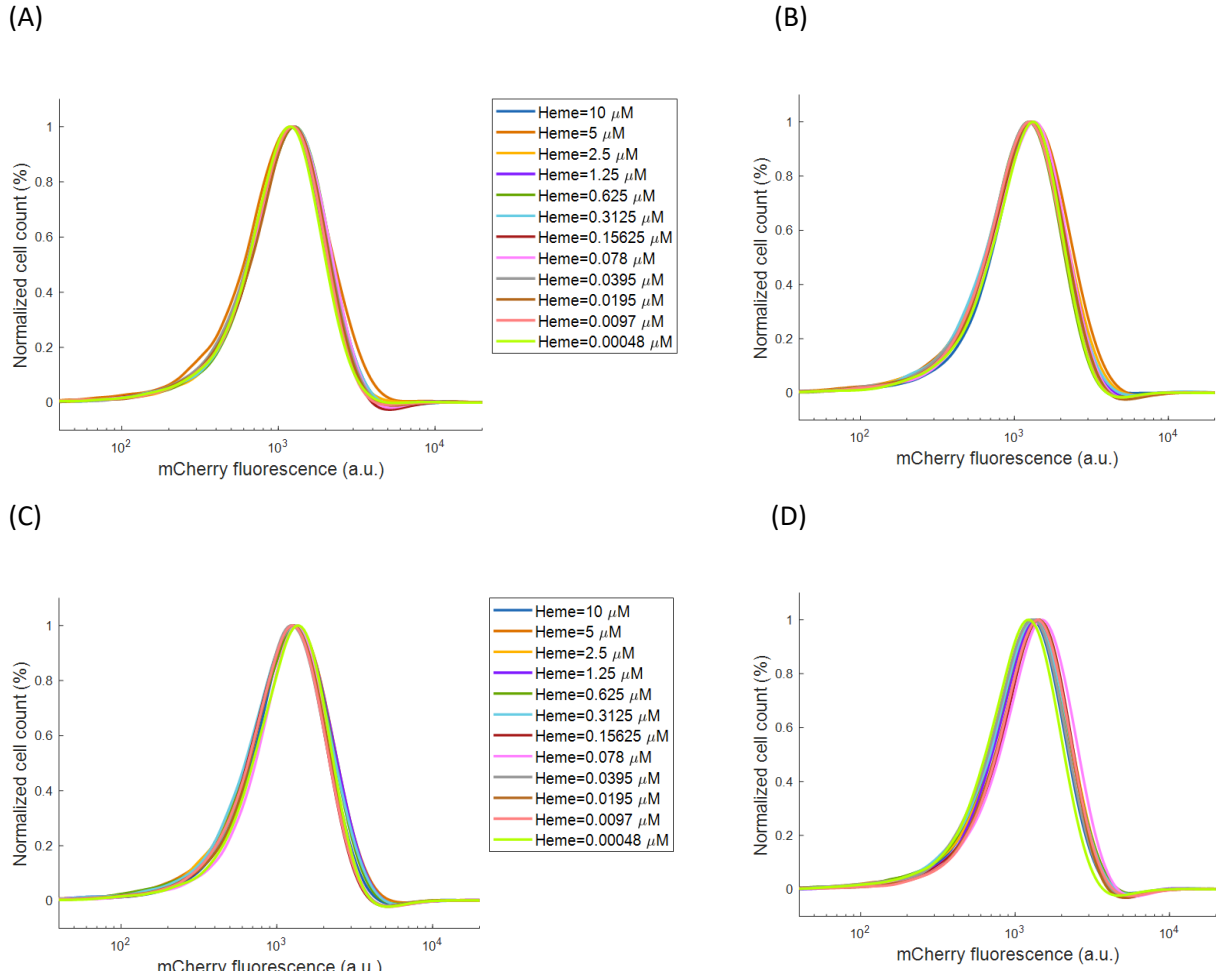
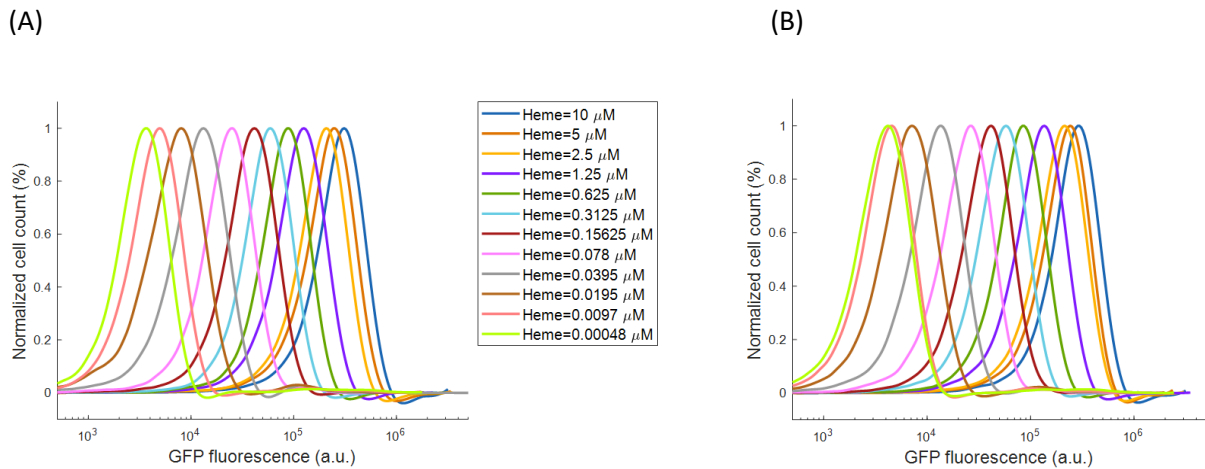


Fig. S41. Flow cytometry data for mCherry over bacterial cells population containing OL design of  $P_{LhrtO}$ . (A)  $[AHL]=0.1 \mu M$ , (B)  $[AHL]=0.011 \mu M$ , (C)  $[AHL]=0.0012 \mu M$ , (D)  $[AHL]=0.00014 \mu M$ . This experimental data was used for generating Fig.S20B.



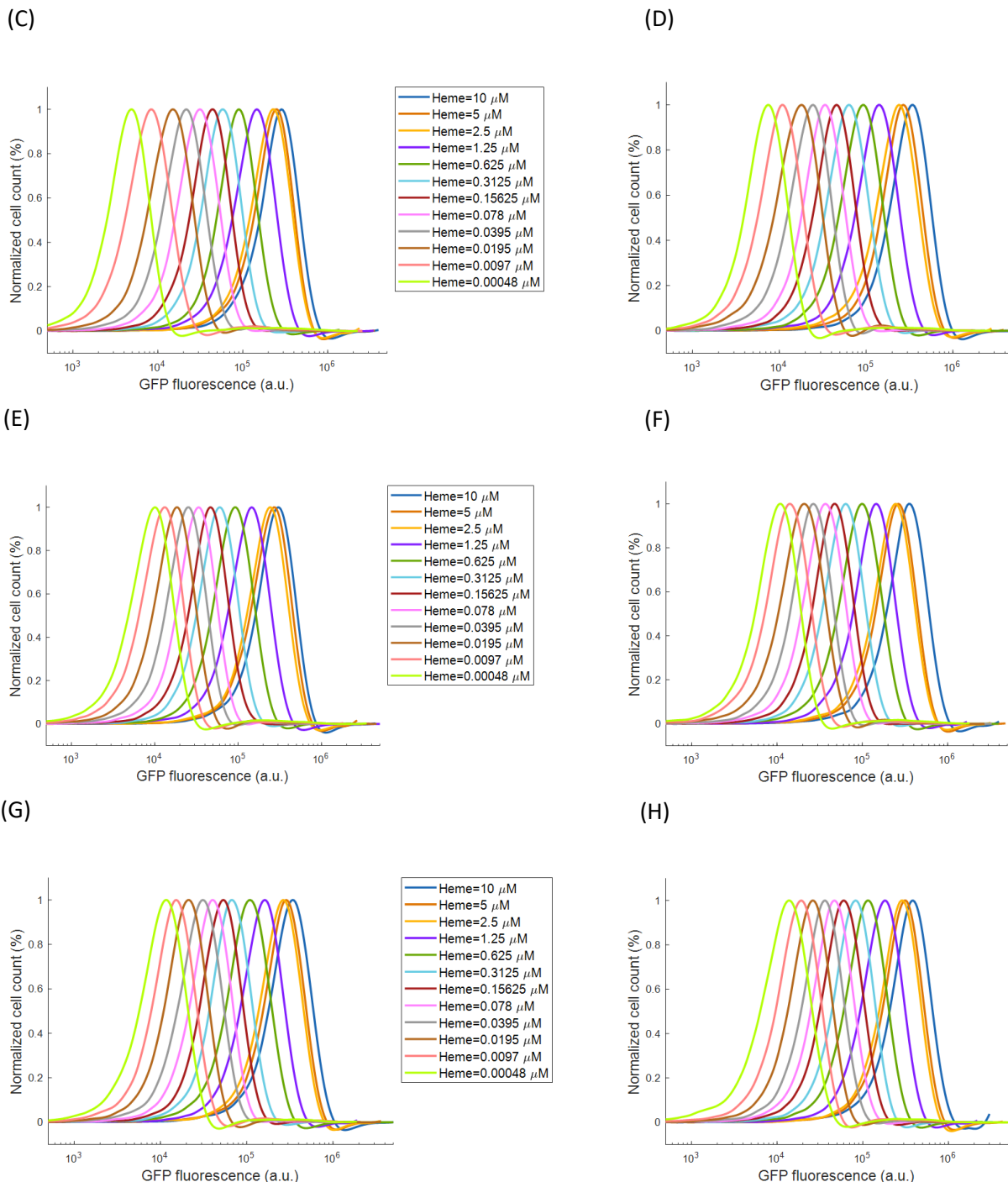


Fig. S42. Flow cytometry data for GFP over bacterial cells population containing ICF-TetR-AAV design of  $P_{LhrtO}$ . (A)  $[AHL]=0.1 \mu M$ , (B)  $[AHL]=0.033 \mu M$ , (C)  $[AHL]=0.011 \mu M$ , (D)  $[AHL]=0.0037 \mu M$ , (E)  $[AHL]=0.0012 \mu M$ , (F)  $[AHL]=0.0004 \mu M$ , (G)  $[AHL]=0.0001 \mu M$ , (H)  $[AHL]=0 \mu M$ . ( $[aTc]=11.11 \text{ ngr/ml}$ ). This experimental data was used for generating Fig.7C and Fig.S20D.

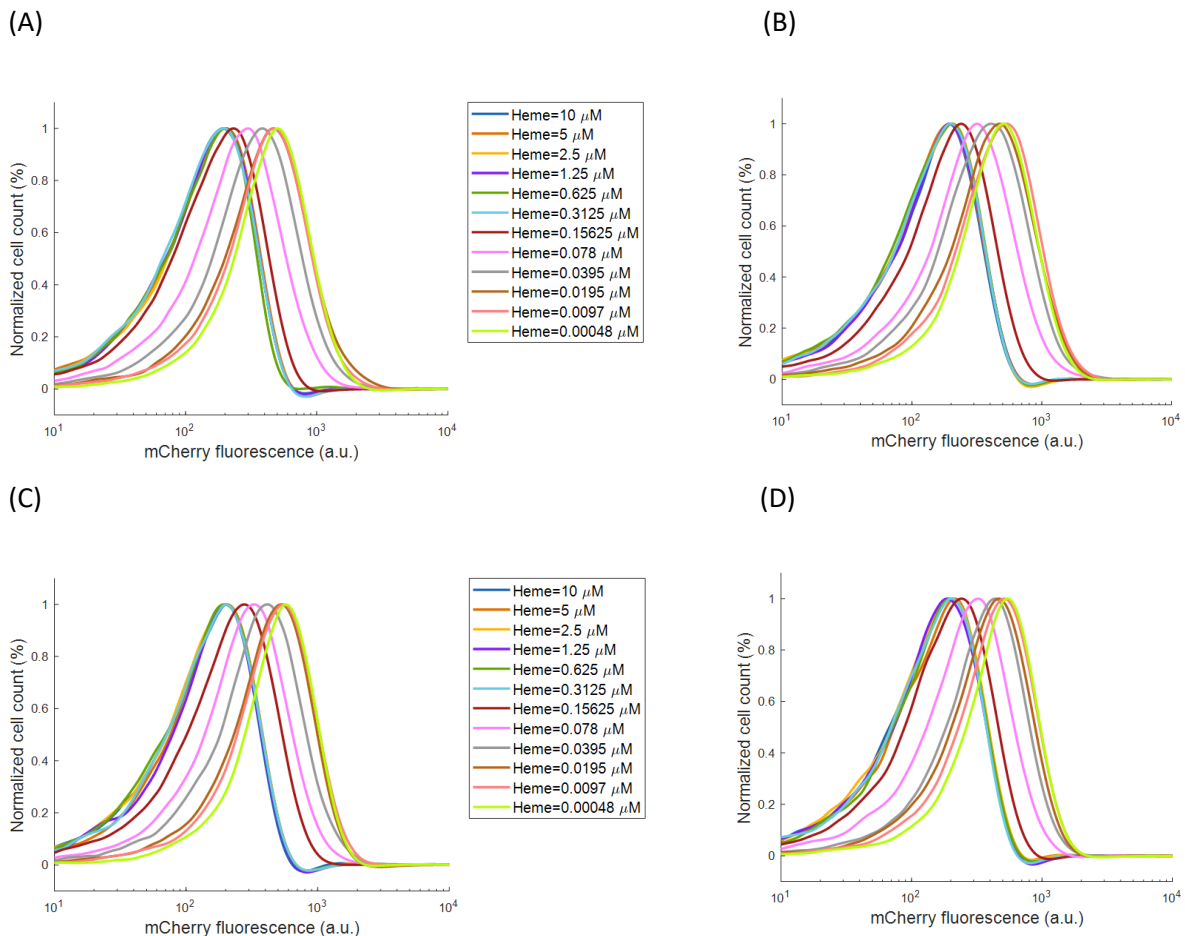
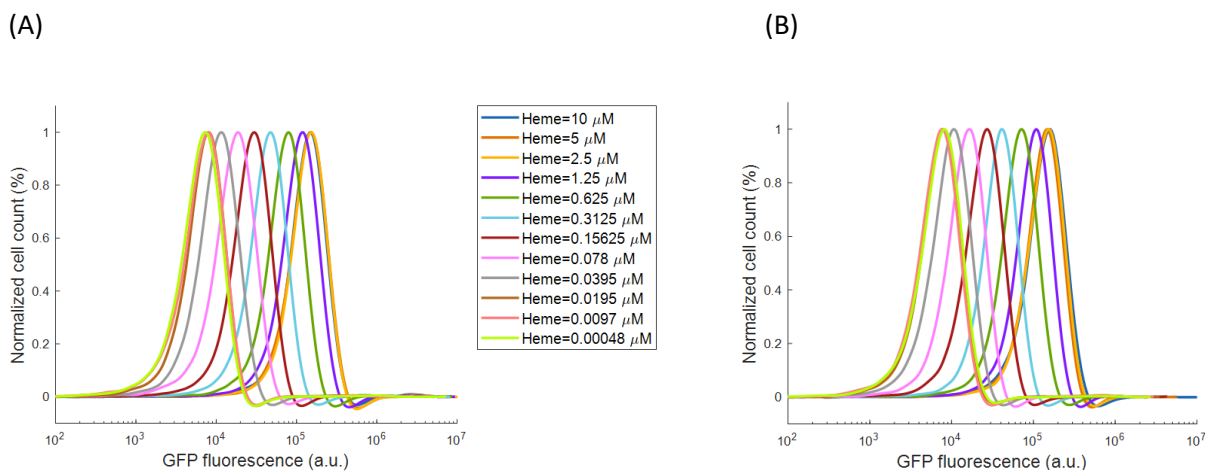


Fig. S43. Flow cytometry data for mCherry over bacterial cells population containing ICF-TetR-AAV design of  $P_{LhrtO}$ . (A) [AHL]=0.1  $\mu$ M, (B) [AHL]=0.011  $\mu$ M, (C) [AHL]=0.0012  $\mu$ M, (D) [AHL]=0.00014  $\mu$ M. ([aTc]=11.1ng/ml). This experimental data was used for generating Fig.S20D.



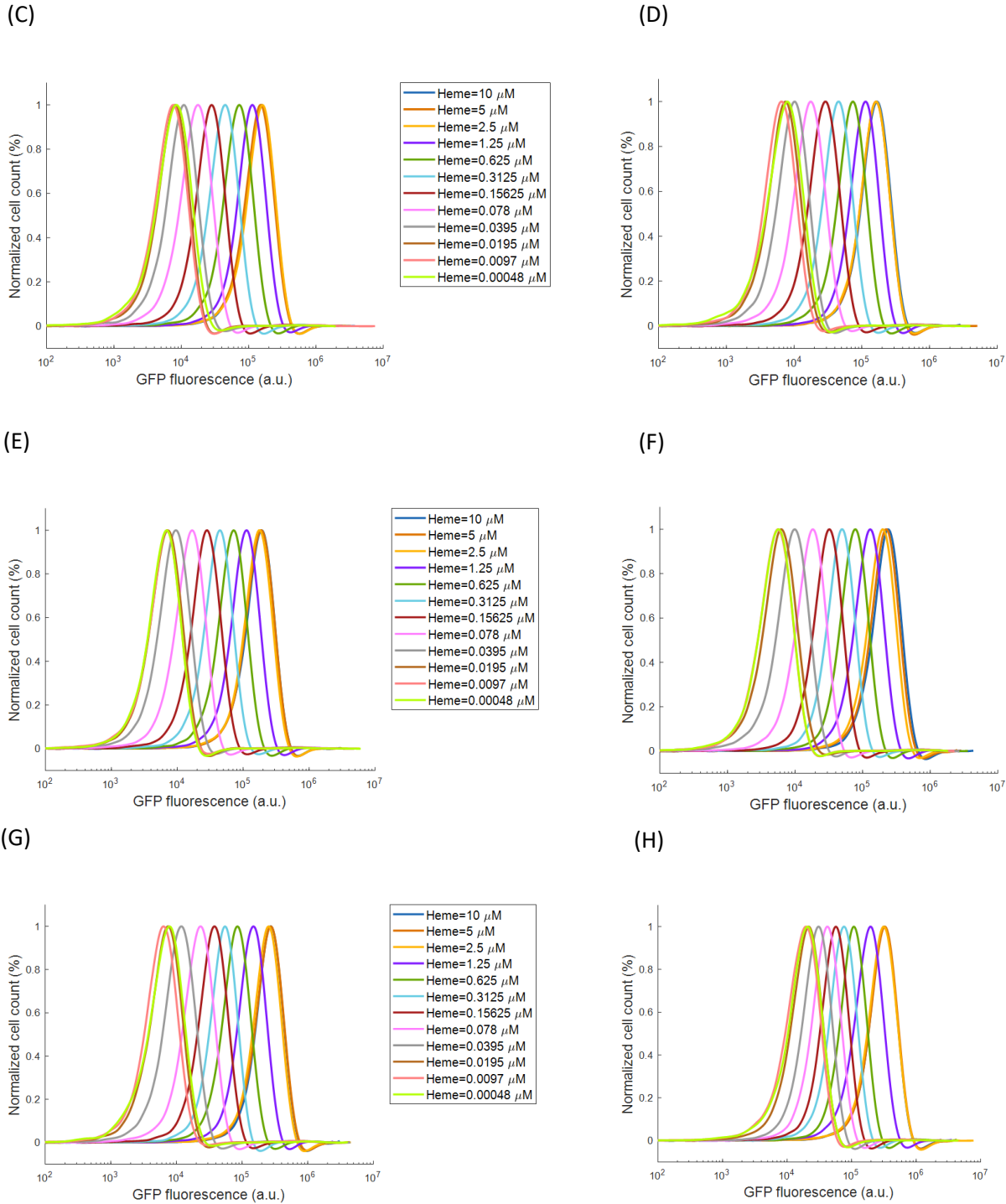


Fig. S44. Flow cytometry data for GFP over bacterial cells population containing DNF-TetR-AAV design of  $P_{LhrtO}$ . (A)  $[AHL]=0.1 \mu M$ , (B)  $[AHL]=0.033 \mu M$ , (C)  $[AHL]=0.011 \mu M$ , (D)  $[AHL]=0.0037 \mu M$ , (E)  $[AHL]=0.0012 \mu M$ , (F)  $[AHL]=0.0004 \mu M$ , (G)  $[AHL]=0.0001 \mu M$ , (H)  $[AHL]=0 \mu M$ . ( $[aTc]=3.7 \text{ ngr/ml}$ ) This experimental data was used for generating Fig.S20E.

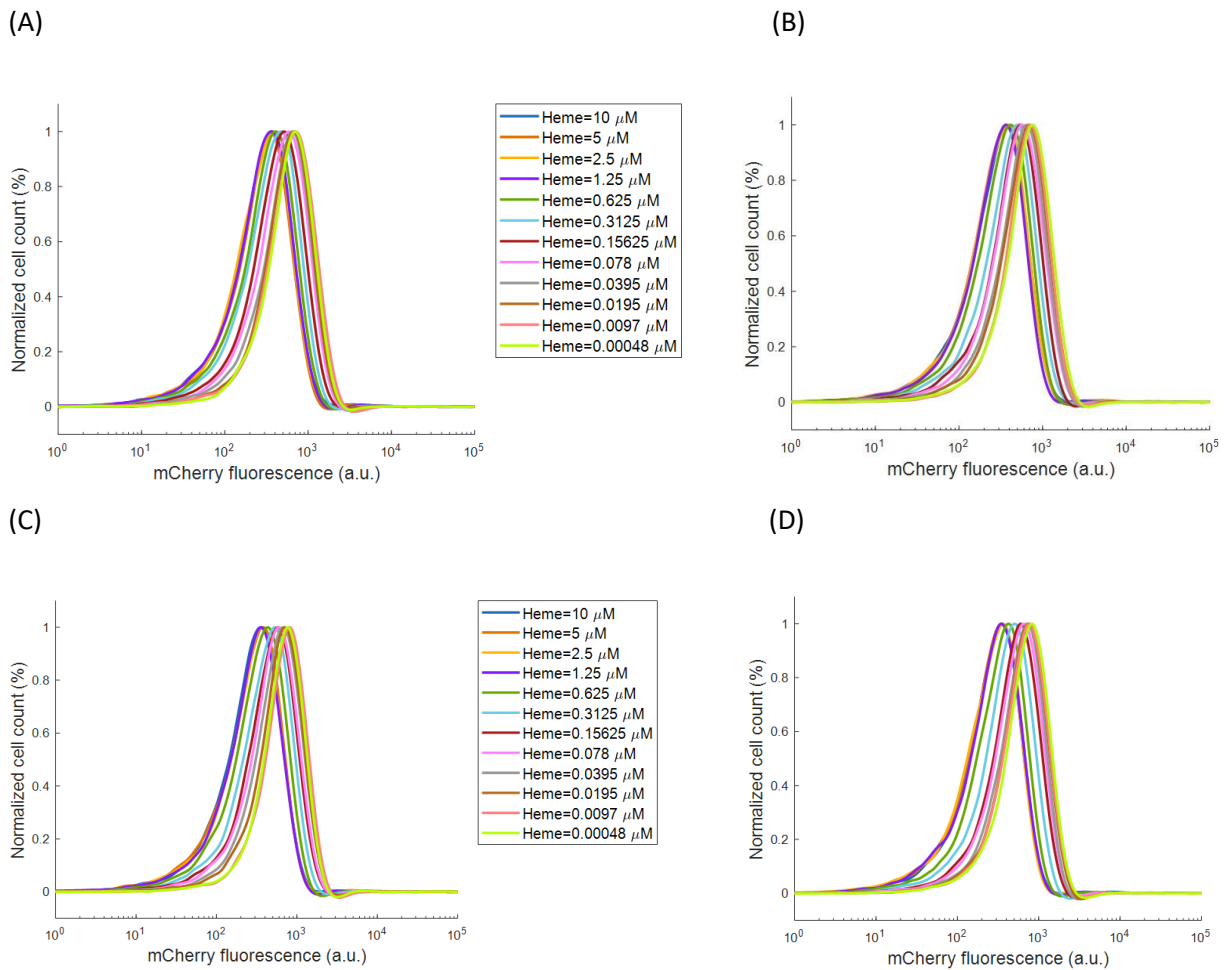
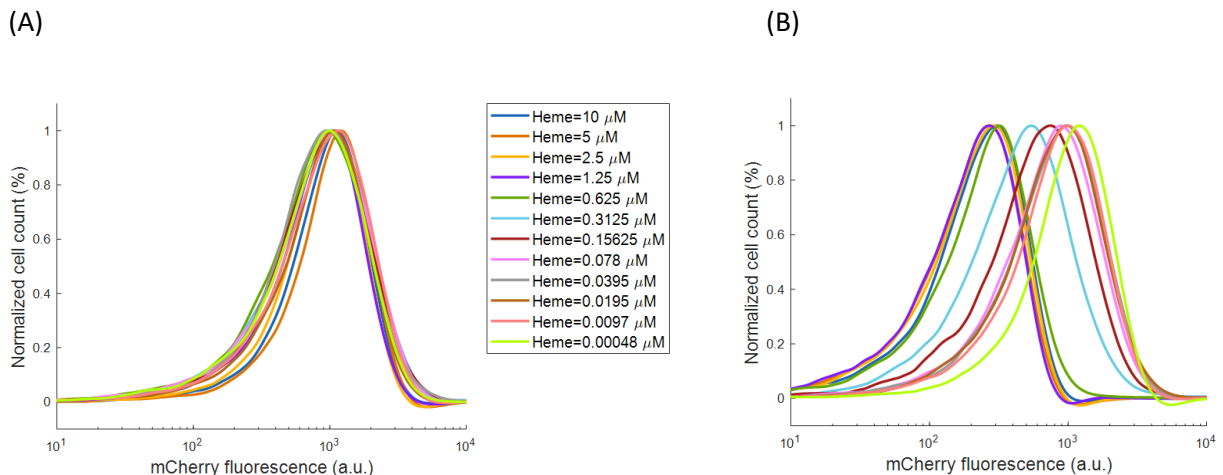


Fig. S45. Flow cytometry data for mCherry over bacterial cells population containing DNF-TetR-AAV design of  $P_{LhrO}$ . (A)  $[AHL]=0.1 \mu M$ , (B)  $[AHL]=0.011 \mu M$ , (C)  $[AHL]=0.0012 \mu M$ , (D)  $[AHL]=0.00014 \mu M$ . ( $[aTc]=3.7\text{ng}/\text{ml}$ ) This experimental data was used for generating Fig.S20E.



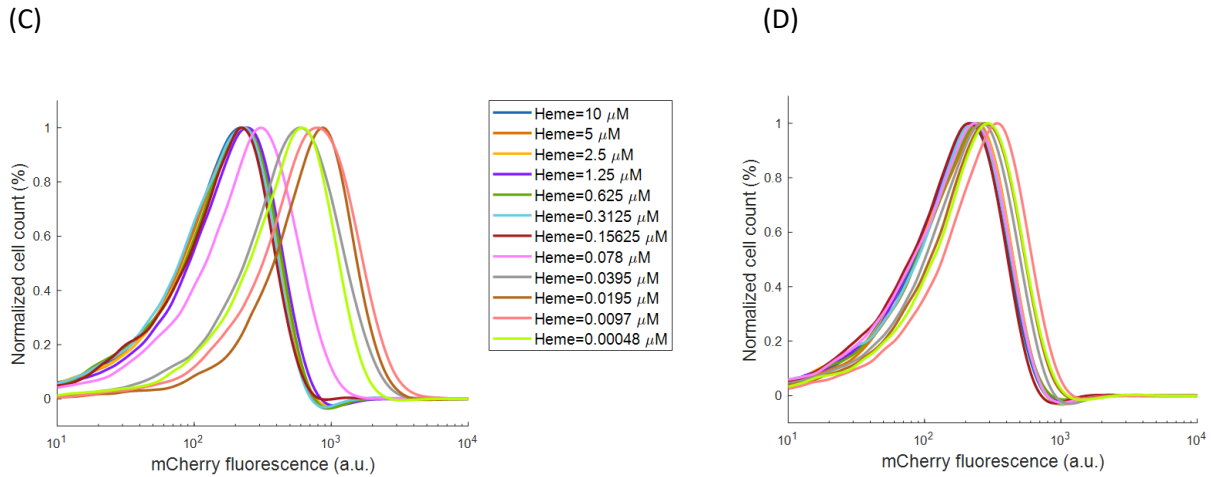


Fig. S46. Flow cytometry data for mCherry over bacterial cells population containing Heme-aTc inverting switch for ICF design of  $P_{LhrtO}$ . (A)  $[AHL]=0.1\ \mu M$ , (B)  $[AHL]=0.011\ \mu M$ , (C)  $[AHL]=0.0012\ \mu M$ , (D)  $[AHL]=0.00014\ \mu M$ . This experimental data was used for generating Fig.S20C.

#### 4.4 Experimental data for native specific promoter $P_{arsR}$

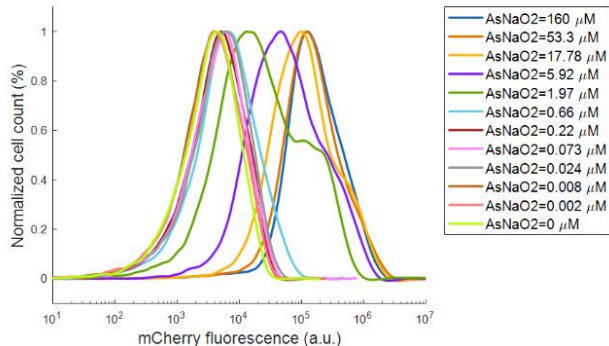
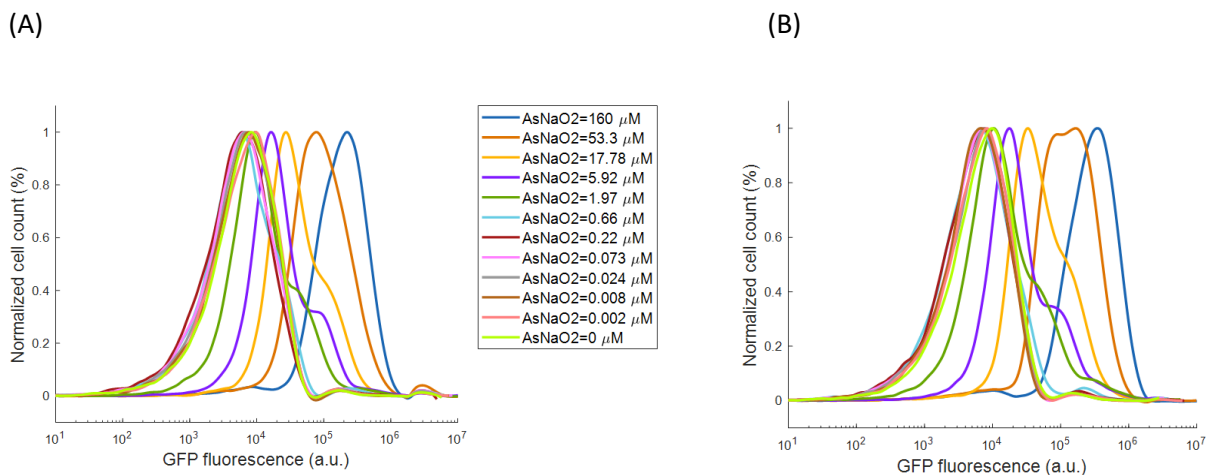
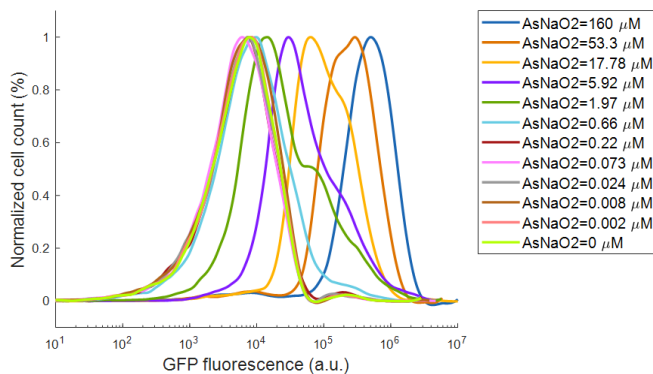


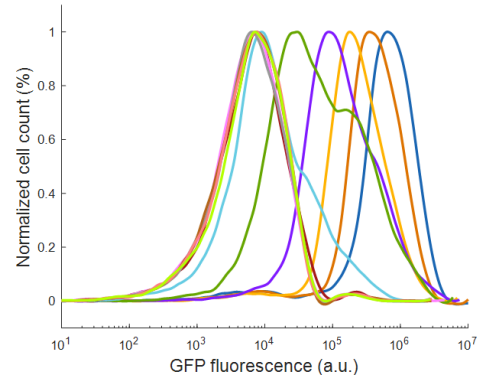
Fig. S47. Flow cytometry data for GFP over bacterial cells population containing  $P_{arsR}$  wild-type design. This experimental data was used for generating Fig.S21A.



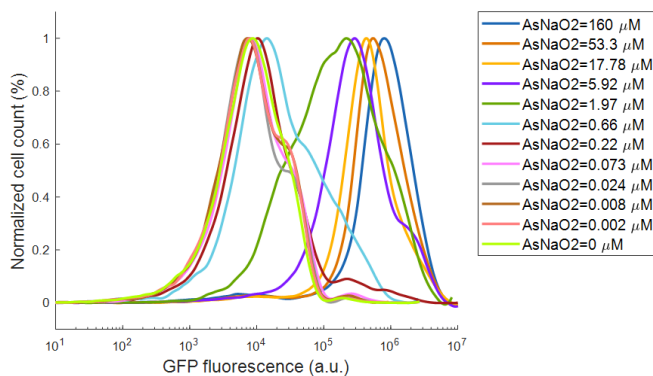
(C)



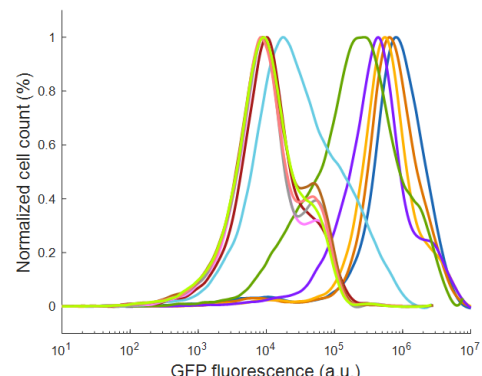
(D)



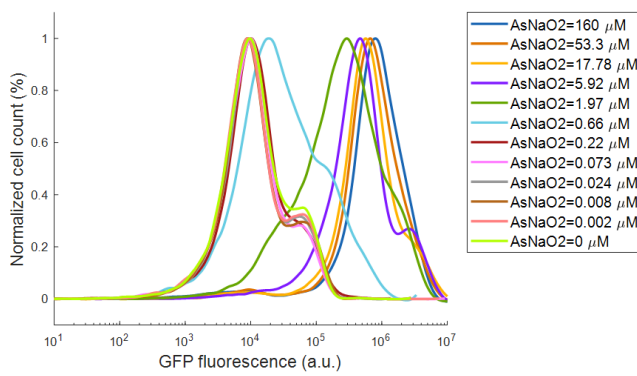
(E)



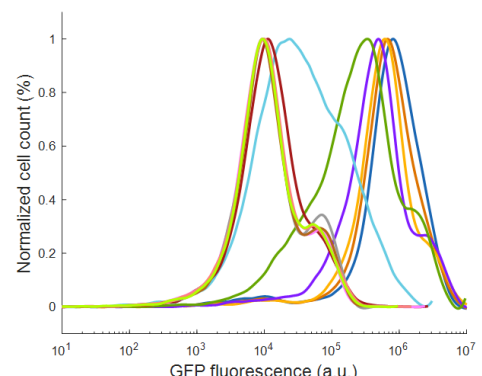
(F)



(G)



(H)



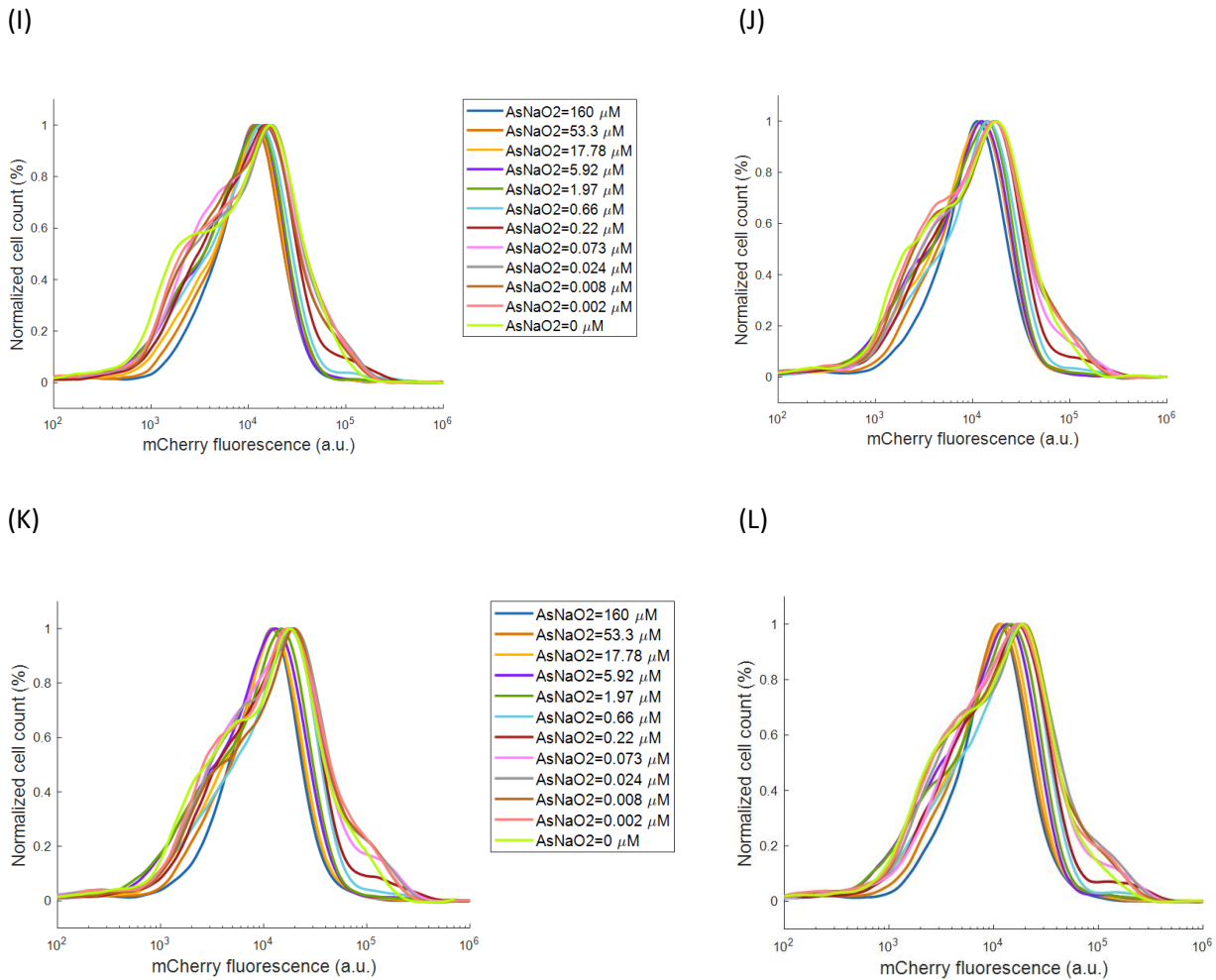
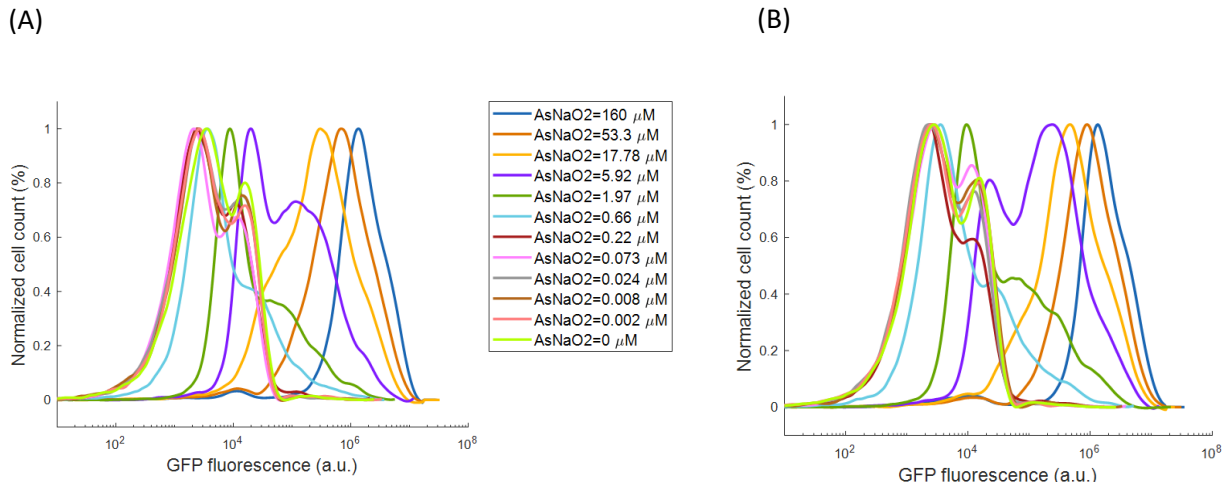


Fig. S48. Flow cytometry data for GFP over bacterial cells population containing OL design of ParsR. (A) [AHL]=0.1371  $\mu$ M, (B) [AHL]=0.0457  $\mu$ M, (C) [AHL]=0.0152  $\mu$ M, (D) [AHL]=0.0051  $\mu$ M, (E) [AHL]=0.0017  $\mu$ M, (F) [AHL]=0.00056  $\mu$ M, (G) [AHL]=0.00019  $\mu$ M, (H) [AHL]=0  $\mu$ M. (I-L) Flow cytometry data for mCherry over bacterial cells population containing OL design. (I) [AHL]=0.0457  $\mu$ M, (J) [AHL]=0.0051  $\mu$ M, (K) [AHL]=0.00056  $\mu$ M, (L) [AHL]=0  $\mu$ M. This experimental data was used for generating Fig.7E and Fig.S21B.



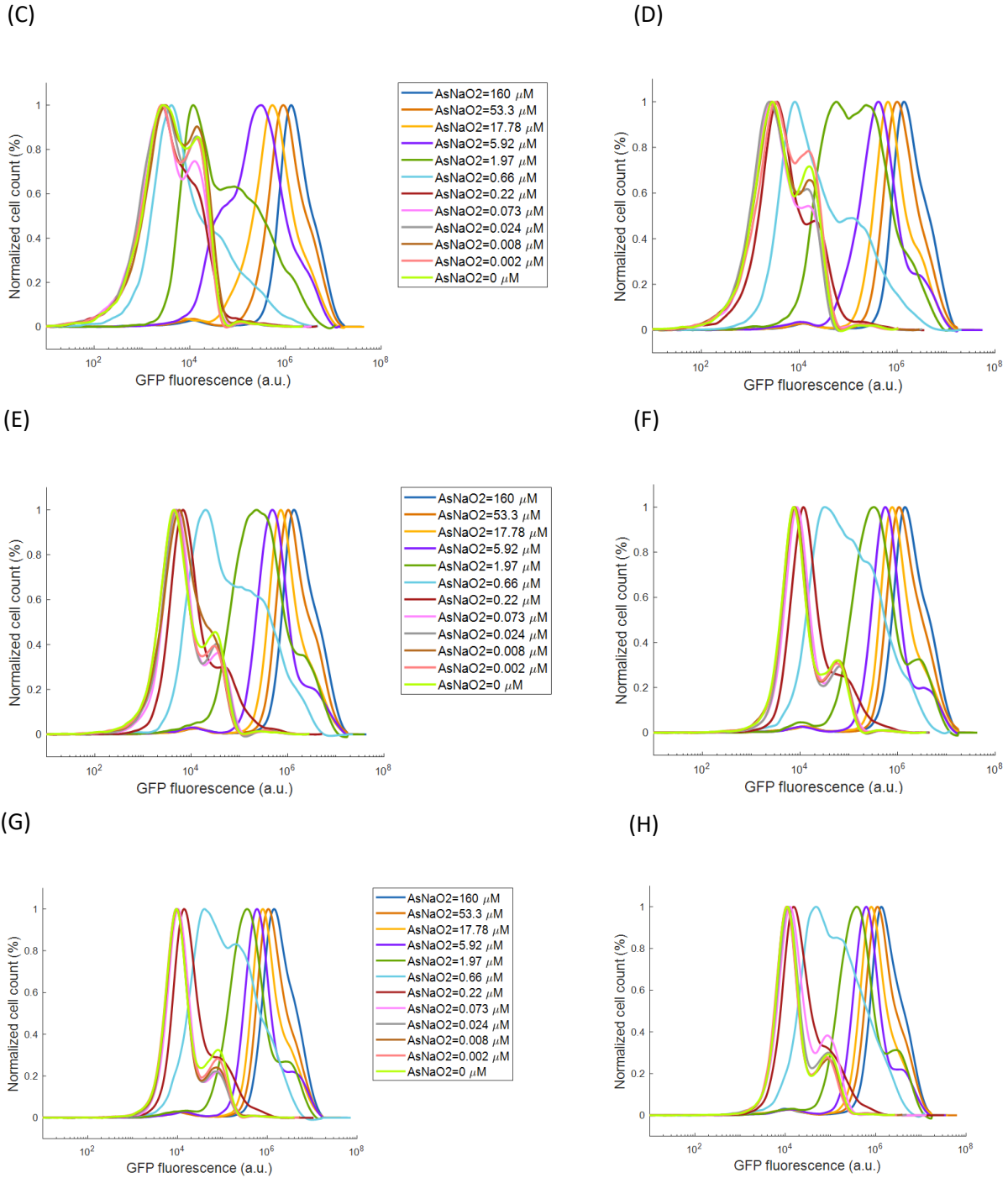


Fig. S49. Flow cytometry data for GFP over bacterial cells population containing ICF design of ParsR. (A) [AHL]=0.1371  $\mu$ M, (B) [AHL]=0.0457  $\mu$ M, (C) [AHL]=0.0152  $\mu$ M, (D) [AHL]=0.0051  $\mu$ M, (E) [AHL]=0.0017  $\mu$ M, (F) [AHL]=0.00056  $\mu$ M, (G) [AHL]=0.00019  $\mu$ M, (H) [AHL]=0  $\mu$ M. This experimental data was used for generating Fig.7F and Fig.S21D.

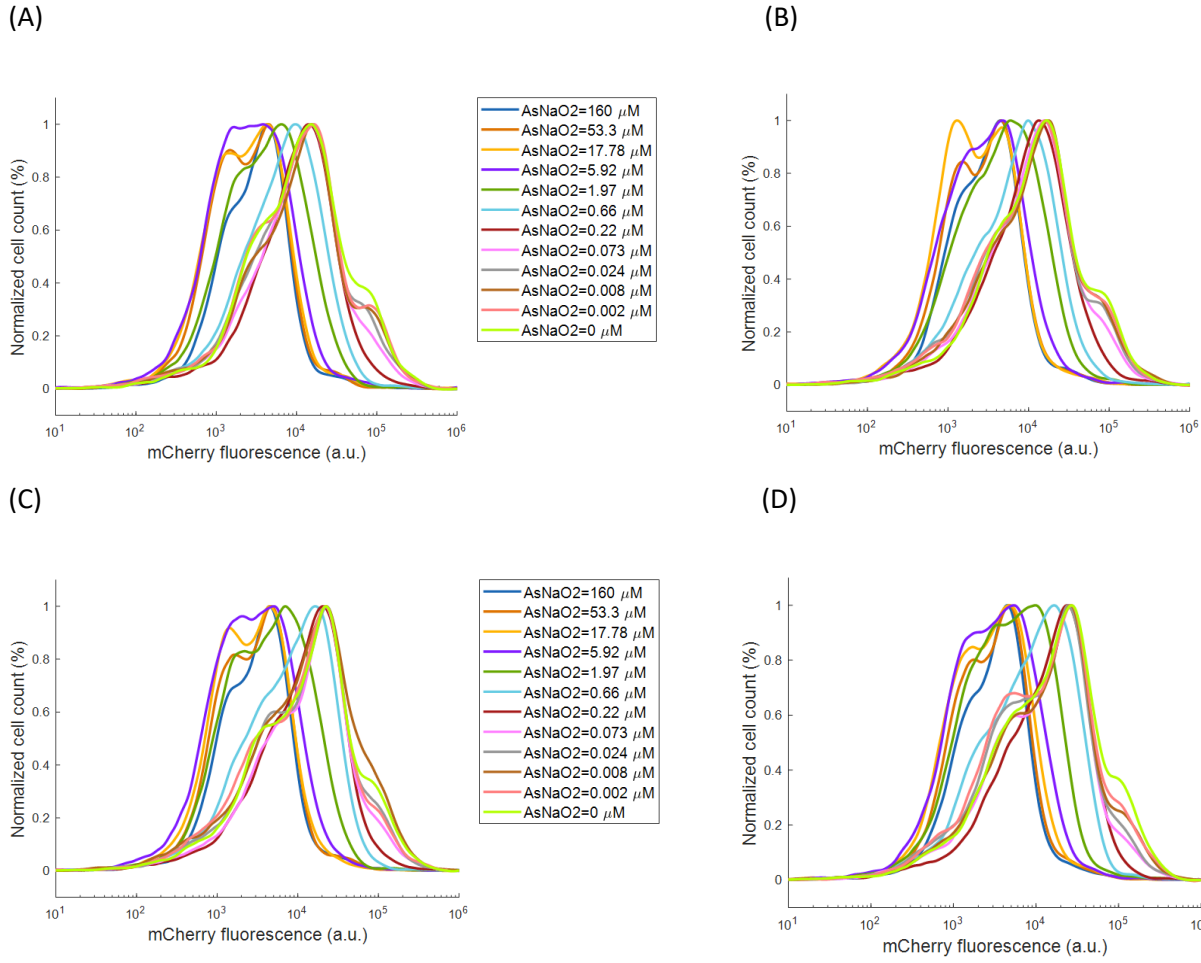
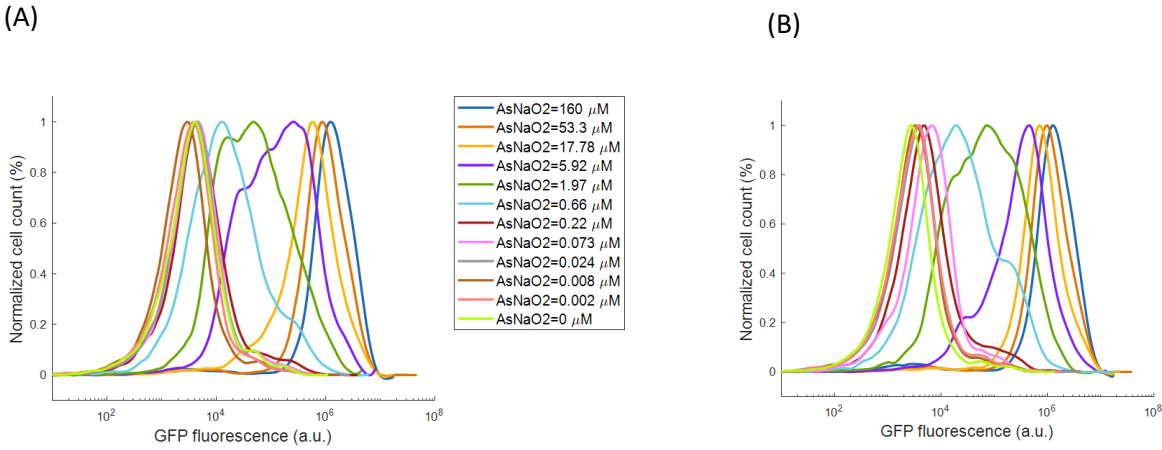


Fig. S50. Flow cytometry data for mCherry over bacterial cells population containing ICF design of  $P_{arsR}$ . (A)  $[AHL]=0.1371 \mu M$ , (B)  $[AHL]= 0.0152 \mu M$ , (C)  $[AHL]= 0.0017 \mu M$ , (D)  $[AHL]= 0.00019 \mu M$ . This experimental data was used for generating Fig.S21D.



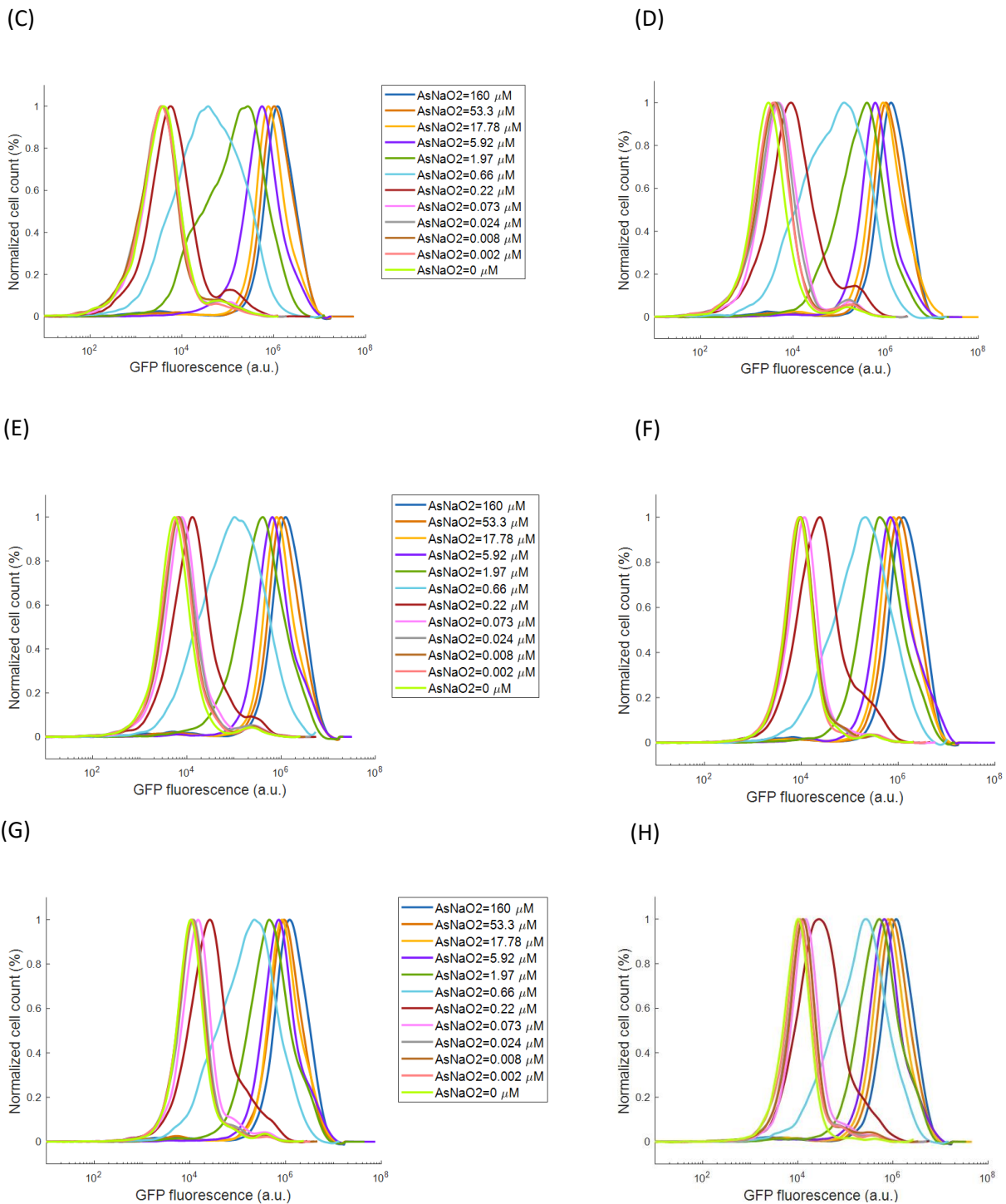


Fig. S51. Flow cytometry data for GFP over bacterial cells population containing DNF design of  $P_{arsR}$ . (A) [AHL]=0.1371  $\mu\text{M}$ , (B) [AHL]=0.0457  $\mu\text{M}$ , (C) [AHL]=0.0152  $\mu\text{M}$ , (D) [AHL]=0.0051  $\mu\text{M}$ , (E) [AHL]=0.0017  $\mu\text{M}$ , (F) [AHL]=0.00056  $\mu\text{M}$ , (G) [AHL]=0.00019  $\mu\text{M}$ , (H) [AHL]=0  $\mu\text{M}$ . This experimental data was used for generating Fig.S21E.

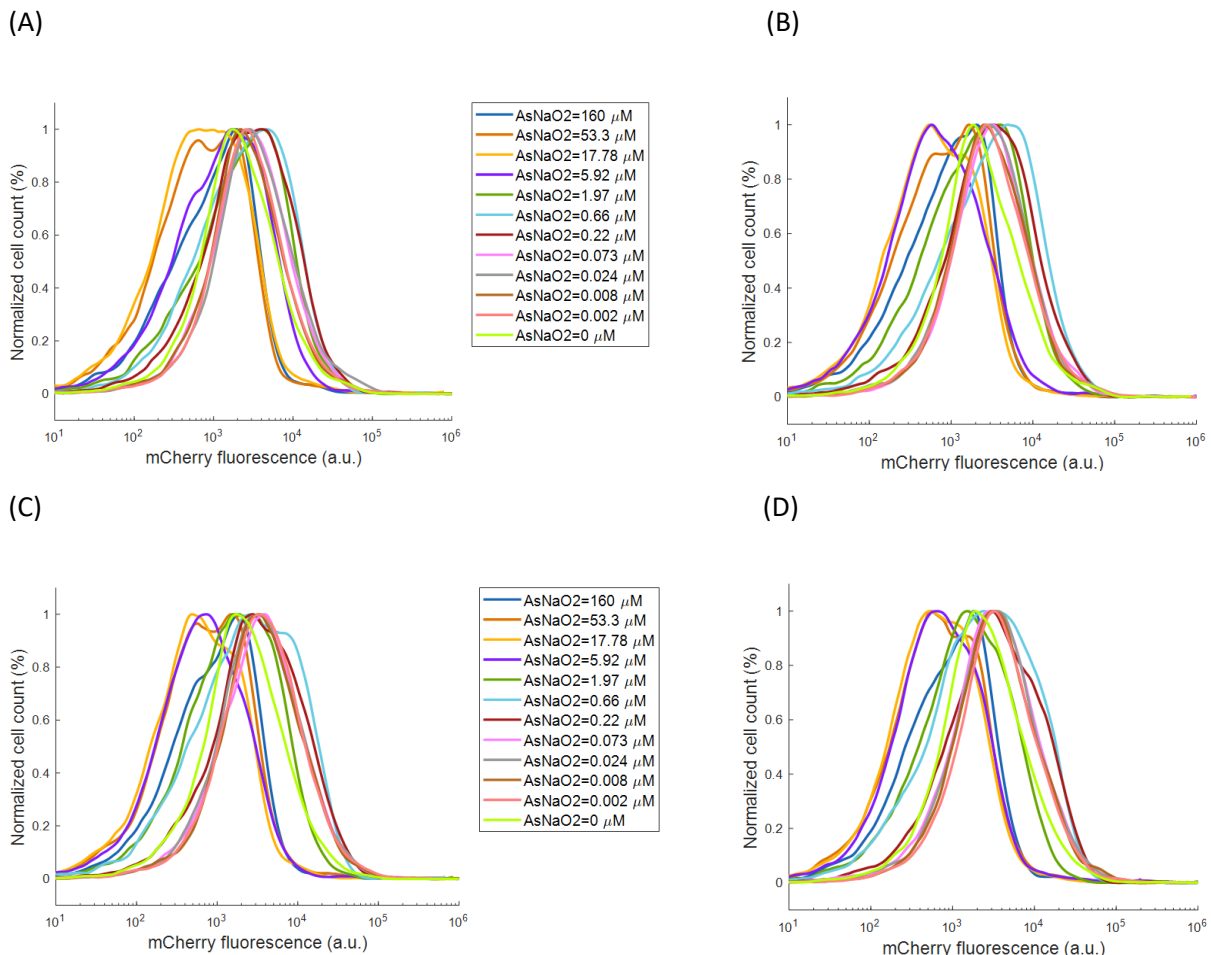
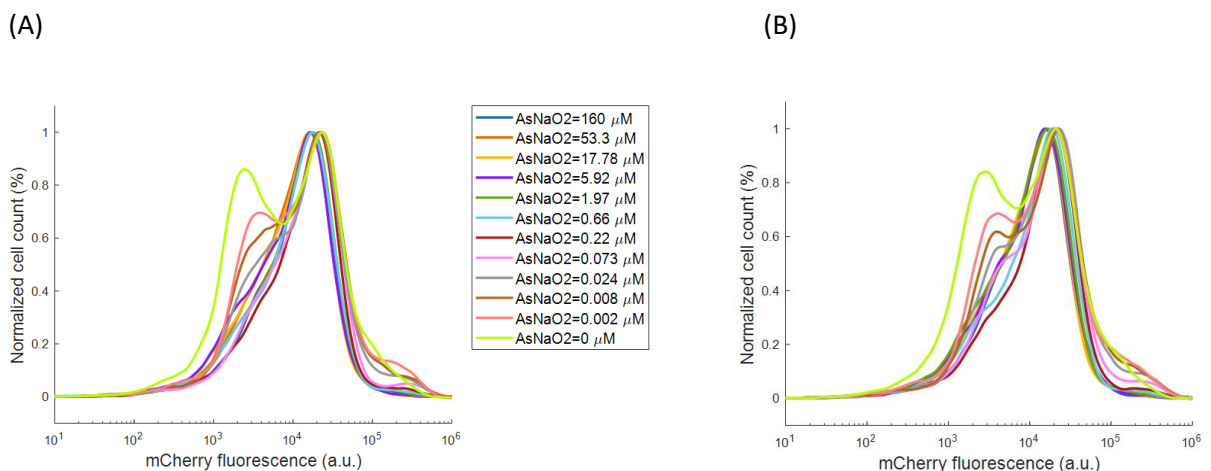
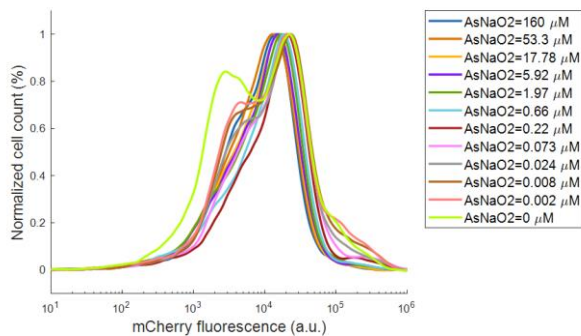


Fig. S52. Flow cytometry data for mCherry over bacterial cells population containing DNF design of  $P_{arsR}$ . (A)  $[AHL]=0.1371 \mu M$ , (B)  $[AHL]= 0.0152 \mu M$ , (C)  $[AHL]= 0.0017 \mu M$ , (D)  $[AHL]= 0.00019 \mu M$ . This experimental data was used for generating Fig.S21E.



(C)



(D)

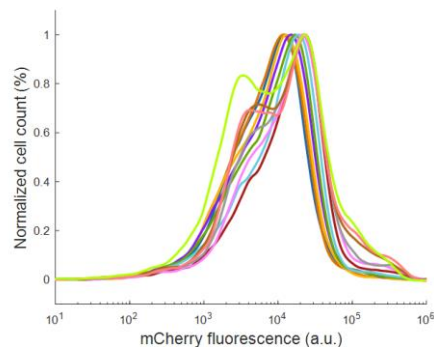


Fig. S53. Flow cytometry data for mCherry over bacterial cells population containing AsNaO<sub>2</sub>-aTc inverting switch design of P<sub>arsR</sub>. (A) [aTc]=100ngr/ml, (B) [aTc]= 11.1ngr/ml, (C) [aTc]= 1.23ngr/ml, (D) [aTc]= 0.137 ngr/ml. This experimental data was used for generating Fig.S21C.

#### 4.5 Experimental data for native stress promoter P<sub>katG</sub>

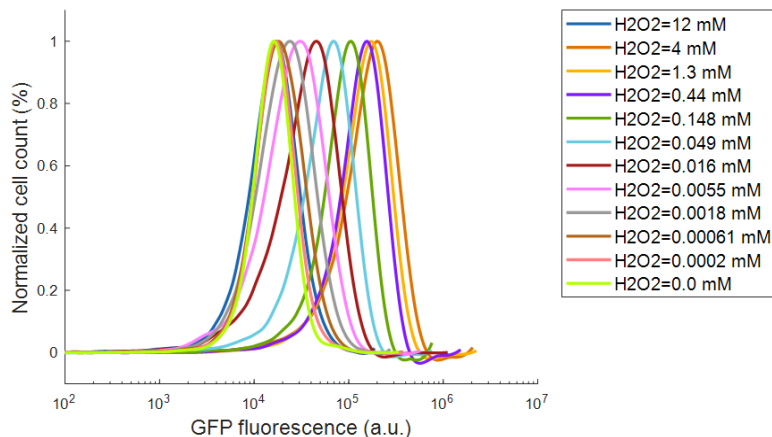
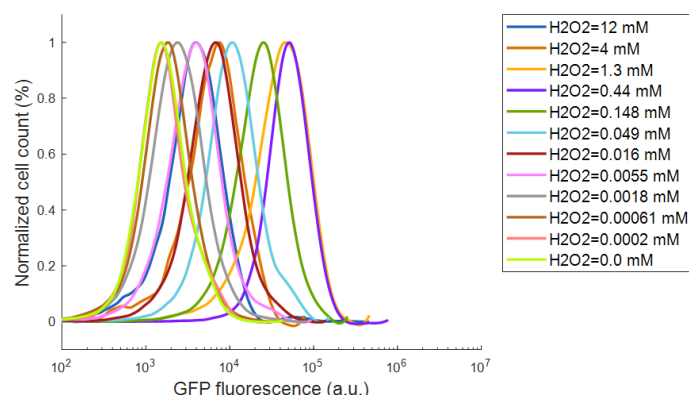
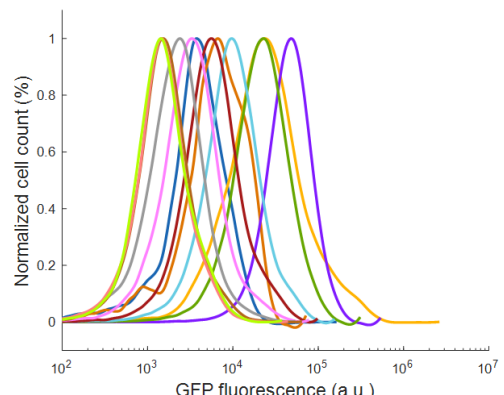


Fig. S54. Flow cytometry data for GFP over bacterial cells population containing wild-type design of P<sub>katG</sub>. This experimental data was used for generating Fig.S22A.

(A)



(B)



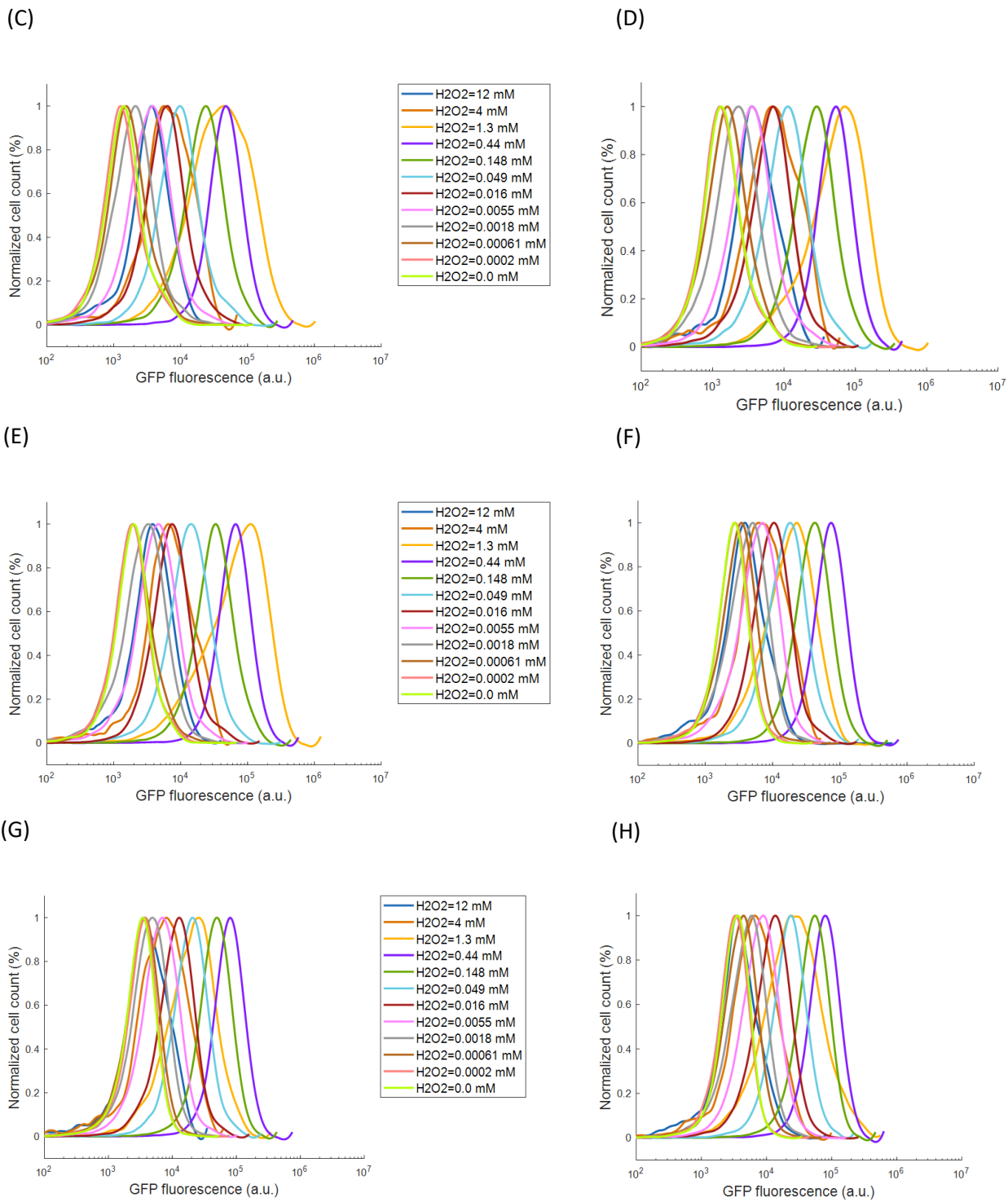
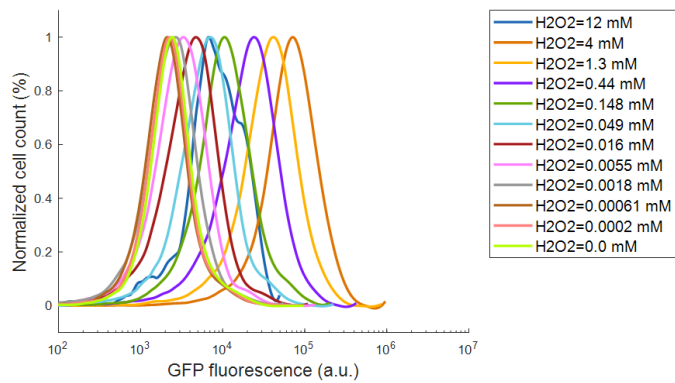
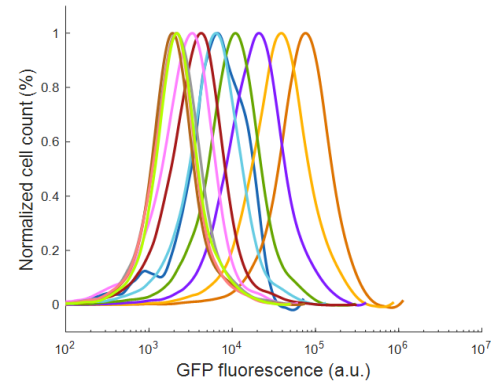


Fig. S55. Flow cytometry data for GFP over bacterial cells population containing OL design of  $P_{katG}$ . (A)  $[AHL]=0.4115 \mu M$ , (B)  $[AHL]=0.1371 \mu M$ , (C)  $[AHL]=0.0457 \mu M$ , (D)  $[AHL]=0.0152 \mu M$ , (E)  $[AHL]=0.0051 \mu M$ , (F)  $[AHL]=0.0017 \mu M$ , (G)  $[AHL]=0.00056 \mu M$ , (H)  $[AHL]=0 \mu M$ . This experimental data was used for generating Fig.8A and Fig.S22B.

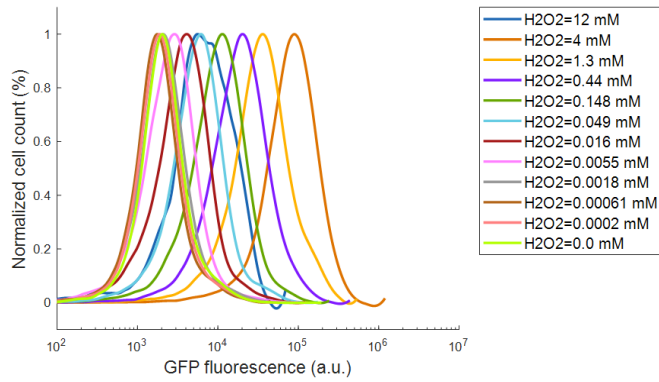
(A)



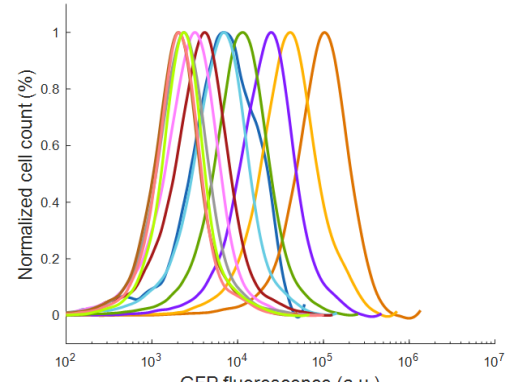
(B)



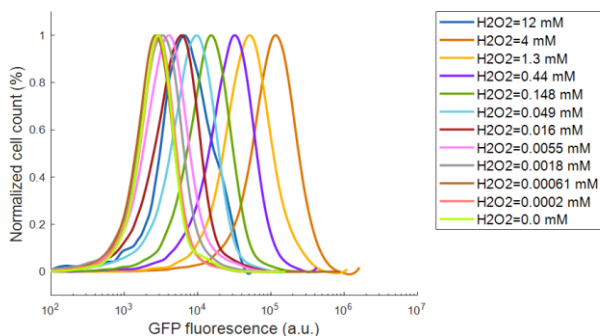
(C)



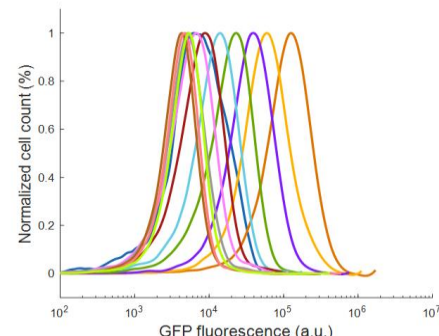
(D)



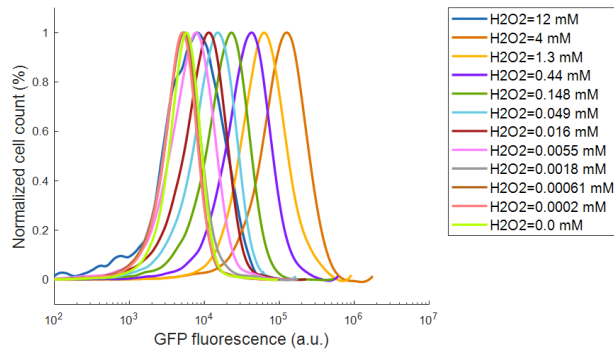
(E)



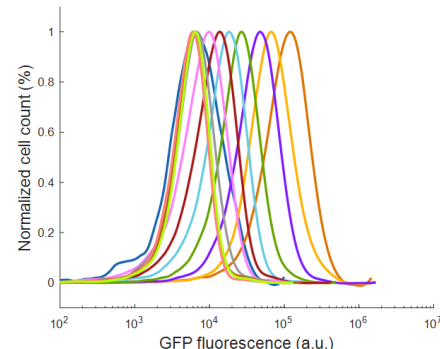
(F)



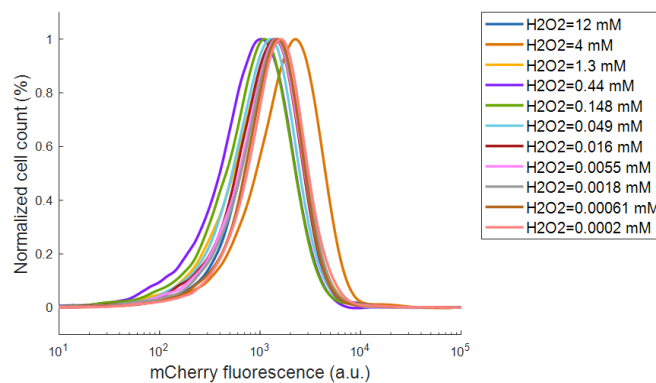
(G)



(H)



(I)



(J)

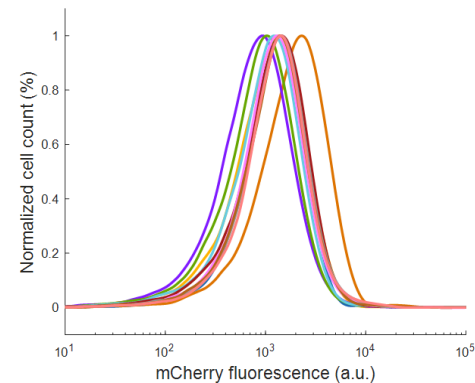
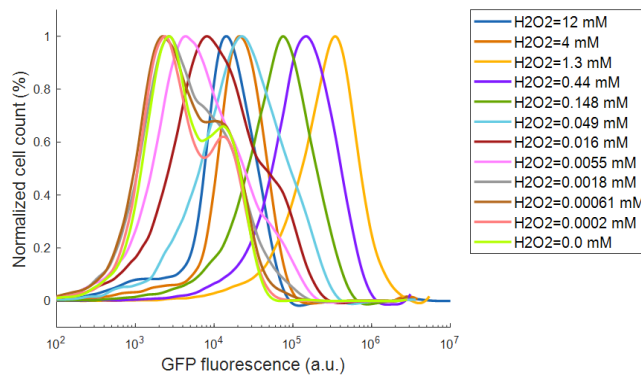
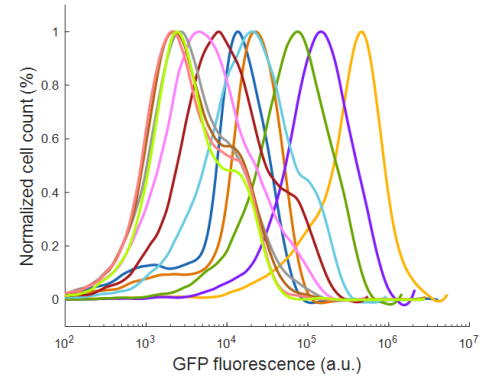


Fig. S56. Flow cytometry data for GFP over bacterial cells population containing ICF design of P<sub>katG</sub>. (A) [AHL]=0.4115 μM, (B) [AHL]=0.1371 μM, (C) [AHL]=0.0457 μM, (D) [AHL]=0.0152 μM, (E) [AHL]=0.0051 μM, (F) [AHL]=0.0017 μM, (G) [AHL]=0.00056 μM, (H) [AHL]=0 μM. (I-J) Flow cytometry data for mCherry over bacterial cells population containing ICF design. (I) [AHL]=0.0017 μM, (J) [AHL]=0.0 μM. This experimental data was used for generating Fif.8C and Fig.S22D.

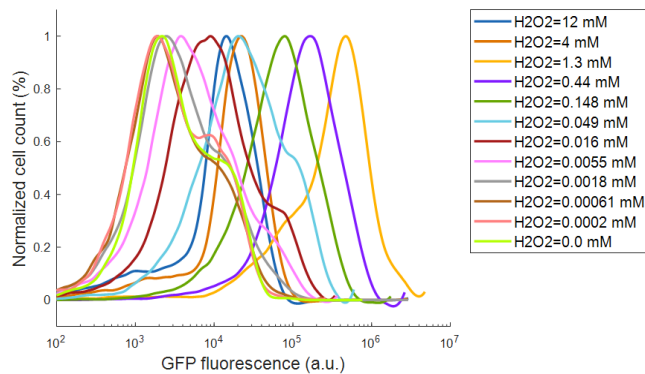
(A)



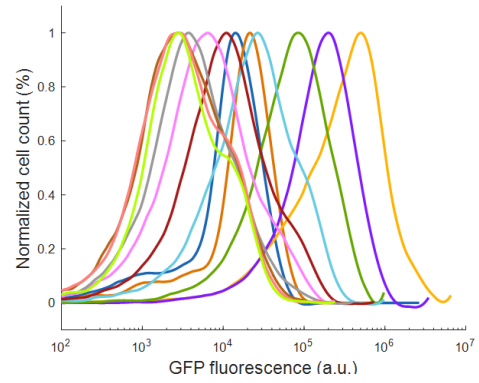
(B)



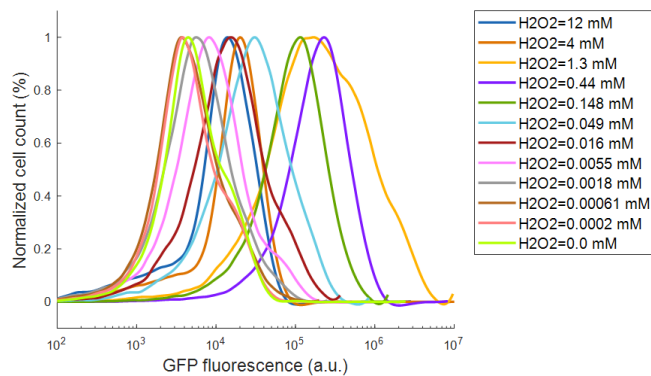
(C)



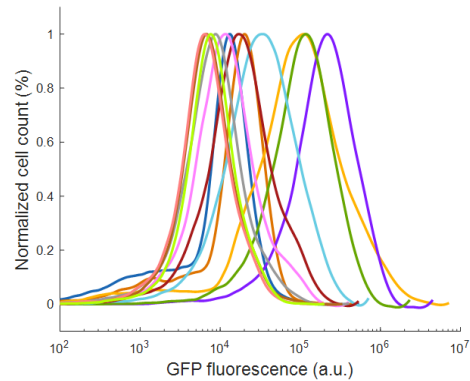
(D)



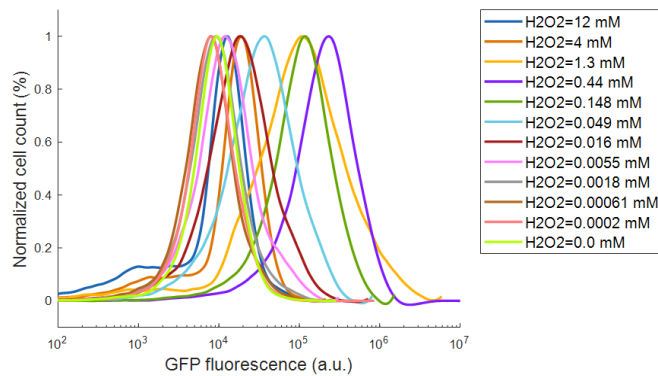
(E)



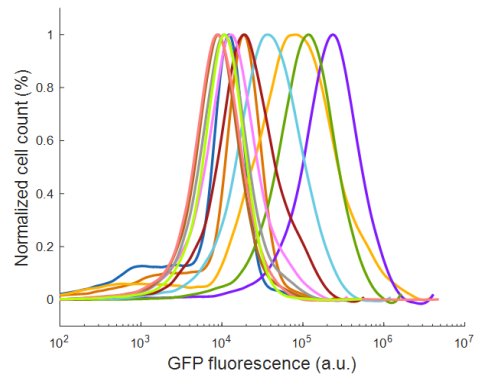
(F)



(G)



(H)



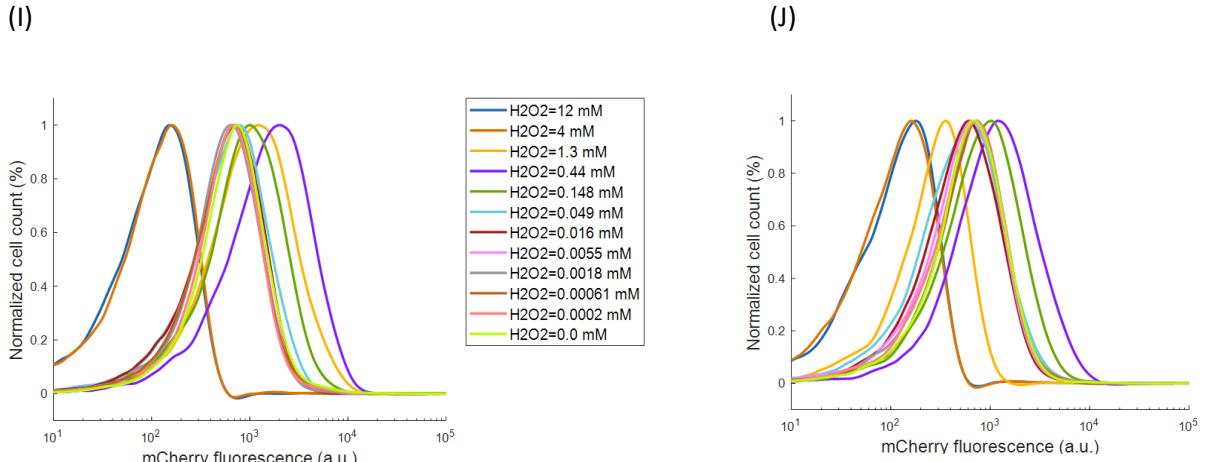


Fig. S57. Flow cytometry data for GFP over bacterial cells population containing DNF design of  $P_{katG}$ . (A)  $[AHL]=0.4115 \mu M$ , (B)  $[AHL]=0.1371 \mu M$ , (C)  $[AHL]=0.0457 \mu M$ , (D)  $[AHL]=0.0152 \mu M$ , (E)  $[AHL]=0.0051 \mu M$ , (F)  $[AHL]=0.0017 \mu M$ , (G)  $[AHL]=0.00056 \mu M$ , (H)  $[AHL]=0 \mu M$ . (I-J) Flow cytometry data for mCherry over bacterial cells population containing DNF design. (I)  $[AHL]=0.4115 \mu M$ , (J)  $[AHL]=0.0017 \mu M$ . This experimental data was used for generating Fig.S22E.

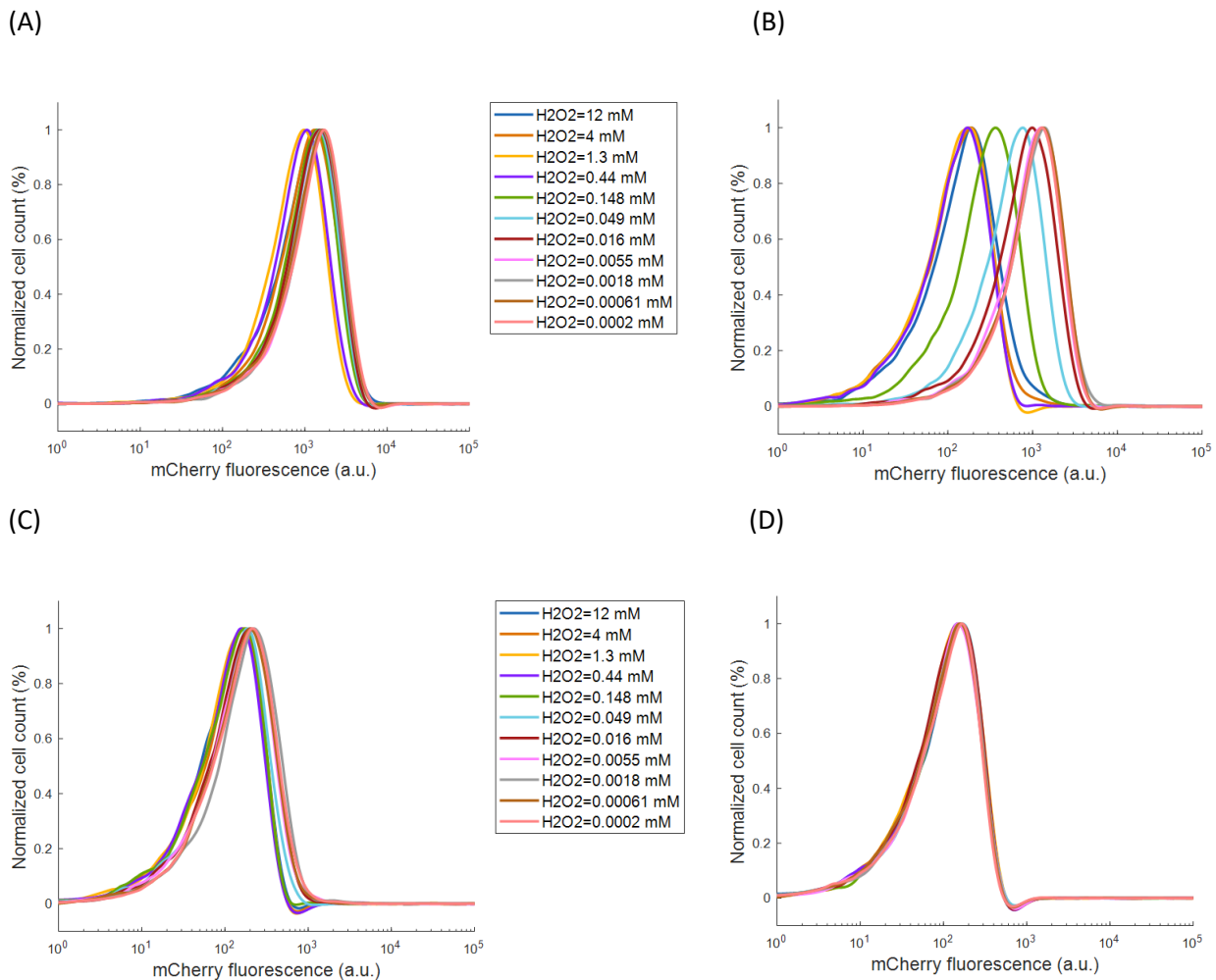


Fig. S58. Flow cytometry data for mCherry over bacterial cells population containing H<sub>2</sub>O<sub>2</sub>-aTc inverting switch design of P<sub>katG</sub>. (A) [aTc]=33.33ngr/ml, (B) [aTc]=11.11ngr/ml, (C) [aTc]=3.7ngr/ml, (D) [aTc]=1.23ngr/ml. This experimental data was used for generating Fig.8B and Fig.S22C.

#### 4.6 Experimental data for native stress promoter P<sub>recA</sub>

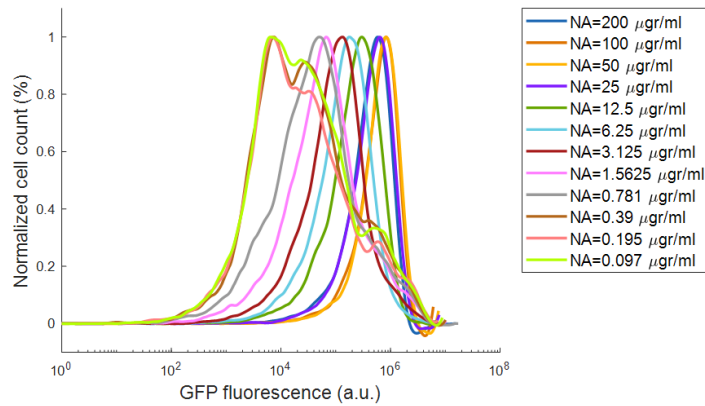
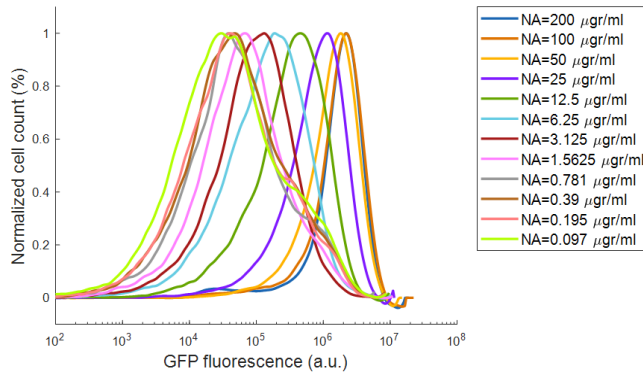
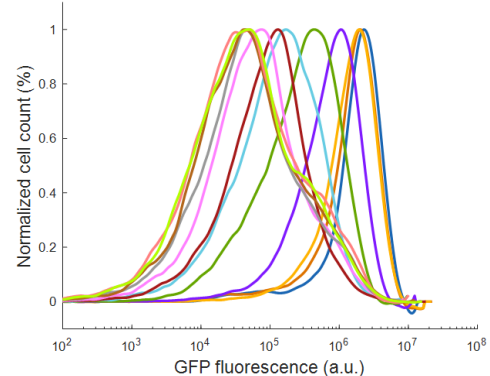


Fig. S59. Flow cytometry data for GFP over bacterial cells population containing P<sub>recA</sub> wild-type design. This experimental data was used for generating Fig.S23A.

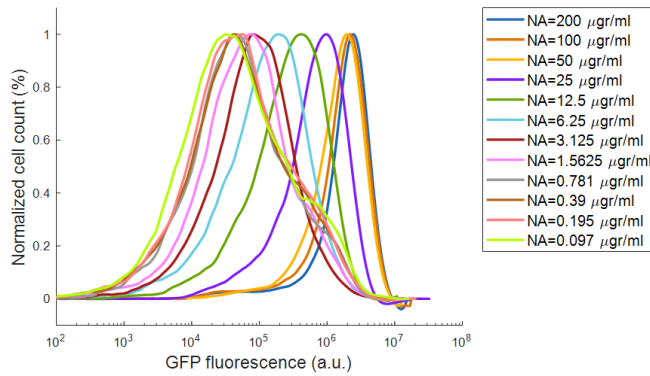
(A)



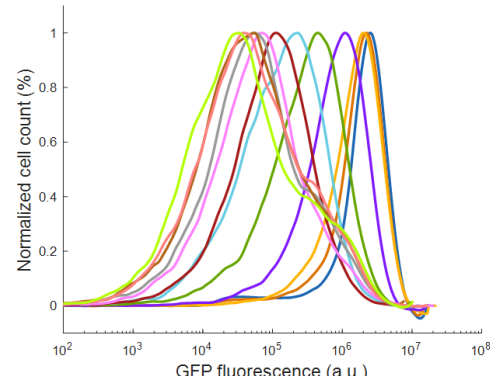
(B)



(C)



(D)



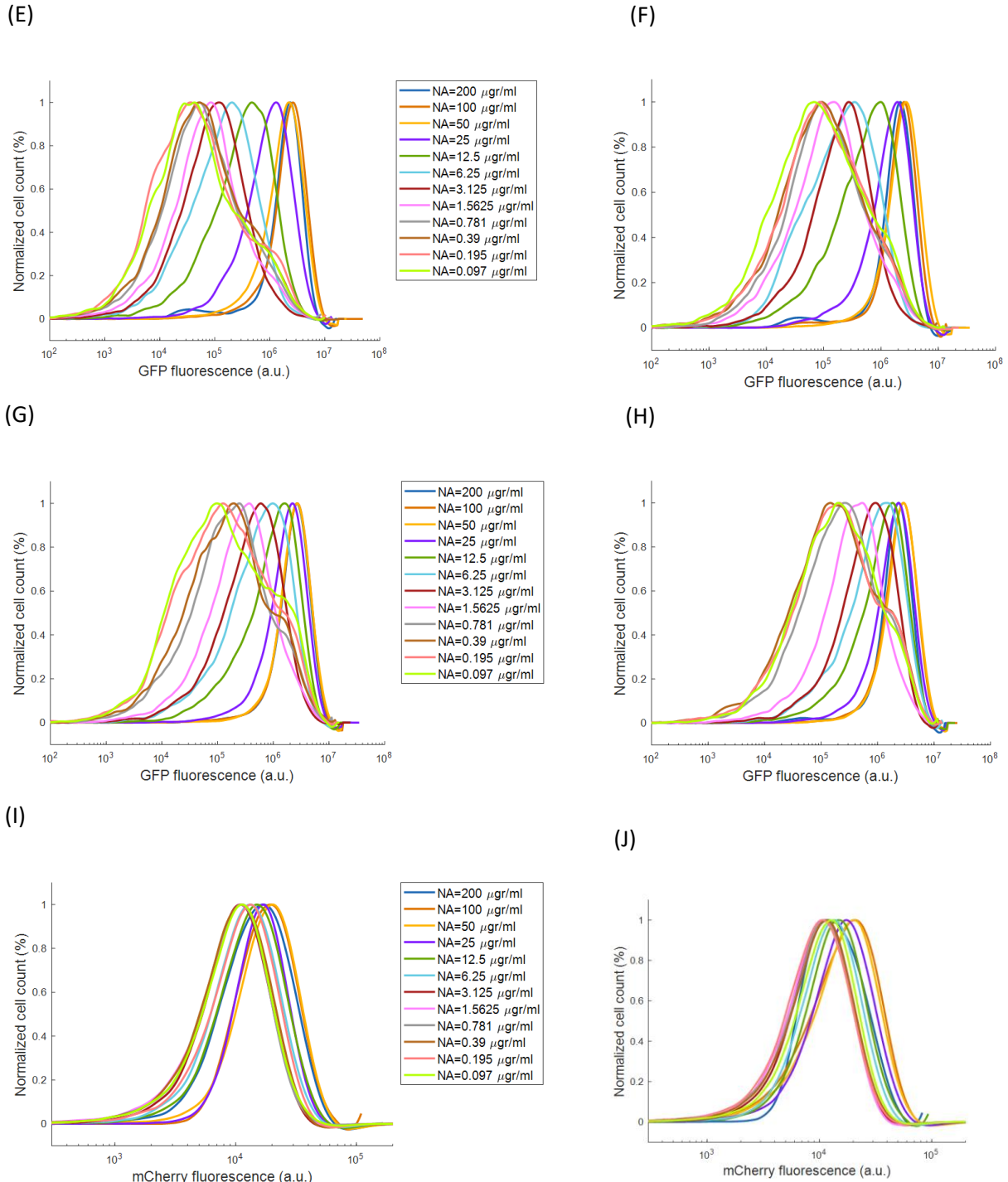
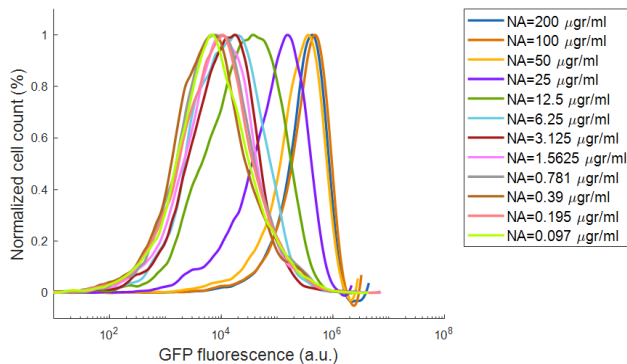
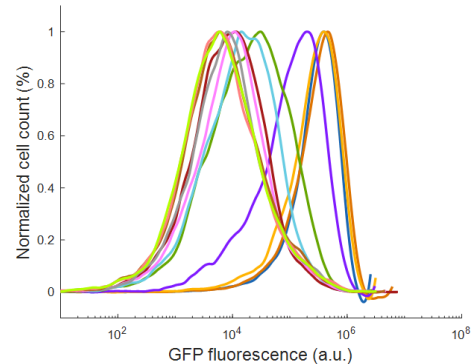


Fig. S60. Flow cytometry data for GFP over bacterial cells population containing AT-OL design of Preca. (A)  $[AHL]=0.1371 \mu\text{M}$ , (B)  $[AHL]=0.0457 \mu\text{M}$ , (C)  $[AHL]=0.0152 \mu\text{M}$ , (D)  $[AHL]=0.0051 \mu\text{M}$ , (E)  $[AHL]=0.0017 \mu\text{M}$ , (F)  $[AHL]=0.00056 \mu\text{M}$ , (G)  $[AHL]=0.0002 \mu\text{M}$ , (H)  $[AHL]=0 \mu\text{M}$ . (I-J) Flow cytometry data for mCherry over bacterial cells population containing AT-OL design. (I)  $[AHL]=0.0152 \mu\text{M}$ , (J)  $[AHL]=0.0017 \mu\text{M}$ . This experimental data was used for generating Fig.S23B.

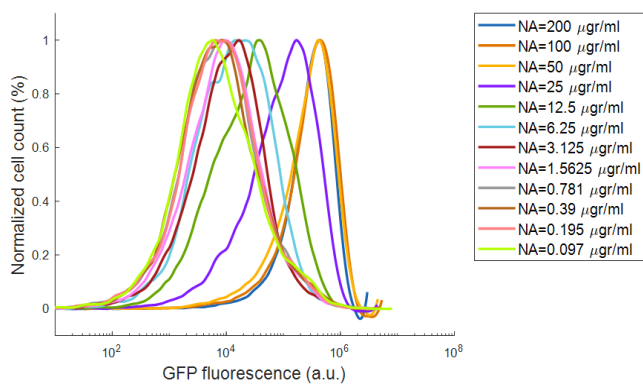
(A)



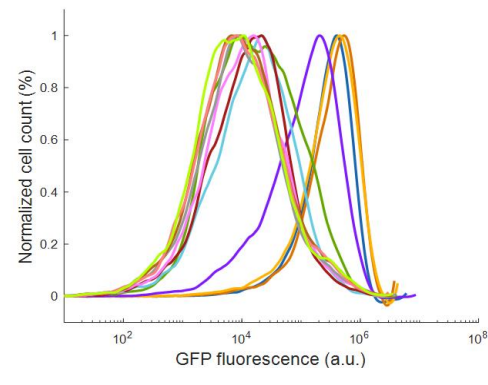
(B)



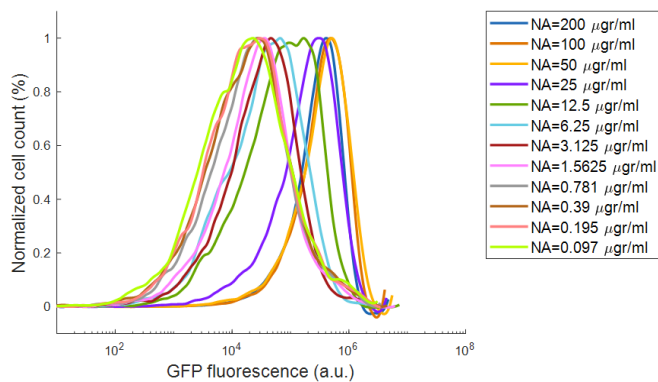
(C)



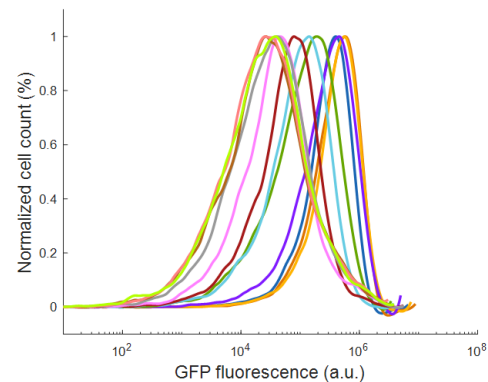
(D)



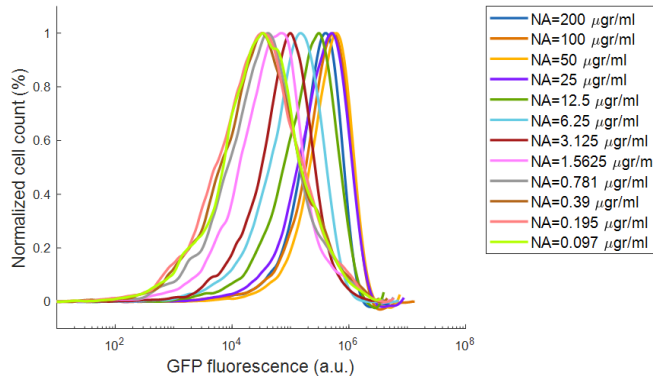
(E)



(F)



(G)



(H)

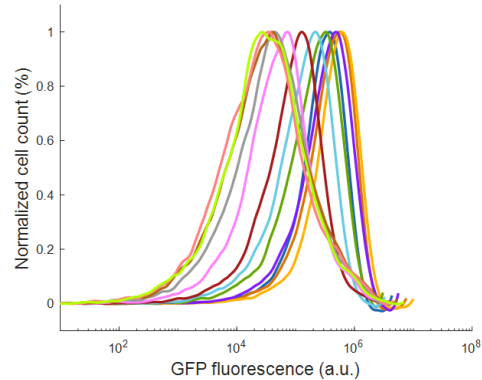
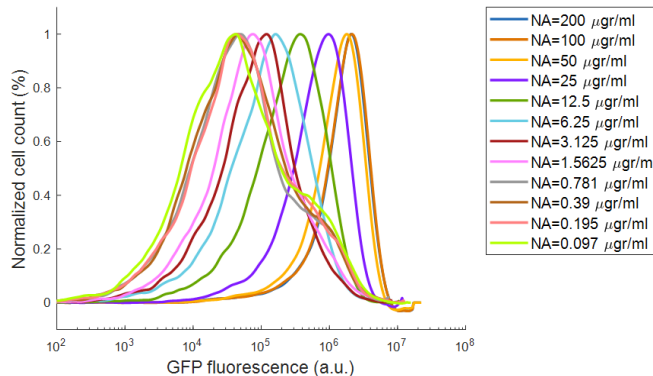
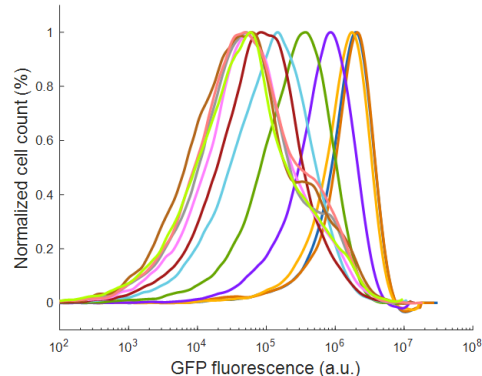


Fig. S61. Flow cytometry data for GFP over bacterial cells population containing TI-OL design of P<sub>recA</sub>. (A) [AHL]=0.1371  $\mu\text{M}$ , (B) [AHL]=0.0457  $\mu\text{M}$ , (C) [AHL]=0.0152  $\mu\text{M}$ , (D) [AHL]=0.0051  $\mu\text{M}$ , (E) [AHL]=0.0017  $\mu\text{M}$ , (F) [AHL]=0.00056  $\mu\text{M}$ , (G) [AHL]=0.0002  $\mu\text{M}$ , (H) [AHL]=0.0  $\mu\text{M}$ . This experimental data was used for generating Fig.8E and Fig.S23C.

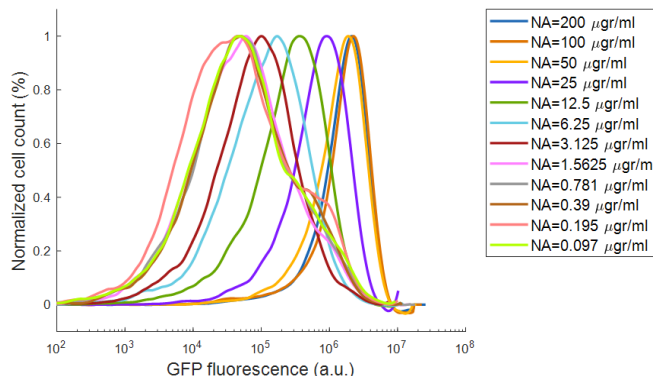
(A)



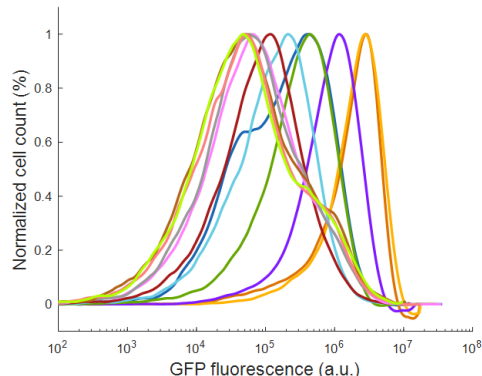
(B)



(C)



(D)



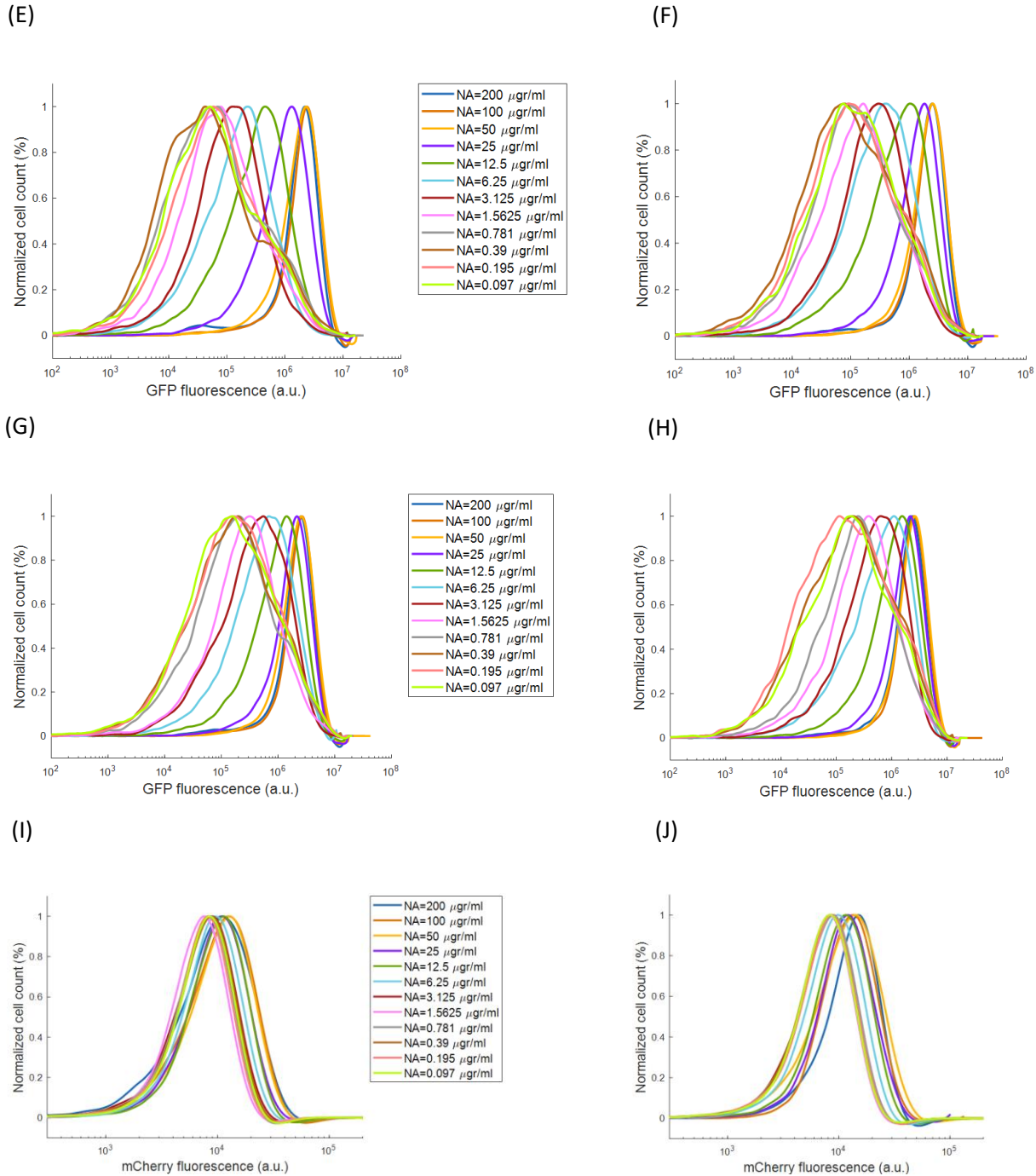


Fig. S62. Flow cytometry data for GFP over bacterial cells population containing ICF design of  $P_{recA}$ . (A)  $[AHL]=0.1371 \mu M$ , (B)  $[AHL]=0.0457 \mu M$ , (C)  $[AHL]=0.0152 \mu M$ , (D)  $[AHL]=0.0051 \mu M$ , (E)  $[AHL]=0.0017 \mu M$ , (F)  $[AHL]=0.00056 \mu M$ , (G)  $[AHL]=0.0002 \mu M$ , (H)  $[AHL]=0 \mu M$ . (I-J) Flow cytometry data for mCherry over bacterial cells population containing ICF design. (I)  $[AHL]=0.0152 \mu M$ , (J)  $[AHL]=0.0051 \mu M$ . This experimental data was used for generating Fig.8F and Fig.S23E.

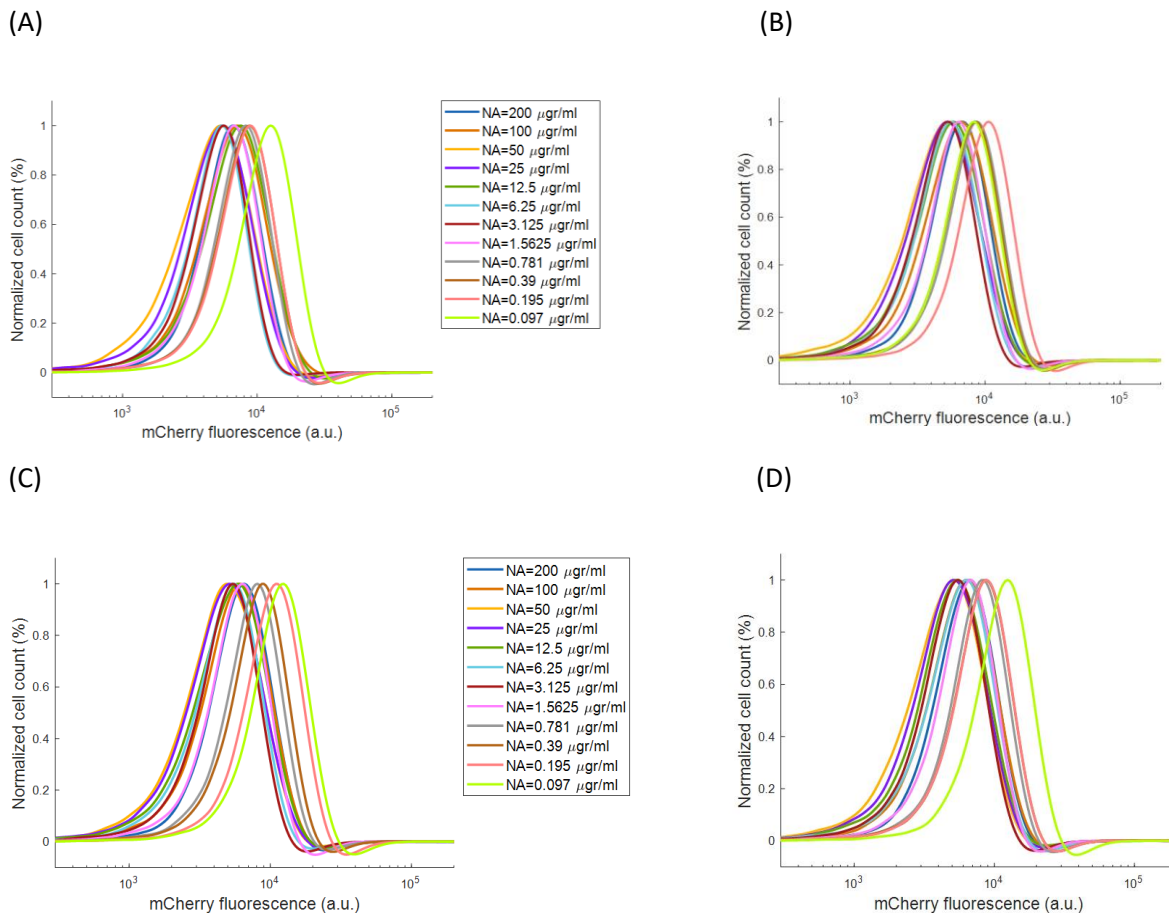
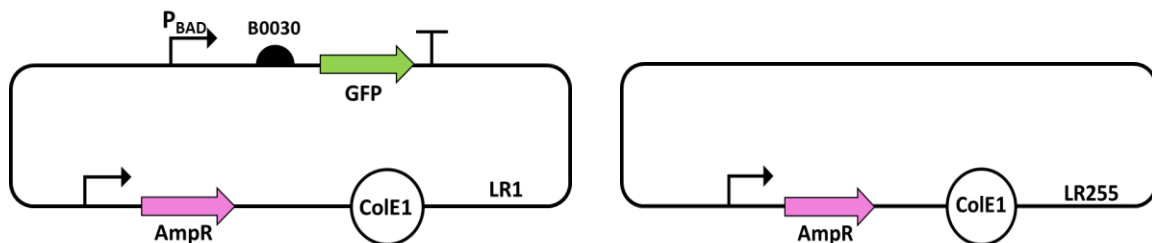
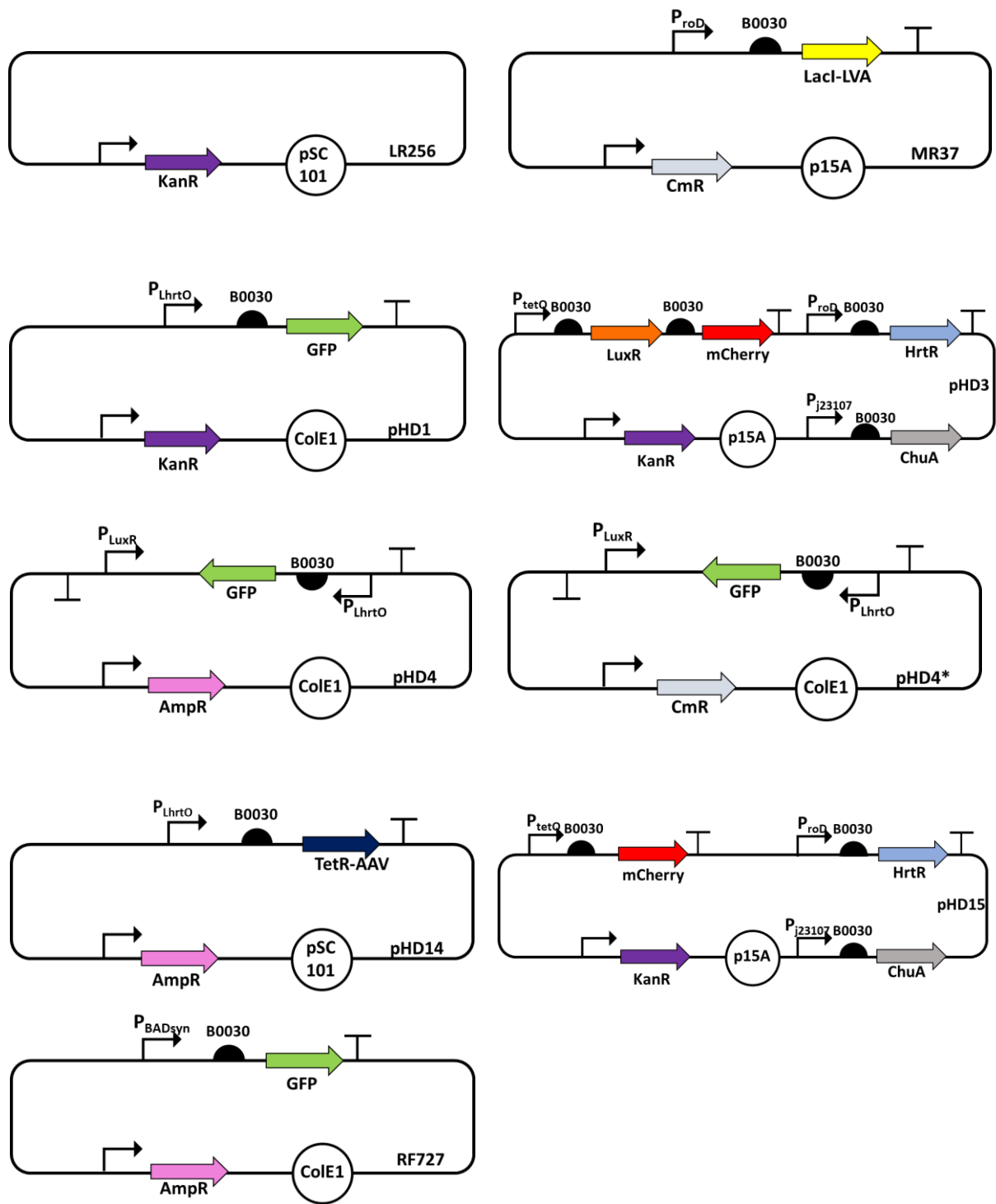
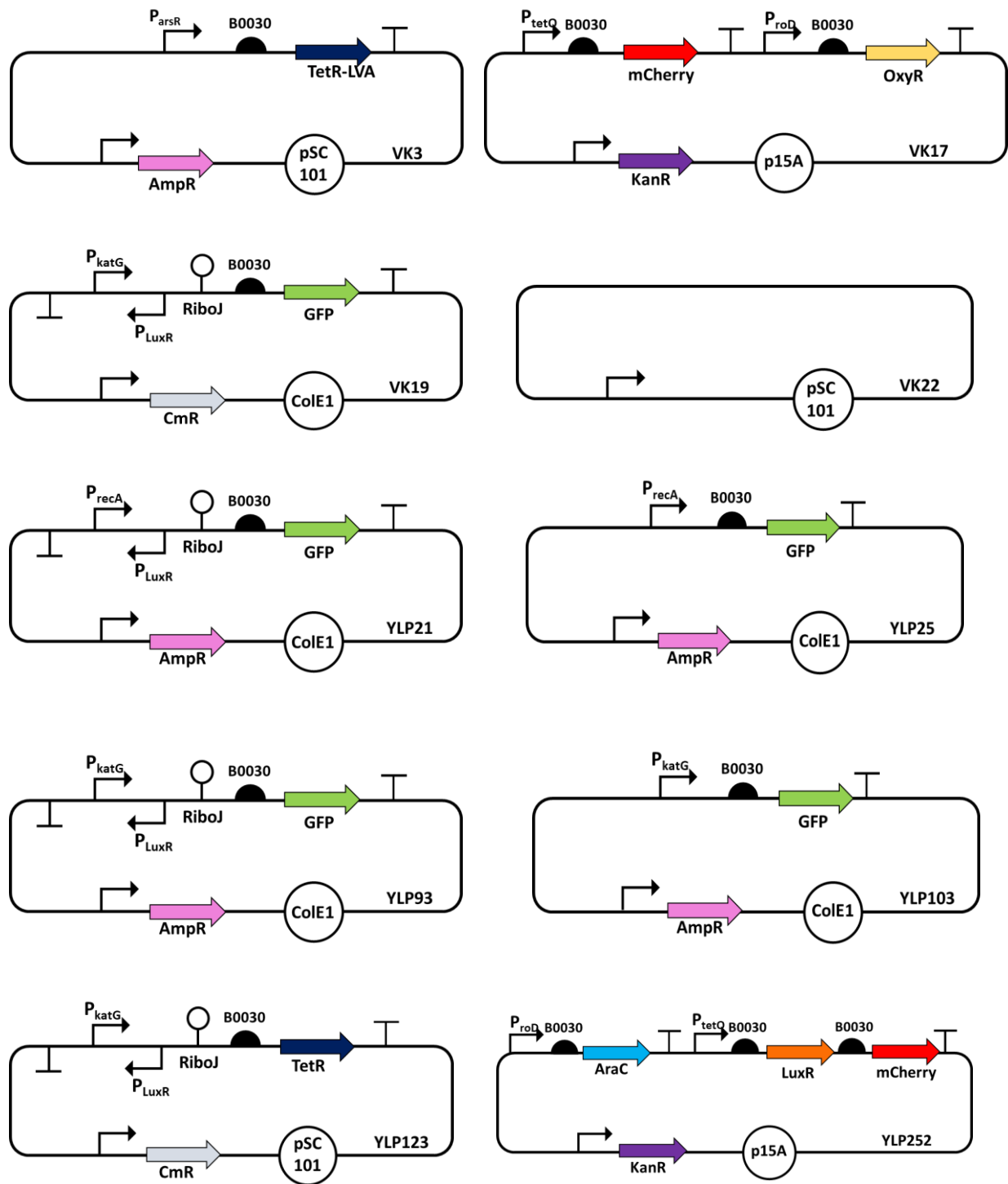


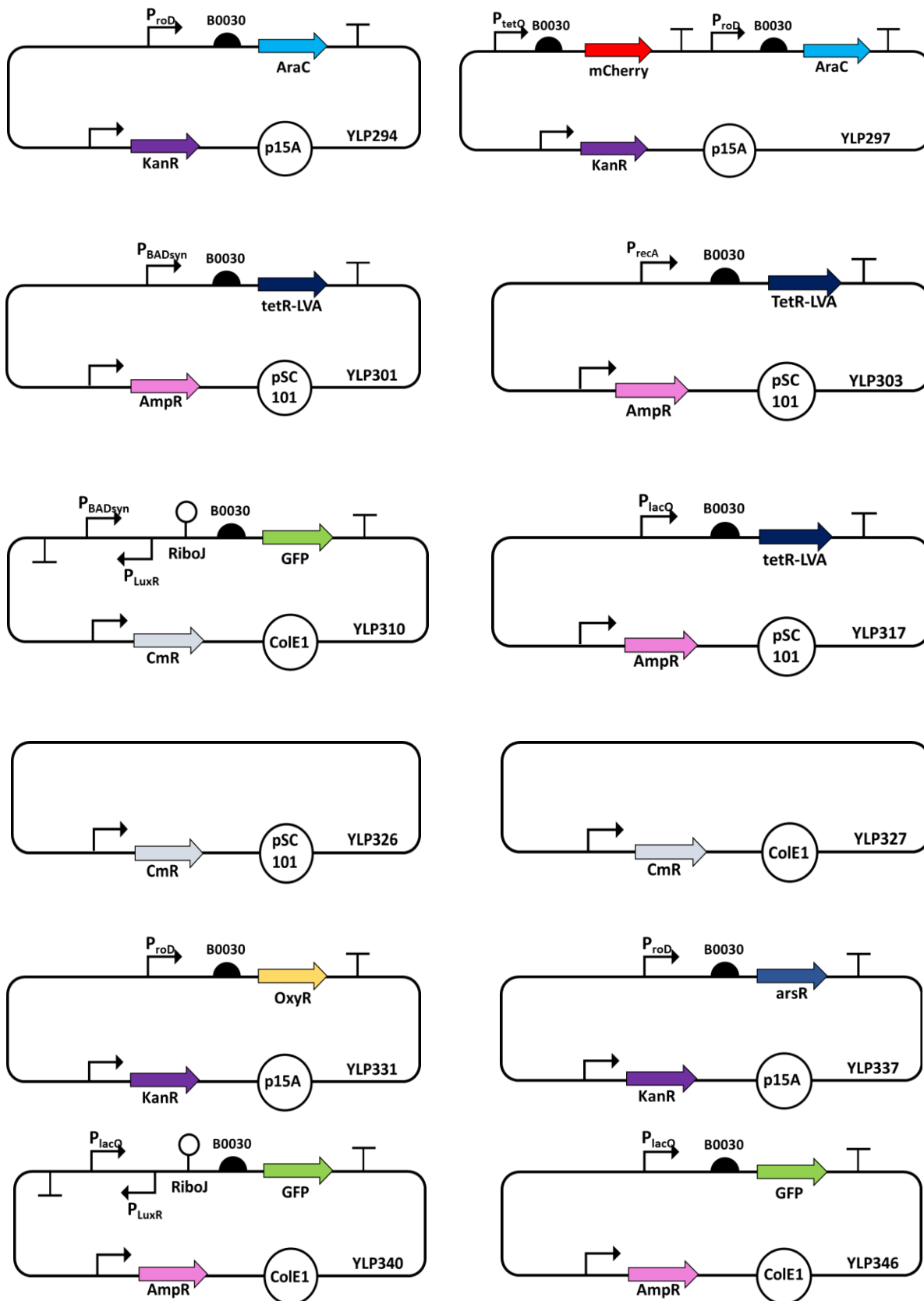
Fig. S63. Flow cytometry data for mCherry over bacterial cells population containing NA-aTc inverting switch design of  $P_{recA}$ . (A)[aTc]=33.33ngr/ml, (B)[aTc]=11.11ngr/ml, (C) [aTc]=1.23ngr/ml, (D) [aTc]=0.411ngr/ml. This experimental data was used for generating Fig.S23D.

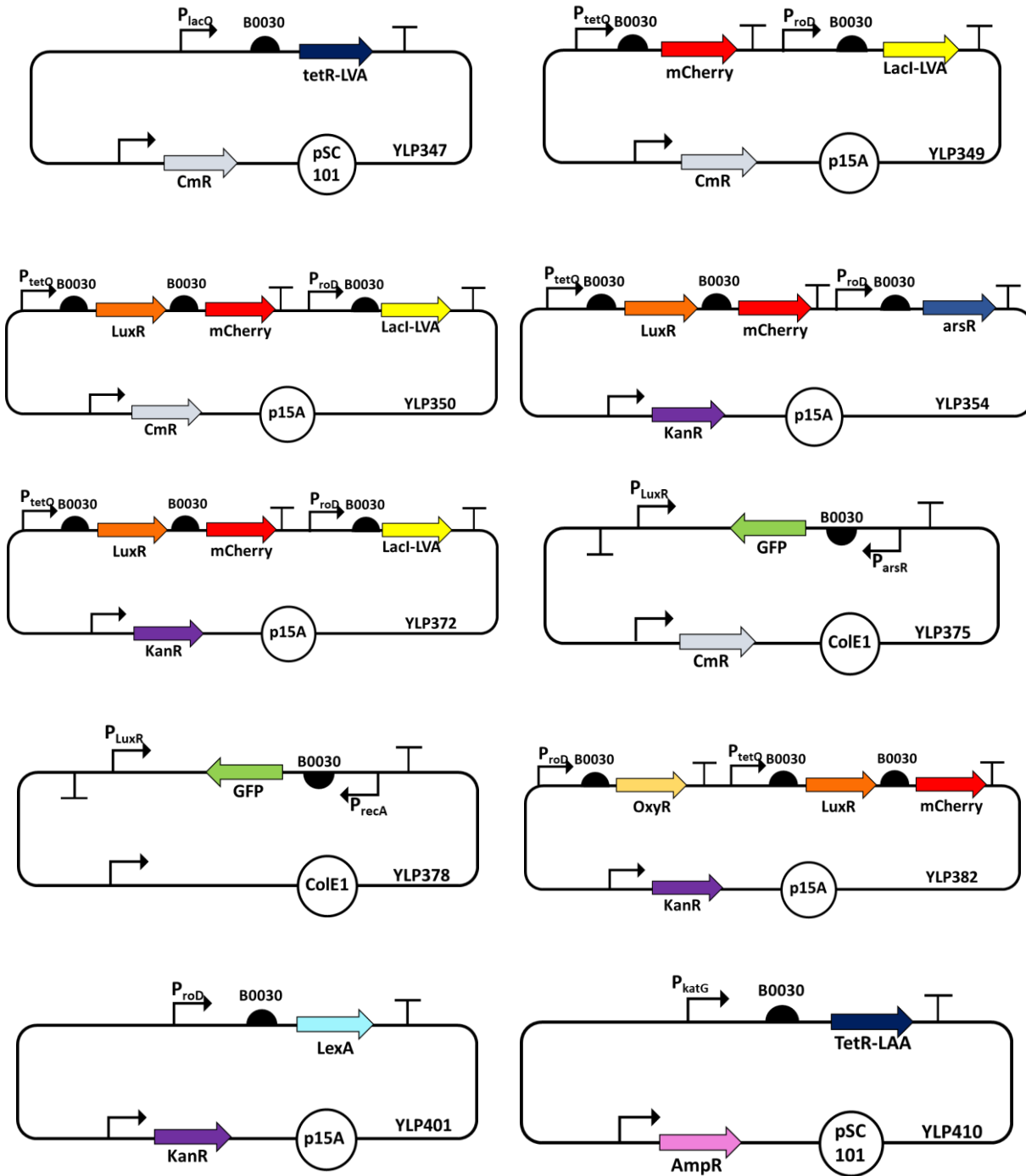
## 5. Plasmid maps used in this work.

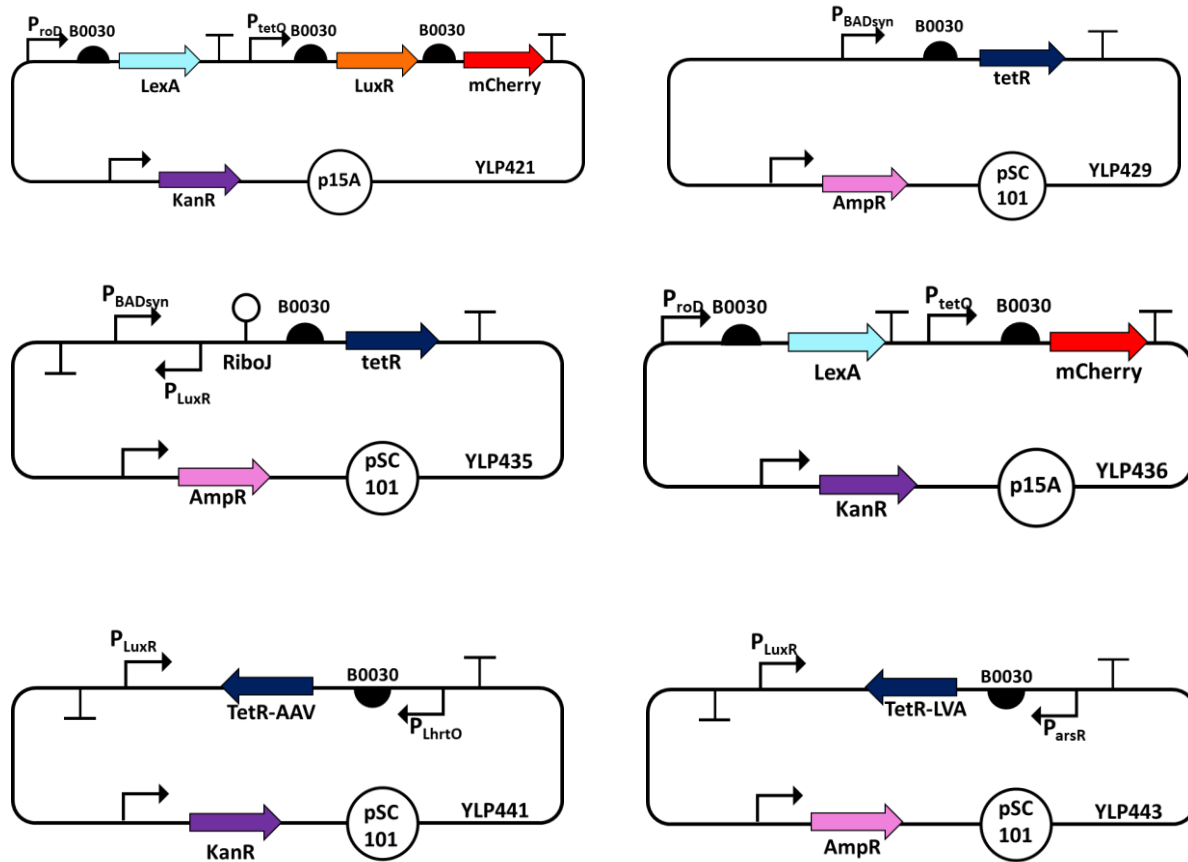












Promoter under test (PUT)	Circuit topology	Plasmids involved in circuit construction	Figures
P <sub>BAD</sub>	wt	LR1+YLP294	Fig.4C
P <sub>BADsyn</sub>	wt	RF727+YLP294	Fig.4C
	OL	YLP252+YLP310+VK22	Fig.6A, Fig.S17A
	ICF-TetR	YLP252+YLP310+YLP429	Fig.S17E
	ICF-TetR-LVA	YLP252+YLP310+YLP301	Fig.6B, Fig.S17D
	DNF-TetR	YLP252+YLP310+YLP435	Fig.S17F
	Arabinose-aTc inverting switch (TetR-LVA)	YLP297+YLP301	Fig.S17B
	Arabinose-aTc inverting switch (TetR)	YLP297+YLP429	Fig.S17C
P <sub>lacO</sub>	OL	YLP340+YLP350+LR256	Fig.S19A
	ICF-TetR-LVA	YLP340+YLP372+YLP347	Fig.S19C
	IPTG-aTc inverting switch	YLP317+YLP349	Fig.S19B

$P_{LhrtO}$	wt	pHD1+pMM549	Fig.7A, Fig.S20A
	OL	pHD3+pHD4	Fig.7B, Fig.S20B
	ICF-TetR-AAV	pHD3+pHD14+pHD4*	Fig.7C, Fig.S20D
	DNF-TetR-AAV	pHD3+YLP441+pHD4*	Fig.S20E
	Heme-aTc inverting switch for ICF	pHD15+pHD14	Fig.S20C
$P_{arsR}$	wt	YLP322+YLP337+YLP326	Fig.S21A
	OL	VK9+YLP354+YLP326	Fig.7E, Fig.S21B
	ICF-TetR-LVA	YLP375+YLP354+VK3	Fig.7F, Fig.S21D
	DNF-TetR-LVA	YLP375+YLP354+YLP443	Fig.S21E
	AsNaO <sub>2</sub> -aTc inverting switch for ICF	VK3+YLP354+YLP327	Fig.S21C
$P_{katG}$	wt	YLP103+YLP331+YLP326	Fig.S22A
	OL	YLP93+YLP382+YLP326	Fig.8A, Fig.S22B
	ICF	VK19+YLP382+YLP410	Fig.8C, Fig.S22D
	DNF	YLP93+YLP382+YLP123	Fig.S22E
	H <sub>2</sub> O <sub>2</sub> -aTc inverting switch for DNF	YLP123+VK17+LR255	Fig.8B, Fig.S22C
$P_{recA}$	wt	YLP25+YLP401+VK22	Fig.S23A
	AT-OL	YLP378+YLP421+VK22	Fig.S23B
	TI-OL	YLP21+YLP421+YLP326	Fig.8E, Fig.S23C
	ICF	YLP303+YLP421+YLP378	Fig.8F, Fig.S23E
	NA-aTc inverting switch	YLP303+YLP436	Fig.S23D

Table S1. List of plasmids used for synthetic genetic circuits in this work.

## 6. Synthetic parts used in this work

Part	Type	DNA sequence	Source
$P_{lacO}$	promoter	aattgtgagcgataacaattgacattgtgagcgataacaagatactgaggcacatcagcag gacgcactgacc	(Lutz & Bujard, 1997)
$P_{tetO}$	promoter	tccctatcagtgtatagagattgacatccctatcagtgtatagagatactgaggcacatcagcagg a cgcaactgacc	(Part: BBa_R004 0, 2013)
$P_{lux}$	promoter	acctgtaggatcgtagcgtaaggttacgcaagaaaatggtttatagtcgaataaa	(Part: BBa_R0062 - Parts.Igem.Org, 2013)
$P_{LhrtO}$	promoter	ataaatgacacagtgtcatggacaaaatgacacagtgtcatgatactgaggcaca	(Mimee et al., 2018)
$P_{roD}$	Constitutive promoter	cacagctaaccacaccgtcgccctatctgctgccctaggctatgagtggctgctggataacttt acgggcattgcataaggctcgataatatttcaggagaccacaacgggtccctctacaata attttgtttaacttt	(Davis et al., 2011)
$P_{j23107}$	Constitutive promoter	tttacggctagctcagccctaggattatgctagc	(Mimee et al., 2018)
$P_{BAD}$	Inducible promoter	aagaaaaccaattgtccatattgcatcagacattgccgtactgcgtctttactggcttctcgct aaccacccggtaaccccgcttattaaaaggcattctgtacaaaggcgggaccaaaggccatga caaaaacgcgtacaaaaggctataatcacggcagaaaaggccacattgatttgac gcgtcacacttgctatgccatgcattttatccataagattagcggatcctacctgacgc atcgcaactctctactgtttccat	(Lee et al., 1981)







		cggtgaagaacatctgaaggcgctggcacgcaaaggcgatttgcggcgttgcggcat cagcgccggattcgctgtgcaggaagagaagggtgcgcgtggtaggtcgatggct ggcggtgaaccacttgcgcacagcatattgaaggtcatttcgcgttgcattt caagccgaatgtgtttgcgcgtgcagggatgcgtgaaagatgcggcattt ggatggacttgctggcagtgcataaaactcaggatgtacgtacggcgttgc acgtattgtacgacaaggtaaccatgtgcgttgcgtcagcagagcttcaccattgaa gccagaaaatagcgagttaaaccatgtgcgttgcgtcagcagagcttcaccattgaa ggctggcggttgggttattcgcacaggcactggctgtaa	
TetR	CDS	atgtccagattagataaaagtaaagtgttacagcgccattagagctgttgcggaa tcgaagggttaacaacccgtaaactcgccagaagctggtaggttaggcgcctacattgtatt ggcatgtaaaaataagcgccgttgcgcacgccttaggcatttagataggcacc ataactcactttgcctttagaagggaaagctggcaagatttttacgtataaaagt ttagatgtgtttactaagtcatcgcatggggcaaaagttacatttaggtacacggcctacaga aaaacagtatgaaactctcgaaaatcaattgcctttatgccaacaagggtttcactagagaa tgcatttatgcactcagcgctgtgggcatttacttttaggtgcgtatttgcgttgc atcaagtgcctaaagaagaaaggaaacacactactgtatgtatgcgcatttacgac aagctatcgaattttgtatcaccaccaagggtcagagccagccttattcgccttgcattt tatgcggattagaaaaacaacttaatgtgaaagtgggtccaggcctgctgcaacacgacgaa aactacgctgcagcgtttaa	(Part: <i>BBA_C004</i> 0 <i>Parts.Igem.Org</i> , 2013)
TetR-AAV	CDS	atgtccagattagataaaagtaaagtgttacagcgccattagagctgttgcggaa tcgaagggttaacaacccgtaaactcgccagaagctggtaggttaggcgcctacattgtatt ggcatgtaaaaataagcgccgttgcgcacgccttaggcatttagataggcacc ataactcactttgcctttagaagggaaagctggcaagatttttacgtataaaagt ttagatgtgtttactaagtcatcgcatggggcaaaagttacatttaggtacacggcctacaga aaaacagtatgaaactctcgaaaatcaattgcctttatgccaacaagggtttcactagagaa tgcatttatgcactcagcgctgtgggcatttacttttaggtgcgtatttgcgttgc atcaagtgcctaaagaagaaaggaaacacactactgtatgtatgcgcatttacgac aagctatcgaattttgtatcaccaccaagggtcagagccagccttattcgccttgcattt tatgcggattagaaaaacaacttaatgtgaaagtgggtccaggcctgctgcaacacgacgaa aactacgctgcagcgtttaa	(Part: <i>BBA_C004</i> 0 <i>Parts.Igem.Org</i> , 2013)
TetR-LVA		atgtccagattagataaaagtaaagtgttacagcgccattagagctgttgcggaa tcgaagggttaacaacccgtaaactcgccagaagctggtaggttaggcgcctacattgtatt ggcatgtaaaaataagcgccgttgcgcacgccttaggcatttagataggcacc ataactcactttgcctttagaagggaaagctggcaagatttttacgtataaaagt ttagatgtgtttactaagtcatcgcatggggcaaaagttacatttaggtacacggcctacaga aaaacagtatgaaactctcgaaaatcaattgcctttatgccaacaagggtttcactagagaa tgcatttatgcactcagcgctgtgggcatttacttttaggtgcgtatttgcgttgc atcaagtgcctaaagaagaaaggaaacacactactgtatgtatgcgcatttacgac aagctatcgaattttgtatcaccaccaagggtcagagccagccttattcgccttgcattt tatgcggattagaaaaacaacttaatgtgaaagtgggtccaggcctgctgcaacacgacgaa aactacgcttttagtagcttaa	(Part: <i>BBA_C004</i> 0 <i>Parts.Igem.Org</i> , 2013)S20

Table S2. List of the synthetic parts, their types and sequences.

Primer	Description	Sequence
AatII-recA-f	P <sub>recA</sub> promoter, amplified from MG6515 genome	ttaa <ins>gacgtc</ins> agagaaggctgtcgac

EcoRI-recA-r	P <sub>recA</sub> promoter	tagtat <del>gaattc</del> gtcatgccggtaataccg
AatII-P <sub>katG</sub> -f	P <sub>katG</sub> promoter	tag <del>gacgtcc</del> gaaatgagggcgaaaa
KpnI-P <sub>katG</sub> -B0030-r	P <sub>katG</sub> promoter	taatat <del>ggtacc</del> tttctctttaatacagtgttaccgttacgatacac
Aat-P <sub>arsR</sub> -f	P <sub>arsR</sub> promoter	taacta <del>gacgtc</del> ccaactcaaattcacaccttattac
EcoRI-P <sub>arsR</sub> -r	P <sub>arsR</sub> promoter	taagg <del>tgaattc</del> ttgcaggtagtgtctcttcg
KpnI-LexA-f	LexA gene	tacaaatagtag <del>gttacc</del> atgaaagcgtaacggccaggc
BamHI-LexA-r	LexA gene	tacaat <del>ggatcc</del> taCAGCCAGTCGCCGTTGC
KpnI-arsR-f	arsR gene	taatc <del>aggtaacc</del> atgtcattctgttacccatccaatttg
BamHI-arsR-r	arsR gene	tactat <del>ggatcc</del> taactgcaaattttactgtccc
KpnI-OxyR-f	OxyR gene	atgc <del>ggtacc</del> atgaaatattcgtgatcttgatgtacc
BamHI-XmaI-OxyR-r	OxyR gene	gcat <del>ggatcc</del> cccggttaaacccgcctgtttaaaacttatac

Table S3. Primers used for part amplification in this work.

Symbol	Description
OL	Open loop
ICF	Indirect coherent feedforward
DNF	Double negative feedback
FCA	Fold change activation
PUT	Part under test
<i>In</i>	Inducer level
<i>Out</i>	Output level e.g., GFP, mCherry
$\beta$	Basal level of promoter
$S$	Sensitivity of part under test
$S_f$	Sensitivity of the function $f(In)$
$f(In)$	Non-linear monotonic function that describes the circuit behavior
$F_S$	Strength of the feedforward/feedback loops
$x$	Concentration of inducer
$x_0$	Initial concentration of inducer
MDL	Minimum detection level
$\theta$	Probability of binding of RNAPs to forward and reverse promoters simultaneously
$K_{df}$	Dissociation constant of transcription factors $X$ binding to forward promoter
$K_{dr}$	Dissociation constant of transcription factors $Y$ binding to reverse promoter
$K_{dz}$	Dissociation constant of transcription factors $Z$ binding to its promoter
$K_R$	Dissociation constant of repressor R binding to promoter P <sub>forw_R</sub>
$K_m$	Dissociation constant of the binding reaction between mRNA and antisense RNA
$X$	Concentration of transcription factors which bind to forward promoter
$Y$	Concentration of transcription factors which bind to reverse promoter
$Y_{max}$	Maximum concentration of transcription factors $Y$ which bind to reverse promoter P <sub>Rev</sub>
$Z$	Expression level of output
$Z_{max}$	Maximum protein level
$Z_{min}$	Minimum protein level
$n_f$	Hill-coefficient of transcription factors $X$ binding to forward promoter
$n_r$	Hill-coefficient of transcription factors $Y$ binding to reverse promoter
$n_z$	Hill-coefficient of transcription factors $Z$ binding to their promoter
$n_R$	Hill-coefficient of repressor R binding to promoter P <sub>forw_R</sub>
$P$	Probability that RNA polymerase is bound to the forward promoter at the equilibrium

$\rho_1$	Shift coefficient in switching threshold
$\rho_2$	Repression coefficient in the expression level
$\alpha$	Translation rate of Z through transcriptional interference
$\alpha_Z$	Translation rate of Z through antisense transcription
$mRNA$	Level of mRNA transcribed from forward promoter
$mRNA_T$	Total level of mRNA transcribed from forward promoter
$M_f$	Maximum mRNA level
$RNA_{Anti}$	Level of antisense RNA transcribed from reverse promoter located downstream to Z
$RNA_{Anti\_T}$	Total level of antisense RNA
$M_r$	Maximum $RNA_{Anti}$ level
$\tau_z$	Protein Z half-life
$\beta_f$	Basal level of forward promoter (w/o the reverse promoter)
$\beta_r$	Basal level of forward promoter (w/ the reverse promoter)
$R$	Concentration of repressor R which binds to promoter $P_{forw\_R}$
$R_{max}$	Maximum concentration of repressor R
$P_{forw\_R}$	Promoter that drives the expression of gene Y and is repressed by repressor R
$P_{forw}$	Forward promoter (sense) that drives the transcription of the out
$P_{Rev}$	Reverse promoter (antisense) that interferes with the transcription of the out
TF	Transcription factor
AHL	N-( $\beta$ -Ketocaproyl)-L-homoserine lactone 3OC6HSL
IPTG	Isopropyl- $\beta$ -D-1-thiogalactopyranoside
aTc	Anhydrotetracycline
$P_{lux}$	Promoter regulated by LuxR, sensitive for AHL
$P_{BAD}$	Promoter regulated by AraC and sensitive for arabinose
$P_{BADsyn}$	Synthetic AraC promoter, regulated by AraC and sensitive for arabinose
$P_{lacO}$	Promoter regulated by LacI and sensitive for IPTG
$P_{LhrtO}$	Promoter regulated by HrtR and sensitive for heme group
$P_{arsR}$	Promoter regulated by ArsR and sensitive for arsenic
$P_{katG}$	Promoter for a <i>katG</i> gene, regulated by OxyR and sensitive for $H_2O_2$
$P_{recA}$	Promoter for a <i>recA</i> gene, regulated by LexA and sensitive for Nalidixic acid (NA)

Table S4. List of parameters and abbreviations used in this work.

## References

- Ackers, G. K., Johnson, A. D., & Shea, M. A. (1982). Quantitative model for gene regulation by A phage repressor. *Proc. Natl Acad. Sci. USA*, 79, 1129–1133.
- Aslund, F., Zheng, M., Beckwith, J., & Storz, G. (2002). Regulation of the OxyR transcription factor by hydrogen peroxide and the cellular thiol-disulfide status. *Proceedings of the National Academy of Sciences*, 96(11), 6161–6165.
- Barger, N., Litovco, P., Li, X., Habib, M., & Daniel, R. (2019). Synthetic metabolic computation in a bioluminescence-sensing system. *Nucleic Acids Research*, 47(19), 10464–10474.
- Belkin, S., Smulski, D. R., Vollmer, A. C., Van Dyk, T. K., & Larossa, R. A. (1996). Oxidative stress

- detection with *Escherichia coli* harboring a katG'::lux fusion. *Applied and Environmental Microbiology*, 62(7), 2252–2256.
- Bintu, L., Buchler, N. E., Garcia, H. G., Gerland, U., Hwa, T., Kondev, J., & Phillips, R. (2005). Transcriptional regulation by the numbers: models. *Curr Opin Genet Dev*, 15(2), 116–124.
- Bongaerts, R. J. M., Hautefort, I., Sidebotham, J. M., & Hinton, J. C. D. (2002). Green fluorescent protein as a marker for conditional gene expression in bacterial cells. *Methods in Enzymology*, 358(February), 43–66.
- Brophy, J. A. N., & Voigt, C. A. (2016). Antisense transcription as a tool to tune gene expression. *Molecular Systems Biology*, 0–14.
- Davidov, Y., Rozen, R., Smulski, D. R., Van Dyk, T. K., Vollmer, A. C., Elsemore, D. A., LaRossa, R. A., & Belkin, S. (2000). Improved bacterial SOS promoter::lux fusions for genotoxicity detection. *Genetic Toxicology and Environmental Mutagenesis*, 466(Mutation Research), 97–107.
- Davis, J. H., Rubin, A. J., & Sauer, R. T. (2011). Design, construction and characterization of a set of insulated bacterial promoters. *Nucleic Acids Research*, 39(3), 1131–1141.
- Khvorova, A., Lescoute, A., Westhof, E., & Jayasena, S. D. (2003). Sequence elements outside the hammerhead ribozyme catalytic core enable intracellular activity. *Nature Structural Biology*, 10(9), 708–712.
- Lee, N. L., Gielow, W. O., & Wallace, R. G. (1981). Mechanism of araC autoregulation and the domains of two overlapping promoters, P(c) and P(bad), in the l-arabinose regulatory region of *Escherichia coli*. *Proceedings of the National Academy of Sciences of the United States of America*, 78(2 II), 752–756.
- Little, J. W., Mount, D. W., & Yanisch-Perron, C. R. (1981). Purified lexA protein is a repressor of the recA and lexA genes. *Proceedings of the National Academy of Sciences of the United States of America*, 78(7), 4199–4203.
- Lutz, R., & Bujard, H. (1997). Independent and tight regulation of transcriptional units in *Escherichia coli* via the LacR/O, the TetR/O and AraC/I 1-I 2 regulatory elements. *Nucl*, 25:6, 1203–1210.
- Mangan, S., & Alon, U. (2003). Structure and function of the feed-forward loop network motif. *Proceedings of the National Academy of Sciences of the United States of America*, 100(21), 11980–11985.
- Mimee, M., Nadeau, P., Hayward, A., Carim, S., Flanagan, S., Jerger, L., Collins, J., McDonnell, S., Swartwout, R., Citorik, R. J., Bulovi, V., Langer, R., Traverso, G., Chandrasekaran, A. P., & Lu, T. K. (2018). An ingestible bacterial-electronic system to monitor gastrointestinal health. *Science*, 918(May), 915–918.
- Panek, H. R., & Brian, M. R. O. (2004). *KatG Is the Primary Detoxifier of Hydrogen Peroxide Produced by Aerobic Metabolism in Bradyrhizobium japonicum*. 186(23), 7874–7880.
- Part: BBa\_C0040* parts.igem.org. (2013). [http://parts.igem.org/Part:BBa\\_C0040](http://parts.igem.org/Part:BBa_C0040)
- Part: BBa\_C0062* parts.igem.org/. (2013). [http://parts.igem.org/Part:BBa\\_C0062](http://parts.igem.org/Part:BBa_C0062)
- Part: BBa\_J33201* parts.igem.org. (2013). [http://parts.igem.org/Part:BBa\\_J33201](http://parts.igem.org/Part:BBa_J33201)
- Part: BBa\_R0040*. (2013). [http://parts.igem.org/Part:BBa\\_R0040](http://parts.igem.org/Part:BBa_R0040)
- Part: BBa\_R0062 - parts.igem.org*. (2013). [http://parts.igem.org/Part:BBa\\_R0062](http://parts.igem.org/Part:BBa_R0062)

- Shaner, N. C., Campbell, R. E., Steinbach, P. A., Giepmans, B. N. G., Palmer, A. E., & Tsien, R. Y. (2004). Improved monomeric red, orange and yellow fluorescent proteins derived from Discosoma sp. red fluorescent protein. *Nature Biotechnology*, 22(12), 1567–1572.
- Surre, J., Saint-ruf, C., Collin, V., Orenga, S., Ramjeet, M., & Matic, I. (2018). *Strong increase in the autofluorescence of cells signals struggle for survival.* 1–14.
- Vollmer, A. C., Belkin, S., Smulski, D. R., Van Dyk, T. K., & Larossa, R. A. (1997). Detection of DNA damage by use of Escherichia coli carrying recA’::lux, uvrA’::lux, or alkA’::lux reporter plasmids. *Applied and Environmental Microbiology*, 63(7), 2566–2571.
- Wan, X., Volpetti, F., Petrova, E., French, C., Maerkli, S. J., & Wang, B. (2019). Cascaded amplifying circuits enable ultrasensitive cellular sensors for toxic metals. *Nature Chemical Biology*, 15(5), 540–548.